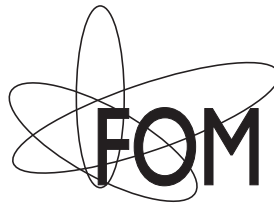


# Thermoelectric effects in magnetic nanostructures

Frank Bakker



University of Groningen  
**Zernike Institute  
for Advanced Materials**



Zernike Institute PhD thesis series 2012-21  
ISSN: 1570-1530  
ISBN: 978-90-367-5711-9  
ISBN: 978-90-367-5712-6 (electronic version)

The work described in this thesis was performed in the research group Physics of Nanodevices of the Zernike Institute for Advanced Materials at the University of Groningen, the Netherlands. This work is part of the research programme of the Foundation for Fundamental Research on Matter (FOM), which is part of the Netherlands Organisation for Scientific Research (NWO).

Cover design by: Floris Douma  
Printed by: Ipskamp Drukkers, Enschede

**RIJKSUNIVERSITEIT GRONINGEN**

**THERMOELECTRIC EFFECTS IN MAGNETIC  
NANOSTRUCTURES**

**Proefschrift**

ter verkrijging van het doctoraat in de  
Wiskunde en Natuurwetenschappen  
aan de Rijksuniversiteit Groningen  
op gezag van de  
Rector Magnificus, dr. E. Sterken,  
in het openbaar te verdedigen op  
vrijdag 5 oktober 2012  
om 14:30 uur

door

**Frank Lennart Bakker**

geboren op 3 maart 1984  
te Leeuwarden

Promotor: Prof.dr.ir. B.J. van Wees

Beoordelingscommissie: Prof.dr. C.H. Back  
Prof.dr. A. Brataas  
Prof.dr. T.T.M. Palstra

---

# Contents

<b>1</b>	<b>Introduction</b>	<b>1</b>
1.1	Electrons: charge, spin and heat . . . . .	1
1.2	Motivation . . . . .	2
1.3	Outline of this thesis . . . . .	6
	Bibliography . . . . .	8
<b>2</b>	<b>(Spin-) Caloritronics</b>	<b>11</b>
2.1	Thermal transport in metallic systems . . . . .	11
2.1.1	Seebeck and Peltier effects . . . . .	12
2.1.2	Phonon and magnon drag effects . . . . .	15
2.1.3	Nernst effects . . . . .	15
2.2	Spin transport in metallic systems . . . . .	16
2.2.1	Two-current model . . . . .	16
2.2.2	Non-local spin valve . . . . .	19
2.3	Spin-dependent thermoelectricity . . . . .	20
2.4	3-D Finite element modeling . . . . .	24
2.4.1	Dissipation due to spin relaxation . . . . .	25
2.5	Novel spin-caloritronic concepts . . . . .	26
2.5.1	Magnetically controllable heat currents . . . . .	27
2.5.2	Spin-dependent Thomson effect . . . . .	27
2.6	Summary . . . . .	28
	Bibliography . . . . .	30
<b>3</b>	<b>Interplay of Peltier and Seebeck effects in nanoscale nonlocal spin valves</b>	<b>35</b>
3.1	Introduction . . . . .	35
3.2	Nonlocal voltage detection . . . . .	36

---

3.3	Peltier and Seebeck effects . . . . .	37
3.4	Experimental realization . . . . .	38
3.5	First, second and third harmonic response . . . . .	39
3.6	Conclusion . . . . .	43
	Bibliography . . . . .	44
<b>4</b>	<b>Direct observation of the spin-dependent Peltier effect</b>	<b>47</b>
4.1	Introduction . . . . .	47
4.2	Concept of the experiment . . . . .	49
4.3	Spin-dependent Peltier measurement . . . . .	50
4.4	Conclusion . . . . .	53
4.5	Supplementary Information . . . . .	53
4.5.1	Calculation of the temperature gradient . . . . .	53
4.5.2	Electrochemical potential profile extracted from the modeling	54
4.5.3	Second harmonic response (Joule heating) . . . . .	55
4.5.4	Results for two other samples . . . . .	56
4.5.5	Measurements at 77K . . . . .	57
4.5.6	Modeling parameters . . . . .	59
	Bibliography . . . . .	60
<b>5</b>	<b>Nanoscale temperature detection using the Seebeck effect</b>	<b>63</b>
5.1	Introduction . . . . .	63
5.2	Experimental Techniques . . . . .	65
5.3	Model . . . . .	65
5.4	Results and Discussion . . . . .	67
5.5	Conclusion . . . . .	70
	Bibliography . . . . .	71
<b>6</b>	<b>Magnetization dynamics</b>	<b>73</b>
6.1	Introduction . . . . .	73
6.2	Magnetic energy . . . . .	75
6.3	Anisotropic magnetoresistance . . . . .	77
6.4	Magnetization dynamics . . . . .	78
6.4.1	Theory of ferromagnetic resonance (FMR) . . . . .	80
6.4.2	Detection of ferromagnetic resonance . . . . .	82
6.5	OOMMF Simulations . . . . .	83
6.6	Conclusion and outlook . . . . .	84
	Bibliography . . . . .	86

<b>7 Thermoelectric detection of ferromagnetic resonance of a nanoscale ferromagnet</b>	<b>91</b>
7.1 Introduction . . . . .	91
7.2 Heat generation during ferromagnetic resonance . . . . .	92
7.3 Experimental realization . . . . .	94
7.4 Thermoelectric detection of FMR . . . . .	95
7.5 Conclusion . . . . .	99
Bibliography . . . . .	100
<b>A Fabrication &amp; measurement techniques</b>	<b>103</b>
A.1 Fabrication techniques . . . . .	103
A.1.1 Deep-UV Lithography . . . . .	103
A.1.2 Electron beam lithography (EBL) . . . . .	105
A.1.3 Sputtering of lithographically defined strips . . . . .	106
A.2 Measurement setup and techniques . . . . .	108
A.2.1 Harmonic response voltages . . . . .	108
A.2.2 High frequency measurements . . . . .	110
<b>Summary</b>	<b>112</b>
<b>Samenvatting</b>	<b>116</b>
<b>Acknowledgements</b>	<b>121</b>
<b>Publications</b>	<b>125</b>
<b>Curriculum Vitae</b>	<b>127</b>





### 1.1 Electrons: charge, spin and heat

Electron transport in condensed matter is one of the most important physical phenomena used in today's technology. All modern electrical equipment, ranging from vacuum cleaners till high-end microprocessors is essentially founded on this type of transport. However, in most cases the electron's full potential is not used. Although electrons have multiple distinctive properties, most applications only exploit the negative elementary charge that it possesses. Since the discovery of the Giant Magneto Resistance (GMR) effect in 1990 by Nobel prize winners Albert Fert and Peter Grünberg [1, 2], another property of the electron has found its way to industry, the electron spin. This quantum-mechanical property describes the intrinsic angular momentum that is associated with an electron which is, in classical terms, like a spinning sphere of charge. In spin-based electronics (abbreviated as spintronics) [3], one aims at developing new device functionality by employing the magnetic dipole moment that is generated by the electron spin. The GMR effect is one of the first spintronic discoveries that has led to practical devices and is now implemented in read-heads of modern day hard drives. More recently, it has been demonstrated that spin currents have the ability to influence the orientation of magnetic memory elements, the so-called spin-transfer torque (STT) effect [4, 5]. This effect enables the fabrication of non-volatile magnetic random access memory devices which are faster and more energy efficient than the devices used in today's computers. The same spin-transfer torque effect can be used to induce a resonance of the magnetization of a ferromagnet. This precessional motion of the magnetization with gigahertz frequencies may be applicable for nanoscale tunable microwave sources in the near future [6, 7, 8, 9].

Thermoelectricity describes the relation between charge currents and heat currents and is based on a third property of electrons, their energy [10]. In 1821, Thomas Johann Seebeck discovered that a circuit made of two different metals, creates a magnetic field when the two junctions are kept at different temperatures [11]. Later, it was found that this magnetic field was in fact generated by an electrical current

that is induced in the metal - a thermoelectric current. Alternatively, if an open circuit is concerned, a potential difference will appear that depends only on the temperature of the ends of the two metals and which is known as the Seebeck potential. Few years later, a French physicist Jean-Charles Peltier found a closely related phenomenon, the Peltier effect. While the Seebeck effect describes the conversion of a temperature difference into a voltage, the reciprocal Peltier effect refers to the heat current that is induced when a charge current flows through a material. Since these great discoveries, both effects have found their way to many applications as for example thermocouples for temperature sensing and solid state refrigerators.

The interplay between charge, spin and heat transport in solid-state devices is schematically presented in Fig. 1.1. As discussed above, the interaction between charge and spin transport is part of the field of spintronics, whereas the coupling between charge and heat transport is described by thermoelectricity. From Fig. 1.1, it is evident that a third relation, spin-caloritronics, connects heat transport to spin transport [12]. Spin-caloritronics offers control of heat and spin currents, without charge currents being involved. Examples of the new functionality that arises from this coupling are spin sources driven by temperature gradients [13, 14, 15, 16] and vice versa, heating or cooling using spin currents. These novel phenomena, which can be studied in spintronic devices, are the main focus of this thesis. Although the obtained results presented here will not be directly implemented in integrated circuits, these recent developments are very promising for next-generation nanoelectronic devices and might radically alter the way we store and process information in the future.

## 1.2 Motivation

The research presented in this thesis aims at obtaining a better fundamental understanding of electron transport in magnetic nanostructures. In metallic spintronics, the interaction between charge and spin transport forms the basic principle for the development of novel devices. Although often disregarded, heat transport can significantly alter the electrical behavior of nanoscale devices. By including thermoelectricity in the already established spintronics theory, various new possible applications that arise from this coupling are addressed.

The different forms of transport are studied in metallic nanodevices that were fabricated with state-of-the-art nanofabrication techniques. During the purely electrical measurements that we performed in our experiments, a better fundamental understanding of the underlying (thermal) mechanisms that occur in spintronic nanostructures has been obtained. Furthermore, new physical phenomena that arise

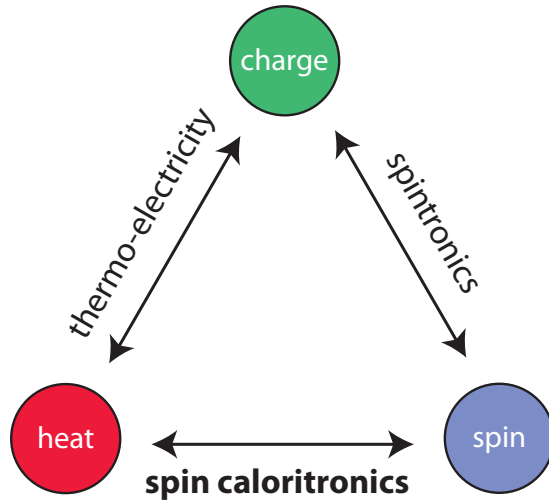


**Figure 1.1:** Interplay between the transport of spin, charge and heat in conductive media. The coupling between charge and spin transport forms the basis of modern spintronics and finds its applications in magnetic memory elements. Charge and heat transport are related to each other via thermoelectricity, used for heating/cooling elements or thermocouples. A relatively new aspect is the interplay between heat- and spin-transport, often referred to as spin-caloritronics. This new research field studies novel thermal phenomena that occur in magnetic structures.

from coupling between spin and heat transport have been revealed and demonstrated. In the remainder of this section, the main results which are presented in the Chapters 3, 4, 5 and 7 are introduced. In addition, the significance of this work for developing applicable spintronic devices is summarized for the different experiments that are performed.

### Interplay of Peltier and Seebeck effects in nonlocal spin valves

In Chapter 3, the conventional Peltier and Seebeck effects have been investigated in magnetic nanostructures. The magnetic devices that are used consist of two ferromagnetic strips connected by a nonmagnetic metal, thereby forming a so-called nonlocal spin valve. The nonlocal resistance depends on the orientation of the magnetization of both ferromagnets and the electrical current that is sent through. In the current literature that studies spin transport, the effect of Peltier and Seebeck effects and heat transport is usually disregarded. We have shown that a substantial part

of the observed signals has a thermoelectric origin. Peltier and Joule heating are distinguished by using a special measurement technique such that the magnitude of both contributions can be quantified.

The drive of the microelectronic industry towards smaller and smaller electronic components makes efficient heat management on the nanoscale essential. Especially in devices which contain multilayers of many different materials, the different Peltier and Seebeck coefficients lead to the generation of heat and voltages at the interfaces. Hence, a better mesoscopic understanding of thermoelectricity and Joule heating is of vital importance for the development of future nanoelectronic devices.

### **Direct observation of the spin-dependent Peltier effect**

Chapter 4 contains the first experimental demonstration of cooling and heating using a spin current - a current of angular momentum. This spin-dependent Peltier effect is similar to the conventional Peltier effect, but instead of a charge current, a spin current is required. The heating and cooling occurs in ferromagnetic materials, where the Peltier coefficient is different for electrons that are oriented parallel to the magnetization compared to electrons oriented anti-parallel to the magnetization. This property enables the switching between heating and cooling simply by the reversal of the magnetization. Hence, the effect becomes programmable.

The spin-dependent Peltier effect is investigated in a stacked spin-valve geometry, where the two ferromagnetic layers of permalloy are separated by a thin layer of copper. A thermocouple connected to the bottom of the pillar detects the cooling or heating induced by the spin currents. In addition, the effect of heating induced by the charge current and spin relaxation is studied.

In the research field of spintronics, the ultimate goal is to develop electronic circuits that function fully based on the spin of the electron, rather than its charge. Such an achievement could result in a perfect integration of information processing (currently based on the transport of electron charge) with information storage. Note that most of the hard drives fabricated nowadays exploit the electron spin for magnetic information storage. The spin-dependent Peltier effects allows for the control of temperature using pure spin currents. The earlier observed spin-dependent Seebeck effect [16] describes the inverse process, the generation of a spin current by a temperature gradient. This mechanism could prove very useful as a source of spin current or as a temperature sensor that generates a temperature dependent spin voltage. Both these spin-thermoelectric effects offer extra functionality that can be implemented in future spintronic devices.

### **Nanoscale temperature sensing using the Seebeck effect**

Accurate measurements of the electron temperature in metallic systems are demonstrated in Chapter 5. We study the effect of Joule and Peltier heating on the electron temperature by measuring the Seebeck effect in metallic nanoscale devices. For the study of especially spin-caloritronic effects, an accurate knowledge about thermal transport in nanoscale devices is essential.

Here we present an experimental study of the heat transfer in metallic nanostructures and compare it with 3D finite element modeling. The devices consist of an array of four interfaces between two different materials which can either be used for Seebeck measurements or Peltier heating/cooling. We achieved a good quantitative agreement between the experiments and the model, which confirms the validity of our transport model. The comparison of the experimental data with the model allowed for the experimental determination of the Seebeck coefficient for different materials. In addition, we observed a strong thickness dependence of the electrical conductivity, which is important for accurate modeling of Joule heating.

The obtained results are in good quantitative agreement with our model and hence, introducing spin-dependency of the model parameters help to conceive and develop novel spintronic devices. Furthermore, spin-dependent parameters can be extracted from the modeling provided that the heat transport is described accurately. Particularly, this has proven to be very useful in the analysis of the results of Chapter 4.

### **Thermoelectric detection of ferromagnetic resonance**

The interaction between spin dynamics and thermoelectricity is the subject of Chapter 6 and 7. Since the discovery of the spin-Seebeck effect, the coupling between magnetization dynamics and heat transport has attracted a lot of attention in the field of spintronics. Spin dynamics itself can be used as a microwave or spin source and has been investigated intensively, both theoretically and experimentally. However, experiments that study the relation between heat and magnetization dynamics are still scarce.

In Chapter 7, we present thermoelectric measurements of the heat dissipation during ferromagnetic resonance of a permalloy strip. We show for the first time an on-chip FMR detection technique based on the Seebeck effect. The device consists of a co-planar waveguide which is short-circuited at the end in order to generate a microwave field. The permalloy strip is located near the end of the waveguide and contacted by a thermocouple. This thermal technique is, unlike other methods, not restricted to electrically conductive media and is therefore also applicable to for instance ferromagnetic insulators. Furthermore, the dissipation during ferromag-

netic resonance is a phenomenon that is important for the analysis of dynamical spin-caloritronic experiments.

### 1.3 Outline of this thesis

The experimental and theoretical work presented in this thesis can be divided in two main parts. The first part, covered by Chapter 2, 3, 4 and 5, describes stationary spin-caloritronic features of spintronic devices. The second part, discussed in Chapter 6 and 7 focusses on the dynamical aspects of the magnetization motion combined with thermoelectricity. In the list below, a short overview for each chapter is given:

- *Chapter 2* introduces the general theory of heat, charge and spin transport and the relations between them. A diffusive two-channel transport model is derived which combines both spintronic and thermoelectric features. Many (spin-) caloritronic concepts such as the Seebeck and Peltier effect, Nernst and Thomson effects and their spin-dependent counterparts are covered. Additionally, the finite-element methods that are used to model the experimental devices are discussed.
- *Chapter 3* describes the thermoelectric origin of the baseline resistance that is observed in nonlocal spin valve measurements. Linear (Peltier and Seebeck effects), quadratic (Joule heating) and higher order effects are separated using lock-in measurements and the obtained data is compared with a finite element model.
- *Chapter 4* presents the direct observation of the spin-dependent Peltier effect in a spin valve device. Here, we experimentally demonstrate cooling/heating of a ferromagnetic metal induced by a spin current. The temperature difference between the parallel and anti-parallel configuration of the ferromagnets is monitored using a thermocouple. The spin-dependent Peltier coefficients are extracted by comparison of the data with a finite-element model.
- *Chapter 5* studies the effect of Joule heating on the electron temperature in metallic nanoscale devices. The results are compared to a diffusive 3D finite element model. In addition, Peltier heating and cooling is investigated and a technique to determine the Seebeck coefficient of a material is developed.
- *Chapter 6* covers the theory of magnetization dynamics which is necessary to describe the dissipation during ferromagnetic resonance. An introduction into

the relevant magnetic energies is given and the theory of ferromagnetic resonance is described. The dissipation during ferromagnetic resonance is calculated analytically and determined using numerical simulations in OOMMF.

- *Chapter 7* describes the Seebeck measurements of the heat dissipation during ferromagnetic resonance of a permalloy microstrip. We obtained resonance peaks for many different frequencies and extracted the phenomenological damping parameter. The experimental observations are compared with the theory using finite-element methods.

At the end of this thesis the details of the fabrication and measurement techniques are summarized in appendix A.

## Bibliography

- [1] M. Baibich, J. Broto, A. Fert, F. Van Dau, F. Petroff, P. Etienne, G. Creuzet, A. Friederich, and J. Chazelas, "Giant magnetoresistance of (001) Fe/(001) Cr magnetic superlattices," *Physical Review Letters* **61**(21), pp. 2472–2475, 1988.
- [2] G. Binasch, P. Grünberg, F. Saurenbach, and W. Zinn, "Enhanced magnetoresistance in layered magnetic structures with antiferromagnetic interlayer exchange," *Phys. Rev. B* **39**, pp. 4828–4830, Mar 1989.
- [3] I. Žutić, J. Fabian, and S. Das Sarma, "Spintronics: Fundamentals and applications," *Rev. Mod. Phys.* **76**, pp. 323–410, Apr 2004.
- [4] J. Slonczewski, "Current-driven excitation of magnetic multilayers," *Journal of Magnetism and Magnetic Materials* **159**, p. L1, June 1996.
- [5] L. Berger, "Emission of spin waves by a magnetic multilayer traversed by a current," *Physical Review B* **54**(13), p. 9353, 1996.
- [6] O. Boulle, V. Cros, J. Grollier, L. G. Pereira, C. Deranlot, F. Petroff, G. Faini, J. Barnas, and a. Fert, "Shaped angular dependence of the spin-transfer torque and microwave generation without magnetic field," *Nature Physics* **3**, pp. 492–497, May 2007.
- [7] D. Houssameddine, U. Ebels, B. Delaët, B. Rodmacq, I. Firastrau, F. Ponthenier, M. Brunet, C. Thirion, J.-P. Michel, L. Prejbeanu-Buda, M.-C. Cyrille, O. Redon, and B. Dieny, "Spin-torque oscillator using a perpendicular polarizer and a planar free layer," *Nature materials* **6**, p. 447, June 2007.
- [8] S. I. Kiselev, J. C. Sankey, I. N. Krivorotov, N. C. Emley, R. J. Schoelkopf, R. a. Buhrman, and D. C. Ralph, "Microwave oscillations of a nanomagnet driven by a spin-polarized current," *Nature* **425**, p. 380, Sept. 2003.
- [9] I. N. Krivorotov, N. C. Emley, J. C. Sankey, S. I. Kiselev, D. C. Ralph, and R. a. Buhrman, "Time-domain measurements of nanomagnet dynamics driven by spin-transfer torques," *Science (New York, N.Y.)* **307**, pp. 228–31, Jan. 2005.
- [10] D. K. C. MacDonald, *Thermoelectricity, An introduction to the Principles*, Dover Publications, Inc., Mineola, New York, 2006.
- [11] T. Seebeck, "Über die magnetische Polarisation der Metalle und Erze durch Temperatur-Differenz," *Ann. Phys.* **2**(September), pp. 287–292, 1826.
- [12] G. E. W. Bauer, A. H. MacDonald, and S. Maekawa, "Spin caloritronics," *Solid State Communications* **150**(11-12), pp. 459 – 460, 2010.
- [13] K. Uchida, S. Takahashi, K. Harii, J. Ieda, W. Koshibae, K. Ando, S. Maekawa, and E. Saitoh, "Observation of the spin Seebeck effect," *Nature* **455**, pp. 778–81, Oct. 2008.
- [14] C. M. Jaworski, J. Yang, S. Mack, D. D. Awschalom, J. P. Heremans, and R. C. Myers, "Observation of the spin-Seebeck effect in a ferromagnetic semiconductor," *Nature Materials* **9**, pp. 1–6, Sept. 2010.



- 
- [15] K. Uchida, J. Xiao, H. Adachi, J. Ohe, S. Takahashi, J. Ieda, T. Ota, Y. Kajiwara, H. Umezawa, H. Kawai, G. E. W. Bauer, S. Maekawa, and E. Saitoh, "Spin Seebeck insulator," *Nature Materials* **9**, pp. 1–4, Sept. 2010.
- [16] A. Slachter, F. L. Bakker, J.-P. Adam, and B. J. van Wees, "Thermally driven spin injection from a ferromagnet into a non-magnetic metal," *Nat Phys* **6**, pp. 879–882, 2010.



## Chapter 2

---

# (Spin-) Caloritronics

### Abstract

*In this chapter, the basic theory that covers the field of spin-caloritronics is discussed. The fundamental phenomena of heat transport and thermo electricity are reviewed before the two current model that describes spin transport is extended with spin-dependent Seebeck and Peltier effects. A finite element method is introduced that was used to model the 3D geometries of our devices. The chapter concludes with an overview of novel spin-caloritronic concepts that have not been demonstrated experimentally yet.*

## 2.1 Thermal transport in metallic systems

The electrical conductivity  $\sigma$  relates the flow of charge to the applied voltage gradient when no temperature gradient is applied. The thermal conductivity  $\kappa$ , on the other hand, defines the amount of heat flow that is generated by a temperature gradient when no electrical current is allowed to flow. Depending on the dimensions of metallic structures that are studied experimentally, there exist different theories to describe the heat transport microscopically (e.g. diffusive or ballistic). Since the relevant dimensions of the devices discussed here are usually much larger than the electron (or phonon) mean free path length, a classical diffusive model will give an appropriate description of the system. Heat conduction can then be described by the diffusive or collisional energy transfer of (quasi-) particles in a system where a temperature difference is applied. Lattice vibrations, called phonons, are in many materials responsible for the transport of heat. For metallic systems, however, the transport of energy is dominated by the large number of free electrons that are available [1]. Hence, in metals a strong relation between the electrical conductivity  $\sigma$  and thermal conductivity  $\kappa$  is present. The Wiedemann-Franz law describes this connection and states that  $\kappa = \sigma LT$  with  $T$  the temperature and  $L$  the Lorentz number. Moreover, charge and heat currents can interact with each other and their connection is described by thermoelectricity. The two basic phenomena of thermoelectricity are the Seebeck and Peltier effect and will be described in the next section.

### 2.1.1 Seebeck and Peltier effects

The Seebeck effect, discovered in 1821 by Thomas Seebeck [2], is the conversion of a temperature gradient into an electrical voltage and can be utilized to create thermocouples for temperature measurements. The Seebeck effect originates from the fact that the conductivity for the electrons is energy dependent. For a three-dimensional free electron system, the density of states  $g(E)$  scales with  $\sqrt{E}$  and the electron distribution over the energy states is described by Fermi-Dirac statistics. In Fig. 2.1, the density of states is plotted as a function of energy and the electron distribution is shown for the hot and cold end of a metallic conductor. At the hot end, the electrons are spread out over more (and higher) energy states and consequently, the average energy per electron is larger than for electrons in the cold region. Electrons that diffuse from the hot to the cold end have therefore more energy than the electrons which diffuse in the opposite direction, leading to net flow of energy. This process describes essentially the thermal conductivity of electrons. When the electrical conductivity of the high and low energy electrons is equal, both charge currents cancel and there is no net charge transfer. However, when the electrons with higher energies experience a different conductivity than the electrons with a lower energy, a net diffusion of charge occurs. In equilibrium, this process is opposed by an electric field that builds up and prevents further diffusion. This electric field is known as the Seebeck effect.

The energy dependent conductivity can be calculated from the Einstein relation using the diffusion coefficient  $D(E)$  and the density of states  $g(E)$  as  $\sigma(E) = e^2 g(E) D(E)$ . The Seebeck effect is enhanced whenever the conductivity depends strongly on energy and hence, if  $\left(\frac{d\sigma(E)}{dE}\right)_{E=E_F}$  is large. Thus, a large energy dependent scattering ( $D(E)$ ) and/or strong band bending ( $g(E)$ ) at the Fermi energy gives rise to an enhanced Seebeck effect. For simple metals, the Seebeck effect is well described based on the Mott relation [3] via:

$$S = -\frac{\pi^2}{3} \left(\frac{k_B^2 T}{e}\right) \left(\frac{\partial \ln(\sigma(E))}{\partial E}\right)_{E=E_F} \quad (2.1)$$

with  $E$  the electron energy. The Seebeck coefficient is for metals typically small and in the order of a few  $\mu V$  per Kelvin.

The sign and magnitude of the induced electric field is represented by the Seebeck coefficient  $S$ . In this thesis, the general convention for the sign of the Seebeck coefficient is used, being  $\nabla V = -S\nabla T$ . According to this convention the Seebeck coefficient is negative if diffusion of electrons from the hot end towards the cold end result in a negatively charged cold end. It is clear that for a free electron system (when  $\sigma(E + dE) > \sigma(E)$ ), the Seebeck coefficient is always negative. However,

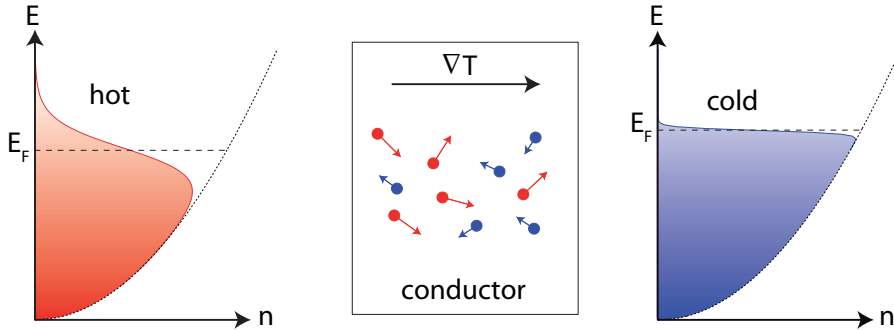


**Figure 2.1:** Illustration of the mechanism of the Seebeck effect when a temperature gradient is applied to a conductor. The density of states is plotted as a function of energy for the hot and cold end of a conductive medium. Because electrons obey Fermi-Dirac statistics, they are spread over a large number of energy states. At absolute zero temperature the distribution of occupied states drops abruptly to zero at the Fermi energy. However, at elevated temperatures, a fraction of the electrons can occupy states above the Fermi level. At the hot end, the average electron energy is larger than at the cold end. Hence, electrons which diffuse from the hot to the cold end transfer more energy than electrons that diffuse in opposite direction, resulting in a net transfer of energy while the net charge flow is zero. However, if the conductivity is larger for electrons with higher energies compared to lower energy electrons, the diffusion leads to a net flow of charge. This net diffusion of electrons from the hot to the cold end has to be compensated and consequently, an electric field or Seebeck voltage builds up.

in real metals the actual bending of the bands at the Fermi energy and the different scattering mechanisms have to be taken into account and the Seebeck coefficient can be positive.

Figure 2.2a shows a thermocouple which can be used to measure a temperature difference based on the Seebeck effect. Two wires of different materials are joined together at a temperature  $T_1$  and the other two ends are kept at a reference temperature  $T_0$ . The voltage that arises is now the difference between the two Seebeck voltages that develop in both materials and is given by  $V = (S_A - S_B)(T_1 - T_0)$ , where  $S_{A,B}$  are the material dependent Seebeck coefficients (sometimes also called thermopower).

The reciprocal Peltier effect describes the generation or absorbance of heat when an electrical current is sent through a junction of two different materials. This phenomena arises from the fact that there is always a heat current  $Q$  associated with a charge current  $I$  in a material (schematically depicted in Fig. 2.2b). For dissimilar materials, the associated heat currents are different ( $Q_A \neq Q_B$ ) and heat evolves

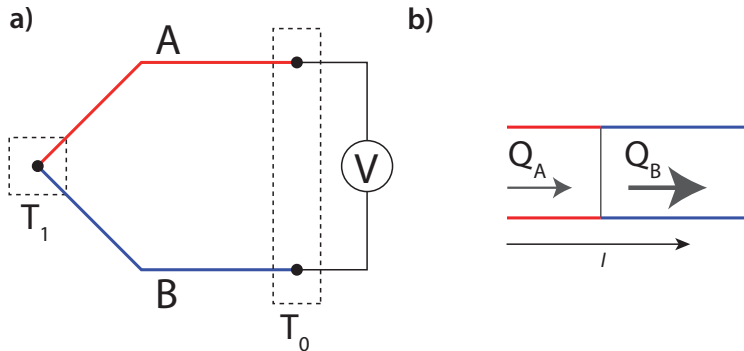


**Figure 2.2:** (a) Basic thermoelectric circuit for measuring the Seebeck effect. If A and B have different Seebeck coefficients, the thermoelectric potential generated across material A differs from that of material B and is proportional to  $\Delta T$ . (b) Schematic representation of the Peltier effect. An electrical current carries a certain amount of heat with it, described by the Peltier coefficient. If two materials with different Peltier coefficients are connected, the difference in heat current between both materials leads to cooling or heating at the interface, dependent on the current direction.

or vanishes at the interface depending on the charge current direction. Therefore, applications of the Peltier effect can be found in solid state cooling or heating elements. From Onsager's reciprocity [4, 5] it follows that the Seebeck coefficient  $S$  and the Peltier coefficient  $\Pi$  are connected via  $\Pi = ST$ , the Thomson-Onsager relation.

Thermal transport and thermoelectric effects in nanoscale devices differ from thermal transport in macroscopic systems in the sense that the role of interfaces and the surface become increasingly important [6]. In addition, when the size of the system approaches the mean free path lengths of phonons and electrons, the system can be locally out of equilibrium. Since the temperature is usually defined as the average energy of a system of particles in equilibrium, a temperature can, in that case, not be assigned [7]. Recently, the interest in thermoelectric properties of nanostructured and/or low-dimensional materials is increasing as they can offer much higher efficiency, thereby opening up new possibilities for efficient solid state cooling devices [8]. The performance of a thermoelectric material is often expressed by a figure of merit,  $ZT$ , where  $Z$  is a combination of thermal properties namely  $Z = \sigma S^2 / \kappa$  and  $T$  is the absolute temperature. A higher  $ZT$  value reflects a better thermodynamic efficiency and for thermoelectrics to compete with mechanical devices a value of 3 – 4 is needed. At this moment, the highest thermopowers have been reported in novel materials as superlattices of  $\text{Bi}_2\text{Te}_3/\text{Sb}_2\text{Te}_3$  [9] ( $ZT \approx 2.4$ ) and silicon nanowires [10] ( $ZT \approx 1.0$ ). On the other hand, it has been demonstrated

the Seebeck and Peltier coefficients for many metals can be significantly enhanced in thin films [11, 12, 13, 14].

### 2.1.2 Phonon and magnon drag effects

In the discussion of the Peltier and Seebeck effects, we have considered the free electrons in the metal as particles that do not interact with the ionic lattice. For weak interactions between the electrons and the lattice, the free electron model may indeed be sufficient, but in many cases these effects cannot be neglected. Suppose a temperature gradient is applied to a piece of metal. Now, heat flows through the lattice in the form of phonons (lattice waves), where energy is transported from the hotter to the colder end. In the absence of interactions between phonons and electrons, the phonon heat flow is irrelevant and the free electron model still holds for the description of thermoelectric effects. However, if the phonon energy current interacts significantly with the conduction electrons, collisions between electrons and phonons will cause the phonons to drag the electrons with them from the hotter to the colder end. This effect, known as 'phonon drag' has been predicted for the first time by L. Gurevich [15, 16] and leads to a modified total thermopower. The phonon drag effect can be comparable in magnitude to the free electron Seebeck effect and leads to a peak in the experimentally observed thermopower at lower temperatures. However, at room temperature the effect is negligible for typical metals [17].

Heat transport in ferromagnetic metals is governed by electrons, phonons and additionally, magnons. Magnons are spin-wave quanta that diffuse from the hotter region towards the colder region and may, similar to the phonon drag effect, add an extra contribution to the Seebeck coefficient. Recently, the first quantitative experimental observation of the magnon-drag effect in Permalloy has been reported by Costache *et al.* [18] and showed a magnon-drag contribution to the Seebeck coefficient of maximum 10% at room temperature.

### 2.1.3 Nernst effects

The Nernst effect describes the Hall voltage that arises when a temperature gradient and a perpendicular magnetic field are present in a conductive medium. Normal to the temperature gradient and magnetic field, an electrical field will then be induced [19]. Conversely, a heat current induced by an applied charge current (and a perpendicular magnetic field) is called the Ettinghausen effect. In ferromagnetic materials, similar as for the anomalous Hall effect [20], an anomalous Nernst effect is also present. Here the induced voltage depends on both the magnetization and a transverse heat gradient [21] and a magnetic field is not necessary. Experimentally,

the anomalous Nernst effect often obscures spin valve measurements as discussed by Slachter *et al.* [22] or spin Hall measurements as reported by Seki *et al.* [23].

The spin degree of freedom allows for the existence of a spin Nernst effect or, in other words, a thermal spin Hall effect. For this effect, a magnetic field is not needed since the transverse spin current is induced by the spin-orbit interaction. The effect is based on the mechanism that electrons with high energies have a different spin Hall angle than electrons with a low energy. Relatively 'hot' electrons that travel from the hot to the cold region induce therefore (via the spin Hall effect) a different spin current than 'cold' electrons that travel from the cold to the hot region. This leads to a net spin current transverse to the direction of the heat current. Theoretical calculations in mesoscopic cross-bar geometries have shown the existence of this effect [24, 25]. The spin Nernst effect offers the possibility to convert heat currents directly into spin currents, however, experiments that demonstrate the efficiency of this effect are still lacking.

## 2.2 Spin transport in metallic systems

Spintronics, or in full spin-based electronics, is an alternative to electronics in which the angular momentum of the electrons is used instead of its charge [26]. One of the most important achievements that followed from the research field of spintronics is the discovery of the Giant Magnetoresistance (GMR) effect [27, 28]. The GMR effect describes the change of electrical resistance that is observed between the parallel and anti-parallel magnetization configuration of two adjacent ferromagnetic layers. In 2007, the Nobelprize for Physics was awarded to Albert Fert and Peter Grünberg for the discovery of this effect. The fact that every hard disk drive fabricated nowadays includes a read head sensor that utilizes the GMR effect, makes this discovery one of the biggest successes in the field of spintronics so far. The recent progress in flash memory technology applied in solid-state drives (SSD) has become a serious competitor of the GMR based hard drives. Hence, for the field of applied magnetism, it is of vital importance to develop new innovative ways of magnetic memory that offer an alternative to flash memory.

### 2.2.1 Two-current model

The resistance change observed in GMR devices originates from the difference in the density of states for majority and minority spin bands (parallel and anti-parallel to the magnetization) in ferromagnetic metals. Because the density of states at the Fermi level determines the transport properties of the metal, majority and minority spins can have a different conductivity. Hence, spintronic devices consisting of



ferromagnetic metals and non-magnetic materials are often described by a so-called two current model based on diffusive transport which was firstly derived by Valet and Fert [29]. In this model, where all magnetizations are considered to be collinear, electrical transport for majority spins  $J_\uparrow$  (usually called spin-up) and minority spins  $J_\downarrow$  (usually called spin-down) are treated independently. This approach is only justified if the length over which spin information is preserved is much longer than the mean free path of the electrons. The current densities  $J_{\uparrow,\downarrow}$  are related to the electrochemical potential for spin-up and spin-down electrons  $\mu_{\uparrow,\downarrow}$  in the following way:

$$J_{\uparrow,\downarrow} = -\frac{\sigma_{\uparrow,\downarrow}}{e} \nabla \mu_{\uparrow,\downarrow} \quad (2.2)$$

with  $\sigma_{\uparrow,\downarrow}$  the spin-dependent conductivity and  $e$  the electron charge. The spin-dependent conductivity is defined as  $\sigma_{\uparrow,\downarrow} = \sigma(1 \pm P_\sigma)/2$  with  $\sigma = \sigma_\uparrow + \sigma_\downarrow$  and  $P_\sigma$  the conductivity polarization, which is then given by  $P_\sigma = (\sigma_\uparrow - \sigma_\downarrow)/(\sigma_\uparrow + \sigma_\downarrow)$ . Due to the nonzero conductivity polarization in ferromagnets, a charge current ( $J_\uparrow + J_\downarrow$ ) is always accompanied by a spin current (defined as  $J_s = J_\uparrow - J_\downarrow$ ). When a ferromagnet F is electrically connected to a non-magnetic material N, magnetic moments can be transported from the ferromagnet into the non-magnetic region, called spin injection [30]. This happens, for example, if an electrical current is sent from the ferromagnetic through the interface into the non-magnetic region. In the bulk of F, the current is spin-polarized (i.e.  $J_\uparrow \neq J_\downarrow$ ), whereas in the bulk of N the current is unpolarized ( $J_\uparrow = J_\downarrow$ ). Therefore, close to the interface the current has to be converted from a polarized current into an unpolarized current via spin relaxation and as a result, a spin accumulation builds up.

Unlike charge, spin is not conserved within the material and can be lost to or be generated by the environment (e.g. by scatter events with the lattice). These spin relaxation processes, where spins flip their orientation, limit the length scale on which spins can be transported through a material. The spin accumulation, defined as  $\mu_s = \mu_\uparrow - \mu_\downarrow$ , decreases exponentially with distance from the point where it is generated according to the Valet-Fert equation for spin-diffusion [29]:

$$\nabla^2 \mu_s = \frac{\mu_s}{\lambda^2} \quad (2.3)$$

with  $\lambda$  the spin relaxation length of the material.

Interfaces between ferromagnets and non-magnetic materials can be used for the injection and/or detection of electron spins. When a current is sent through such an interface, the spin-dependent potentials split at the interface and spins start to accumulate in a short region close to the interface. In the bulk of the metal, one can define a weighted average electrochemical potential  $\mu_c$ , which reflects the measurable electrochemical potential. Following from the spin-dependent conductivities

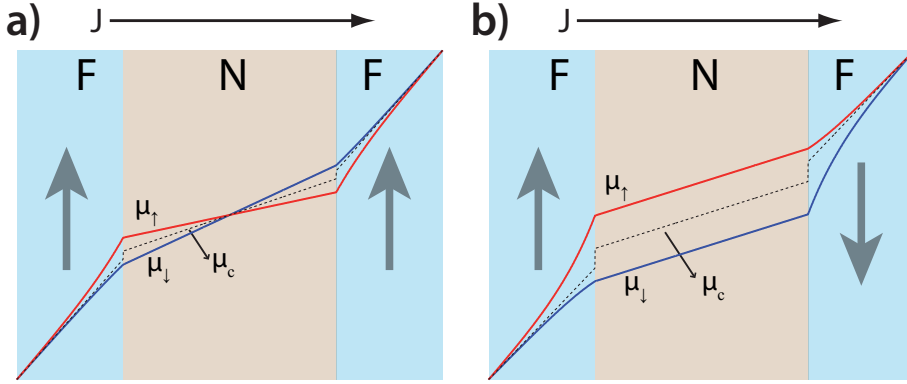


**Figure 2.3:** GMR structure consisting of a nonmagnetic layer (N) sandwiched in between two ferromagnetic layers (F). The gray arrows indicate the magnetization of the ferromagnets. In red and blue, the electrochemical potential for spin-up and spin-down electrons are shown, respectively. The black dotted line reflects the electrochemical potential  $\mu_c$ . (a) Electrochemical potentials for both spin channels in the parallel alignment of the magnetizations when a dc current is applied. The spin accumulation ( $\mu_\uparrow - \mu_\downarrow$ ) is opposite for the two F/N interfaces and zero in the middle of N. (b) In the anti-parallel configuration, the induced spin accumulation is similar at both interfaces and nonzero in the center. Because of the difference in the conductivity for spin-up and spin-down channels in the ferromagnet, the electrochemical potential  $\mu_c$  is not the average of  $\mu_\uparrow$  and  $\mu_\downarrow$ . This leads to a jump in  $\mu_c$  at the interfaces.

$\sigma_{\uparrow,\downarrow}$ , this electrochemical potential is defined as:

$$\mu_c = \frac{\sigma_\uparrow \mu_\uparrow + \sigma_\downarrow \mu_\downarrow}{\sigma_\uparrow + \sigma_\downarrow} \quad (2.4)$$

Hence, the electrochemical potential is not necessarily continuous at the interface between two different materials since the conductivity polarizations can be different on both sides. This leads to an interface potential that scales with the spin accumulation (or splitting of the spin-dependent potential) at the interface as described by van Son *et al.* [31]. Detecting this spin voltage provides a method of measuring a spin accumulation in a nonmagnetic-metal. For non-collinear magnetizations the description of spin transport becomes more complicated and the two current model fails. Circuit theory describes the transport in terms of scattering matrices and provides a more general picture for magnetoelectronic circuits and devices [32].

Figure 2.3 shows an example of the electrochemical potentials for the two spin channels in a GMR device when a current  $J$  is sent through. Such a device consisting of a nonmagnetic layer (N) sandwiched in between two ferromagnetic layers (F) is

called a spin valve. In Fig. 2.3a, the situation is shown for the parallel configuration of the magnetization of the ferromagnetic layers. At the left interface an accumulation of spin-up electrons develops, whereas at the right interface the opposite spin direction accumulates. In the center of N there exists no spin accumulation, however, a spin current is still present. In Fig. 2.3b the opposite situation is displayed where the magnetization are aligned anti-parallel. Here, the spin accumulation in the center is nonzero, but there is no spin current. The dotted black line represents the electrochemical potential  $\mu_c$  which is measurable in an experiment. Due to the conductivity polarization in ferromagnets,  $\mu_c$  lies not exactly in between  $\mu_\uparrow$  and  $\mu_\downarrow$  but is defined by Eq. 2.4. The resulting potential drop at the interfaces is the previously discussed interface potential.

### 2.2.2 Non-local spin valve

Non-local device geometries, where the current paths are spatially separated from the detection circuit, offer a way to study the transport of spins independently from charge currents [33]. These geometries are often utilized for ‘proof of principle’ experiments where pure spin currents (not accompanied by charge currents) are needed. A good example of a non-local spintronic device is the non-local spin valve device (shown in Fig. 2.4a) [34, 35, 36]. Two ferromagnetic elements ( $F_1$  and  $F_2$ ) are connected with each other via a non-magnetic material (N). The current is now not sent from  $F_1$  to  $F_2$ , but is taken out via the N on the left side. The spins that are injected below  $F_1$  can, however, diffuse in both directions. As a result of spin relaxation, the induced spin accumulation in the N (depicted in Fig. 2.4b) decreases exponentially with distance in both directions. The electrochemical potential in the second ferromagnet ( $F_2$ ) depends now on the direction of its magnetization with respect to the spin accumulation and can be used as a detector.

A measurement of the resistance (voltage divided by the current) between  $F_2$  and the N as a function of magnetic field is shown in Fig. 2.4c. In such a typical spin valve measurement, a clear difference is visible between the parallel and anti-parallel alignment of the magnetizations. If the magnetic field is slowly increased in the direction opposite to the magnetizations, the ferromagnetic with the lowest coercive field will switch its magnetization first. A clear jump in the resistance is observed, because the spin accumulation changes sign. At higher field, also the second ferromagnet switches and since now both ferromagnets are in the parallel configuration again, the resistance changes back the original value. The observed nonzero baseline resistance  $(R_P - R_{AP})/2$  originates from a combination of charge transport effects and is discussed in detail in Chapter 3.

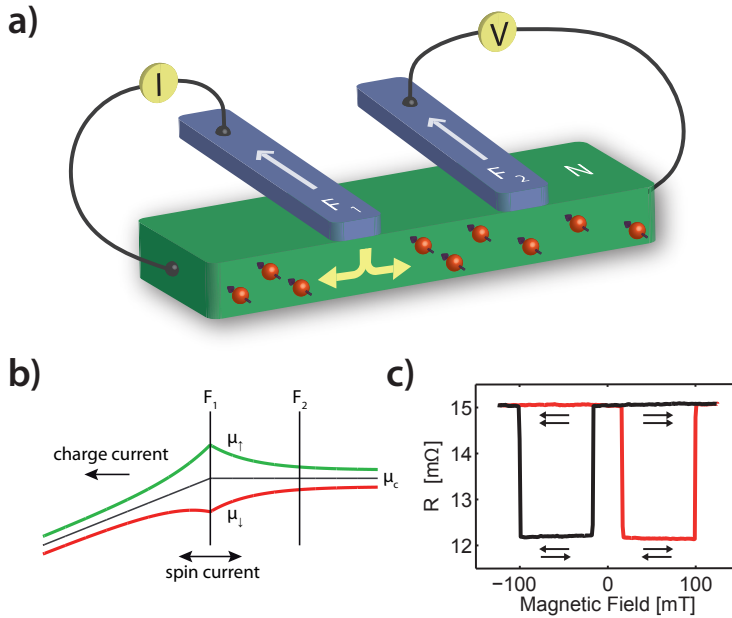


**Figure 2.4:** (a) Basic geometry for a non-local spin valve device where charge and spin currents are spatially separated. Two ferromagnetic elements ( $F_1$  and  $F_2$ ) are connected to a nonmagnetic material ( $N$ ) as indicated. A current is sent from  $F_1$  into the  $N$  and taken out on the left side. A spin accumulation is generated at the interface between  $F_1$  and the  $N$  and diffuses in both directions. Across the interface between  $F_2$  and the  $N$  a voltage evolves depending on the magnitude and direction of the spin accumulation that is present there. (b) Schematic representation of the induced spin accumulation in the  $N$ . (c) Non-local spin valve measurement where the resistance ( $R = V/I$ ) is plotted as a function of the applied magnetic field.

### 2.3 Spin-dependent thermoelectricity

In this section, the theory that combines the previously discussed thermal and spin transport in metallic systems is reviewed. This spin-dependent thermo electricity, or better known as spin-caloritronics [37], is now evolving into a novel research field with many promising applications. Although the coupling between charge, heat and spin currents has been known for some time [38], innovative experiments based on this interaction have not been performed until recently. Progress in nanoscale fabrication techniques that enabled control of heat transport on the nanometer scale

have stimulated the research for these effects and will be the main focus of this thesis.

For the description of heat, charge and spin transport the two-current model developed in Section 2.2.1 needs to be extended to a three current model, thereby including heat transport. The three currents ( $J_\uparrow$ ,  $J_\downarrow$ ,  $Q$ ) are coupled to the spin-up potential, spin-down potential and temperature gradients in the following way [39, 40]:

$$\begin{pmatrix} \vec{J}_\uparrow \\ \vec{J}_\downarrow \\ \vec{Q} \end{pmatrix} = - \begin{pmatrix} \sigma_\uparrow & 0 & \sigma_\uparrow S_\uparrow \\ 0 & \sigma_\downarrow & \sigma_\downarrow S_\downarrow \\ \sigma_\uparrow \Pi_\uparrow & \sigma_\downarrow \Pi_\downarrow & k \end{pmatrix} \begin{pmatrix} \vec{\nabla} V_\uparrow \\ \vec{\nabla} V_\downarrow \\ \vec{\nabla} T \end{pmatrix} \quad (2.5)$$

with  $\sigma_{\uparrow,\downarrow}$  the spin-dependent conductivity,  $\kappa$  the heat conductivity,  $V_{\uparrow,\downarrow} = \mu_{\uparrow,\downarrow}/e$  and where  $S_{\uparrow,\downarrow}$  and  $\Pi_{\uparrow,\downarrow}$  are the spin-dependent Seebeck and Peltier coefficient, respectively. Here, we assumed that the temperatures of both spin directions are equal. This assumption is justified as long as there exists spin-conserving inelastic scattering on a scale much smaller than the device dimensions. For the metals used in our devices and at room temperature, this requirement holds. The regular Seebeck coefficient is defined as  $S = (\sigma_\uparrow S_\uparrow + \sigma_\downarrow S_\downarrow)/\sigma$  which, after rewriting, gives the following definition for the spin-dependent Seebeck coefficient:

$$S_{\uparrow,\downarrow} = S - \frac{1}{2}(P_\sigma \mp 1)S_s \quad (2.6)$$

where we defined  $S_s = S_\uparrow - S_\downarrow$ . The Thomson-Onsager relation applied to the separate spin channels  $\Pi_{\uparrow,\downarrow} = S_{\uparrow,\downarrow}T_0$  gives us the spin-dependent Peltier coefficients. Since the Seebeck coefficient depends on the energy derivative of the conductivity and the density of states of both spin bands is different in ferromagnets, the Seebeck effects for spin-up and spin-down are expected to be different. If  $S_\uparrow \neq S_\downarrow$ , an interesting phenomenon occurs when a temperature gradient is applied to a ferromagnet. In the absence of charge current, a pure spin current develops in the bulk of the ferromagnet given by:

$$J_s = \frac{\sigma}{2}(P_\sigma^2 - 1)S_s \nabla T \quad (2.7)$$

At both ends of the ferromagnetic material this gives rise to a spin accumulation, because the induced spin current is interrupted at the edge. In the bulk the spin accumulation vanishes because of spin relaxation. A functional device can be created by connecting the ferromagnet to a nonmagnetic layer. Figure 2.5 shows the electrochemical potentials of spin-up and spin-down channels at the junction between a ferromagnet and a nonmagnetic conductor when a temperature gradient is applied. Similar to electrical spin injection, a spin accumulation is created at the interface

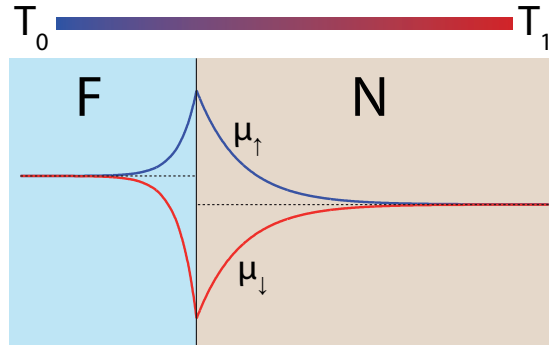


**Figure 2.5:** Modeled electrochemical potential for spin-up and spin-down electrons in an F/N junction subject to a temperature gradient. The temperature difference is set between the two ends of the system and the voltage for both spin channels is set to zero at the left end. For clarity, the conventional Seebeck coefficients are disregarded and only the spin-dependent Seebeck coefficient ( $S_{\uparrow} - S_{\downarrow}$ ) is nonzero. The resulting spin accumulation at the interface leads to splitting of the electrochemical potentials.

which decreases exponentially with distance due to spin relaxation processes. The conventional (charge) Seebeck effects are disregarded in the schematic representation of Fig. 2.5 and will, if taken into account, lead to an extra linear voltage gradient in both materials.

Thermal spin injection has been demonstrated experimentally for the first time by Slachter *et al.* in a device depicted in Fig. 2.6b [39]. Conceptually, a heat current, generated by Joule heating, induces a spin accumulation which is measured using a second ferromagnet placed within the spin relaxation length of N (shown in Fig. 2.6a). The heating of FM<sub>1</sub> leads to a thermal gradient across the F/N interface and causes a splitting of the electrochemical potentials. Depending on the relative orientation of FM<sub>1</sub> and FM<sub>2</sub> the observed spin voltage changes sign. A measurement of  $R_2 = V/I^2$  as a function of the applied magnetic field is shown in Fig. 2.6c. Since  $\nabla T \propto I^2$  (Joule heating),  $V$  is divided by  $I^2$  to obtain a quantity that is independent of the current. For the parallel and anti-parallel configuration of the ferromagnets a different spin voltage is indeed observed, thereby demonstrating the possibility of spin injection with thermal currents. The large baseline resistance is caused by the regular Seebeck effect and discussed in detail in Chapter 3. Magneto-Seebeck effects in magnetic tunnel junctions have also been experimentally observed [41, 42] and modeled [43]. Additionally, thermal spin injection in Si has been demonstrated by Breton *et al.* by using tunnel junctions and a Hanle precession detection

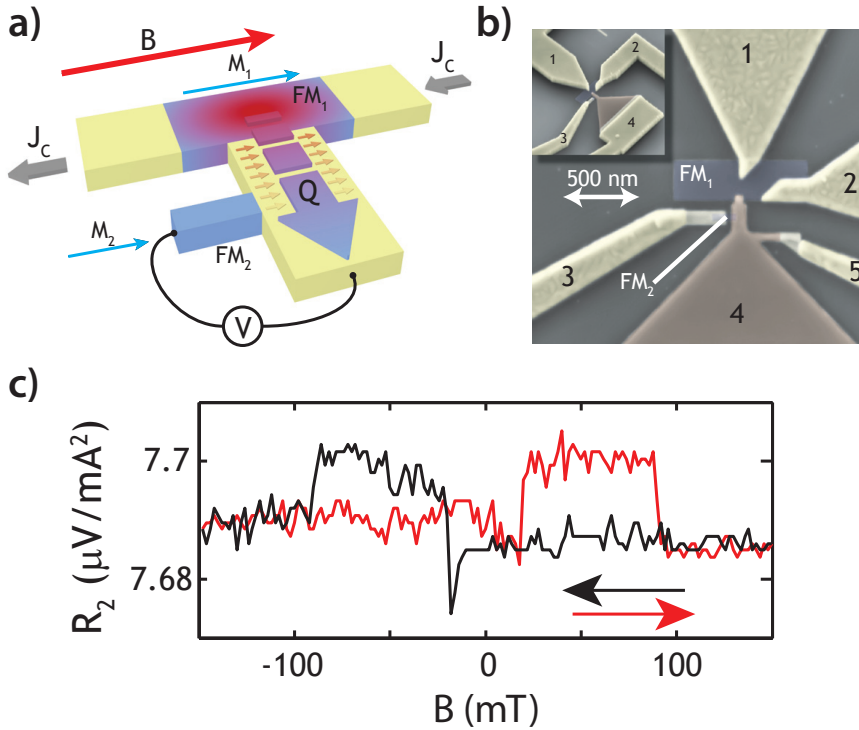


**Figure 2.6:** Figures obtained from Slachter *et al.* [39]. (a) Conceptual representation of thermal spin injection. A thermal gradient is created by heating  $FM_1$  using a charge current. The thermally induced spin accumulation diffuses into the nonmagnetic material (yellow) and is detected by  $FM_2$ . (b) Scanning electron microscopy (SEM) image of the device. A current is sent between contact 1 and 2 and the voltage is detected between contact 3 and 4. (c) Measurement of  $R_2 = V/I^2$  as a function of the applied magnetic field. Clear switches are observed when the configuration of the ferromagnets switches from parallel to anti-parallel.

technique [44].

By Onsager's reciprocity [4], the spin dependency of the Seebeck coefficients give rise to a spin-dependent Peltier effect. This heating or cooling using spin currents is essentially the inverse effect of thermal spin injection and has been theoretically studied by Hatami *et al.* [45]. First experiments performed by Gravier *et al.* on multiple Co/Cu multilayer nanowires have indicated the existence of spin-dependent Peltier coefficients [46, 47]. The cooling or heating using spin currents is one of the main results of this thesis and is discussed in Chapter 4.

## 2.4 3-D Finite element modeling

The 3-D finite element modeling presented in this thesis is performed with the software package Comsol Multiphysics (version 4.1) as described in earlier work [48]. Using the coefficient form for linear or almost linear partial differential equations (PDE's), we defined the physics for charge, heat and spin transport. The fluxes  $\vec{J} = (J_{u_1}, J_{u_2}, \dots)$  are related to the dependent continuous variables  $\vec{u} = (u_1, u_2, \dots)$  by a conduction matrix  $c$  as  $\vec{J} = -c\nabla\vec{u}$ . The PDE's are solved by the conservation of fluxes:

$$\vec{\nabla} \cdot (-c\nabla\vec{u}) = \vec{f} \quad (2.8)$$

where  $\vec{f}$  is a source term which may depend on the variable  $\vec{u}$ . Boundary conditions can be either set for fluxes (Neumann condition) or variables (Dirichlet condition).

For the spin-dependent thermoelectric model as described in Section 2.3, the fluxes  $\vec{J}_\uparrow$ ,  $\vec{J}_\downarrow$  and  $\vec{Q}$  are governed by the variables  $V_\uparrow$ ,  $V_\downarrow$  and  $T$ . The conduction matrix is given by the matrix of Eq. 2.5 and the source term is defined in the following way:

$$\begin{pmatrix} \vec{\nabla} \cdot \vec{J}_\uparrow \\ \vec{\nabla} \cdot \vec{J}_\downarrow \\ \vec{\nabla} \cdot \vec{Q} \end{pmatrix} = \begin{pmatrix} -\frac{(1-P_\sigma^2)\sigma}{4\lambda^2}(V_\uparrow - V_\downarrow) \\ \frac{(1-P_\sigma^2)\sigma}{4\lambda^2}(V_\uparrow - V_\downarrow) \\ J_\uparrow^2/\sigma_\uparrow + J_\downarrow^2/\sigma_\downarrow + \frac{(1-P_\sigma^2)\sigma}{4\lambda^2}V_s^2 \end{pmatrix} \quad (2.9)$$

Although charge is conserved in the model ( $\vec{\nabla} \cdot \vec{J} = 0$ ), spin is definitely not and the source terms for  $\vec{J}_\uparrow$  and  $\vec{J}_\downarrow$  reflect the Valet-Fert equation for spin relaxation in terms of  $\vec{J}_{\uparrow,\downarrow}$ . Here we note that in the original derivation of the Valet-Fert equation from particle conservation, thermoelectricity was not included [49]. As described earlier in Section 2.1.1, the Seebeck effect describes effectively the energy dependence of the conductivity or, via the Einstein relation for metals, the energy dependence of the density of states and the relaxation time at the Fermi energy. By introducing the Seebeck effect into the original derivation for spin relaxation, the energy derivatives of the density of states and the relaxation times need to be taken into account. These energy dependencies lead to extra source terms in Eq. 2.3 that can, in principle, induce bulk spin accumulations [39]. Since not much is known about these energy derivatives and because we expect these effects to be rather small, they are disregarded in the further analysis. The sum of the Joule heating in both spin channels is incorporated in the source term for  $Q$ . Additionally, an extra term is added that describes the heat that evolves due to the relaxation of spins [50]. The next section will discuss this process in more detail.



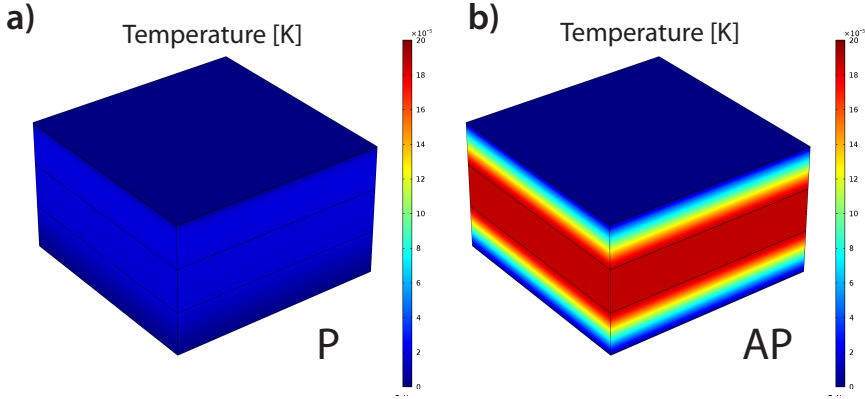


**Figure 2.7:** Model of the dissipation due to spin relaxation in a F/N/F stack. The temperature profile is plotted for a dc current of 1 mA. For clarity, the Joule heating for both channels is disregarded. a) In the parallel configuration, the spin current is almost constant throughout the stack and hence, the spin accumulation is small. Then, the relaxation current is low and there the heating is negligible. b) For the anti-parallel configuration, the situation is opposite and the dissipation due to relaxation is large.

### 2.4.1 Dissipation due to spin relaxation

In Section 2.2.1 it was shown that if a spin accumulation is present, the electrochemical potential for spin-up and spin-down electrons split. During spin relaxation, electrons flip their spin orientation and move from one spin channel into the other. If both spin channel do not have the same electrochemical potential, energy is gained or lost during this process given by the relaxation rate ( $\vec{\nabla} \cdot \vec{J}_s/2$ ) times the potential difference ( $V_\uparrow - V_\downarrow$ ):

$$\nabla \cdot \vec{Q} = \frac{(1 - P_\sigma^2)\sigma}{4\lambda^2}(V_\uparrow - V_\downarrow)^2 \quad (2.10)$$

The factor two in the relaxation rate is to avoid counting each spin flip twice. Obviously, if a spin-up electron disappears a spin-down electron appears, but the corresponding energy is only released or absorbed once.

Based on this principle, a magnetically controllable heating device can be fabricated. Suppose that a current is sent through a F/N/F stack, then the dissipation due to spin relaxation depends strongly on the relative orientation of the magnetizations. For the parallel configuration, the spin accumulation is small (see Fig. 2.3) and there is minor dissipation. In the anti-parallel configuration, however, the spin accumulation is large and the dissipation is maximal. The induced temperature distribution, calculated with the finite element model, is shown in Fig. 2.7

for a situation where Joule heating is disregarded. In this model, which consists of a Py(Ni<sub>80</sub>Fe<sub>20</sub>)/Cu/Py stack, the induced temperature increase is rather small ( $\approx 0.2$  mK) for a current of 1 mA. Nevertheless, the effect is not negligible in GMR stacks and can be of the same order of magnitude as the regular Joule heating. In the Supplementary of Chapter 4 experimental results on this dissipation term will be discussed in more detail.

## 2.5 Novel spin-caloritronic concepts

Recent experimental work on spin-caloritronics has demonstrated the great diversity of this evolving research field. Innovative spin sources as the spin-Seebeck effect in metallic [51], semiconducting [52, 53] and even insulating materials [54] open up new pathways for spintronic applications. The spin Seebeck effect describes the generation of a spin current in a ferromagnet perpendicular to an applied heat current. The detection of the spin current is performed with Pt strips using the inverse spin Hall effect [55, 56]. Although the exact origin of the spin Seebeck effect is still unknown, there are strong indications that the spin current is caused by the non-equilibrium magnon distribution [57, 58]. On the other hand, the coupling with phonons also seems to be an important parameter [59, 60]. Either way, in the study for this effects it is crucial to have knowledge about the exact heat currents in order to be able to distinguish between spin Seebeck effects and anomalous Nernst effects [61]. We stress that the spin Seebeck effect cannot be attributed to the spin dependency of the Seebeck effect, as is the case for the spin-dependent Seebeck effect (discussed in Section 2.3). The spin Seebeck manifests itself over long length scales (in the order of millimeters), whereas the spin-dependent Seebeck effect is only present within the spin-relaxation length from a F/N interface.

Spin caloritronic phenomena offer alternative methods for spin transfer torque in, for instance, spin transfer torque memory devices. Thermal torques replacing electrical spin transfer torques can induce magnetization reversal as earlier theoretical [62, 63] and experimental [64] studies have indicated. Despite the fact that the temperature gradients have to be rather large, by exploiting the waste heat that is generated in electrical devices, it could work even alongside electrical spin transfer torque.

Finally, the coupling of heat transport with magnetization dynamics is still a virtually unexplored area. Chapter 7 describes an experiment where the heat generation during ferromagnetic resonance is measured and can be seen as part of this branch of spin-caloritronics. In the next sections, two novel spin-caloritronics transport concepts are discussed, which are both experimentally not yet demonstrated.

### 2.5.1 Magnetically controllable heat currents

In the previous sections, we assumed that the exchange of energy between electrons in the separate spin bands happens at length scales much smaller than the device dimensions. This exchange of energy can occur directly by inelastic electron-electron interaction or via the phonon system by electron-phonon scattering [65, 63, 66]. For strong energy exchange mechanisms the electron energy distributions of both spin species are always in equilibrium and have the same temperature  $T$ . However, for nanoscale devices and at low temperature this assumption is not completely valid, because of the relatively large inelastic scattering length [67]. It has to be noted that in the limit of very weak inelastic scattering, the transport can still be diffusive, limited by elastic scattering processes. Since the system does not obey Fermi-Dirac statistics anymore in this case, a classical temperature can not be defined. Instead, one could assign a temperature  $T_{\uparrow,\downarrow}$  to the system that represents the local average excess of energy of the spin-up and spin-down electrons, respectively. Moreover, in that situation the electrons from a single spin band do not even exchange energy anymore.

For the case where the energy exchange between the electrons is weak, we can extend the model with a separate temperature for spin-up and spin-down electrons and consequently a spin-dependent thermal conductivity:

$$\begin{pmatrix} \vec{J}_{\uparrow} \\ \vec{J}_{\downarrow} \\ \vec{Q}_{\uparrow} \\ \vec{Q}_{\downarrow} \end{pmatrix} = \begin{pmatrix} \sigma_{\uparrow} & 0 & \sigma_{\uparrow}S_{\uparrow} & 0 \\ 0 & \sigma_{\downarrow} & 0 & \sigma_{\downarrow}S_{\downarrow} \\ \sigma_{\uparrow}\Pi_{\uparrow} & 0 & k_{\uparrow} & 0 \\ 0 & \sigma_{\downarrow}\Pi_{\downarrow} & 0 & k_{\downarrow} \end{pmatrix} \begin{pmatrix} \vec{\nabla}V_{\uparrow} \\ \vec{\nabla}V_{\downarrow} \\ \vec{\nabla}T_{\uparrow} \\ \vec{\nabla}T_{\downarrow} \end{pmatrix} \quad (2.11)$$

A similar model has first been described by Heikkilä *et al.* [65] and later applied to nanoscale devices by Slachter *et al.* [22]. Since in such a system the temperature for the two spin species  $T_{\uparrow}$  and  $T_{\downarrow}$  can be different it offers new device possibilities as for example a heat valve. In this device, consisting of a layer of nonmagnetic metal sandwiched in between two ferromagnetic layers, one can control the heat flow through the stack magnetically by switching between the parallel and anti-parallel configuration of the two ferromagnets.

### 2.5.2 Spin-dependent Thomson effect

The Thomson heat reflects the cooling or heating of a conductor if an electric current is passed through and a temperature gradient is also present [68]. The net heat produced in a conductor per unit volume per second is given by:

$$\nabla \cdot \vec{Q} = \frac{J^2}{\sigma} - \eta J \nabla T \quad (2.12)$$

where the first term is the irreversible Joule heating that depends on the electrical conductivity. The second term is the reversible Thomson heat and depends linearly on the current density  $J$  and temperature gradient  $\nabla T$ . If heat is absorbed or emitted depends then on the direction of the current and the sign of the Thomson coefficient  $\eta$ . The Thomson effect arises from the fact that the Seebeck coefficient  $S$  is in general temperature dependent and  $\eta$  is defined as:

$$\eta = T \frac{dS}{dT} \quad (2.13)$$

The Thomson coefficient differs from the other thermoelectric constants ( $S$  and  $\Pi$ ) in the sense that it is the only one which can be measured for an individual material. Peltier and Seebeck coefficients can only be experimentally obtained from pairs of materials. An integration of Thomson coefficient measurements over a large temperature range enables for determination of absolute values of the Seebeck coefficient.

For similar reasons as for the Seebeck and Peltier coefficients, it is plausible that the Thomson coefficient is different for the majority and minority spins in ferromagnetic materials. The presence of a pure spin current,  $J_S = J_\uparrow - J_\downarrow$ , and temperature gradient  $\nabla T$  in a ferromagnet could therefore lead to a nonzero Thomson heat given by:

$$\nabla \cdot \vec{Q} = -(\eta_\uparrow - \eta_\downarrow) J_S \nabla T \quad (2.14)$$

Experimentally, this effect could be demonstrated in a similar F/N/F multilayer structure to the one discussed in Ch. 4. In addition to the spin dependent Peltier experiment, a temperature gradient needs to be introduced. However, such a measurement is experimentally more challenging, because the spin-dependent Peltier effect could obscure the Thomson heat effect. To overcome these problems, one can for instance make use of a modulation technique for the temperature gradient, while keeping the charge current constant. Introducing an extra source term to describe the Thomson effect in the finite element model will often result in double counting of the Thomson heat, because the Thomson effect is automatically included if the Seebeck coefficients are temperature dependent. Therefore, it is usually better to include the temperature dependencies of the Seebeck and Peltier effects directly into the model.

## 2.6 Summary

The current status of the research field of spin caloritronics has been reviewed in mainly metallic devices and several thermal transport effects are discussed. A diffuse model is developed that combines the basic equations that govern heat and

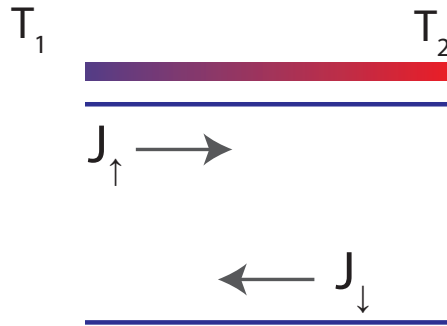


**Figure 2.8:** Concept of the spin-Thomson effect. A pure spin current is flowing in a conductor where a temperature gradient is present. Due to the spin-dependency of the Thomson coefficient, heat is generated or absorbed.

charge transport with the two current model that describes spin transport in metals. A 3D finite element model was introduced that describes spin-dependent thermoelectric effects and the dissipation due to spin relaxation was included. Furthermore, novel caloritronic concepts as magnetically controllable heat currents and the spin-Thomson effect have been discussed.

## Bibliography

- [1] C. Kittel, *Introduction to Solid State Physics -7th ed.*, John Wiley & Sons, Inc., New York, 1995.
- [2] T. Seebeck, "Über die magnetische Polarisation der Metalle und Erze durch Temperatur-Differenz," *Ann. Phys.* **2**(September), pp. 287–292, 1826.
- [3] N. F. Mott and H. Jones, *The Theory of the Properties of Metals and Alloys*, Oxford Univ. Press, London, 1936.
- [4] L. Onsager, "Reciprocal Relations in Irreversible Processes. I.," *Physical Review* **37**, p. 405, 1931.
- [5] H. Callen, "The application of Onsager's reciprocal relations to thermoelectric, thermomagnetic, and galvanomagnetic effects," *Physical Review* **73**(11), p. 1349, 1948.
- [6] D. G. Cahill, W. K. Ford, K. E. Goodson, G. D. Mahan, A. Majumdar, H. J. Maris, R. Merlin, and S. R. Phillpot, "Nanoscale thermal transport," *Journal of Applied Physics* **93**(2), p. 793, 2003.
- [7] F. Giazotto, T. Heikkilä, A. Luukanen, A. Savin, and J. Pekola, "Opportunities for mesoscopies in thermometry and refrigeration: Physics and applications," *Reviews of Modern Physics* **78**, pp. 217–274, Mar. 2006.
- [8] D. Li, S. T. Huxtable, A. R. Abramson, and A. Majumdar, "Thermal Transport in Nanostructured Solid-State Cooling Devices," *Journal of Heat Transfer* **127**(1), p. 108, 2005.
- [9] R. Venkatasubramanian, E. Siivola, T. Colpitts, and B. O'Quinn, "Thin-film thermoelectric devices with high room-temperature figures of merit.," *Nature* **413**, pp. 597–602, Oct. 2001.
- [10] A. I. Boukai, Y. Bunimovich, J. Tahir-Kheli, J.-K. Yu, W. a. Goddard, and J. R. Heath, "Silicon nanowires as efficient thermoelectric materials.," *Nature* **451**, p. 168, Jan. 2008.
- [11] A. Avery, R. Sultan, D. Bassett, D. Wei, and B. Zink, "Thermopower and resistivity in ferromagnetic thin films near room temperature," *Physical Review B* **83**, p. 100401(R), Mar. 2011.
- [12] A. Sugihara, M. Kodzuka, K. Yakushiji, H. Kubota, S. Yuasa, A. Yamamoto, K. Ando, K. Takanashi, T. Ohkubo, K. Hono, and A. Fukushima, "Giant Peltier Effect in a Submicron-Sized CuNi/Au Junction with Nanometer-Scale Phase Separation," *Applied Physics Express* **3**, p. 065204, May 2010.
- [13] W. Sun, H. Liu, W. Gong, L.-M. Peng, and S.-Y. Xu, "Unexpected size effect in the thermopower of thin-film stripes," *Journal of Applied Physics* **110**(8), p. 083709, 2011.
- [14] B. Zink, a.D. Avery, R. Sultan, D. Bassett, and M. Pufall, "Exploring thermoelectric effects and WiedemannFranz violation in magnetic nanostructures via micromachined thermal platforms," *Solid State Communications* **150**, pp. 514–518, Mar. 2010.
- [15] L. Gurevich *J. Phys. USSR* **9**, p. 477, 1945.

- [16] L. Gurevich J. *Phys. USSR* **10**, p. 67, 1946.
- [17] D. K. C. MacDonald and W. B. Pearson, "Thermoelectricity in metals at normal temperatures - a query," *Proceedings of the Physical Society* **78**(2), p. 306, 1961.
- [18] M. V. Costache, G. Bridoux, I. Neumann, and S. O. Valenzuela, "Magnon-drag thermopile," *Nature Materials* **11**, pp. 1–4, Dec. 2011.
- [19] K. Behnia, "The Nernst effect and the boundaries of the Fermi liquid picture," *Journal of Physics: Condensed Matter* **21**, p. 113101, Mar. 2009.
- [20] N. Nagaosa, S. Onoda, a. H. MacDonald, and N. P. Ong, "Anomalous Hall effect," *Reviews of Modern Physics* **82**, pp. 1539–1592, May 2010.
- [21] I. A. Campbell, "The Nernst-Ettinghausen effect in ferromagnetic metals," *Journal of Magnetism and Magnetic Materials* **12**, pp. 31–33, 1979.
- [22] A. Slachter, F. L. Bakker, and B. J. van Wees, "Anomalous Nernst and anisotropic magnetoresistive heating in a lateral spin valve," *Physical Review B* **84**, p. 020412(R), July 2011.
- [23] T. Seki, I. Sugai, Y. Hasegawa, S. Mitani, and K. Takahashi, "Spin Hall effect and Nernst effect in FePt/Au multi-terminal devices with different Au thicknesses," *Solid State Communications* **150**, pp. 496–499, Mar. 2010.
- [24] S.-g. Cheng, Y. Xing, Q.-f. Sun, and X. C. Xie, "Spin nernst effect and nernst effect in two-dimensional electron systems," *Phys. Rev. B* **78**, p. 045302, Jul 2008.
- [25] X. Liu and X. Xie, "Spin Nernst effect in the absence of a magnetic field," *Solid State Communications* **150**, pp. 471–474, Mar. 2010.
- [26] I. Žutić and S. Das Sarma, "Spintronics: Fundamentals and applications," *Reviews of Modern Physics* **76**, pp. 323–410, Apr. 2004.
- [27] G. Binasch, P. Grünberg, F. Saurenbach, and W. Zinn, "Enhanced magnetoresistance in layered magnetic structures with antiferromagnetic interlayer exchange," *Physical review. B, Condensed matter* **39**, p. 4828, Mar. 1989.
- [28] M. N. Baibich, J. M. Broto, A. Fert, F. Van Dau, F. Petroff, P. Etienne, G. Creuzet, A. Friederich, and J. Chazelas, "Giant magnetoresistance of (001) Fe/(001) Cr magnetic superlattices," *Physical Review Letters* **61**(21), pp. 2472–2475, 1988.
- [29] T. Valet and A. Fert, "Theory of the perpendicular magnetoresistance in magnetic multilayers," *Physical Review B* **48**, p. 7099, 1993.
- [30] A. Aronov, "Spin injection in metals and polarization of nuclei," *JETP Lett.* **24**, p. 32, 1976.
- [31] P. V. Son, H. V. Kempen, and P. Wyder, "Boundary resistance of the ferromagnetic-nonferromagnetic metal interface," *Physical Review Letters* **58**, p. 2271, 1987.
- [32] A. Brataas, G. Bauer, and P. Kelly, "Non-collinear magnetoelectronics," *Physics Reports* **427**, pp. 157–255, Apr. 2006.
- [33] S. O. Valenzuela, "Nonlocal Electronic Spin Detection, Spin Accumulation and the Spin Hall Effect," *International Journal of Modern Physics B* **23**(11), p. 2413, 2009.

- [34] F. J. Jedema, A. T. Filip, and B. J. van Wees, "Electrical spin injection and accumulation at room temperature in an all-metal mesoscopic spin valve.," *Nature* **410**, p. 345, Mar. 2001.
- [35] F. J. Jedema, H. B. Heersche, A. T. Filip, J. J. A. Baselmans, and B. J. van Wees, "Electrical detection of spin precession in a metallic mesoscopic spin valve.," *Nature* **416**, p. 713, Apr. 2002.
- [36] M. Johnson and R. H. Silsbee, "Interfacial charge-spin coupling: Injection and detection of spin magnetization in metals," *Physical Review Letters* **55**, p. 1790, Oct. 1985.
- [37] G. E. Bauer, A. H. MacDonald, and S. Maekawa, "Spin Caloritronics," *Solid State Communications* **150**, pp. 459–460, Mar. 2010.
- [38] M. Johnson and R. Silsbee, "Thermodynamic analysis of interfacial transport and of the thermomagnetolectric system," *Physical Review B* **35**(10), p. 4959, 1987.
- [39] A. Slachter, F. L. Bakker, J.-P. Adam, and B. J. van Wees, "Thermally driven spin injection from a ferromagnet into a non-magnetic metal," *Nature Physics* **6**, pp. 879–882, Sept. 2010.
- [40] L. Gravier, S. Serrano-Guisan, F. Reuse, and J.-P. Ansermet, "Thermodynamic description of heat and spin transport in magnetic nanostructures," *Physical Review B* **73**, p. 024419, Jan. 2006.
- [41] N. Liebing, S. Serrano-Guisan, K. Rott, G. Reiss, J. Langer, B. Ocker, and H. Schumacher, "Tunneling Magnetothermopower in Magnetic Tunnel Junction Nanopillars," *Physical Review Letters* **107**, p. 177201, Oct. 2011.
- [42] M. Walter, J. Walowski, V. Zbarsky, M. Münzenberg, M. Schäfers, D. Ebke, G. Reiss, A. Thomas, P. Peretzki, M. Seibt, J. S. Moodera, M. Czerner, M. Bachmann, and C. Heiliger, "Seebeck effect in magnetic tunnel junctions.," **10**, pp. 742–746, July 2011.
- [43] M. Czerner, M. Bachmann, and C. Heiliger, "Spin caloritronics in magnetic tunnel junctions: Ab initio studies," *Physical Review B* **83**, p. 132405, Apr. 2011.
- [44] J.-C. Le Breton, S. Sharma, H. Saito, S. Yuasa, and R. Jansen, "Thermal spin current from a ferromagnet to silicon by Seebeck spin tunnelling," *Nature* **475**, pp. 82–85, June 2011.
- [45] M. Hatami, G. Bauer, Q. Zhang, and P. Kelly, "Thermoelectric effects in magnetic nanostructures," *Physical Review B* **79**, p. 174426, May 2009.
- [46] L. Gravier, A. Fábíán, A. Rudolf, A. Cachin, J.-E. Wegrowe, and J.-P. Ansermet, "Spin-dependent thermopower in Co/Cu multilayer nanowires," *Journal of Magnetism and Magnetic Materials* **271**, pp. 153–158, May 2004.
- [47] L. Gravier, S. Serrano-Guisan, F. Reuse, and J.-P. Ansermet, "Spin-dependent Peltier effect of perpendicular currents in multilayered nanowires," *Physical Review B* **73**, p. 052410, Feb. 2006.
- [48] A. Slachter, F. L. Bakker, and B. J. van Wees, "Modeling of thermal spin transport and spin-orbit effects in ferromagnetic/nonmagnetic mesoscopic devices," *Physical Review B* **84**, p. 174408, Nov. 2011.
- [49] F. Jedema, *Electrical Spin Injection in metallic Mesoscopic Spin Valves*. PhD thesis, University of Groningen, 2002. ISBN 90-367-1724-8.



- [50] A. Tulapurkar and Y. Suzuki, "Boltzmann approach to dissipation produced by a spin-polarized current," *Physical Review B* **83**, p. 012401, Jan. 2011.
- [51] K. Uchida, S. Takahashi, K. Harii, J. Ieda, W. Koshibae, K. Ando, S. Maekawa, and E. Saitoh, "Observation of the spin Seebeck effect.," *Nature* **455**, p. 778, Oct. 2008.
- [52] C. M. Jaworski, J. Yang, S. Mack, D. D. Awschalom, J. P. Heremans, and R. C. Myers, "Observation of the spin-Seebeck effect in a ferromagnetic semiconductor.," *Nature materials* **9**, pp. 898–903, Nov. 2010.
- [53] S. Bosu, Y. Sakuraba, K. Uchida, K. Saito, T. Ota, E. Saitoh, and K. Takanashi, "Spin Seebeck effect in thin films of the Heusler compound  $\text{Co}_{-}\{2\}\text{MnSi}$ ," *Physical Review B* **83**, p. 224401, June 2011.
- [54] K. Uchida, J. Xiao, H. Adachi, J. Ohe, S. Takahashi, J. Ieda, T. Ota, Y. Kajiwara, H. Umezawa, H. Kawai, G. E. W. Bauer, S. Maekawa, and E. Saitoh, "Spin Seebeck insulator.," *Nature materials* **9**, p. 894, Nov. 2010.
- [55] T. Kimura, Y. Otani, T. Sato, S. Takahashi, and S. Maekawa, "Room-Temperature Reversible Spin Hall Effect," *Physical Review Letters* **98**, p. 156601, Apr. 2007.
- [56] S. O. Valenzuela and M. Tinkham, "Direct electronic measurement of the spin Hall effect.," *Nature* **442**, p. 176, July 2006.
- [57] J. Xiao, G. Bauer, K.-c. Uchida, E. Saitoh, and S. Maekawa, "Theory of magnon-driven spin Seebeck effect," *Physical Review B* **81**, p. 214418, June 2010.
- [58] H. Adachi, J.-i. Ohe, S. Takahashi, and S. Maekawa, "Linear-response theory of spin Seebeck effect in ferromagnetic insulators," *Physical Review B* **83**, p. 094410, Mar. 2011.
- [59] H. Adachi, K.-i. Uchida, E. Saitoh, J.-i. Ohe, S. Takahashi, and S. Maekawa, "Gigantic enhancement of spin Seebeck effect by phonon drag," *Applied Physics Letters* **97**(25), p. 252506, 2010.
- [60] K. Uchida, H. Adachi, T. An, T. Ota, M. Toda, B. Hillebrands, S. Maekawa, and E. Saitoh, "Long-range spin Seebeck effect and acoustic spinpumping.," *Nature materials* **10**, pp. 737–741, Aug. 2011.
- [61] S. Huang, W. Wang, S. Lee, J. Kwo, and C. Chien, "Intrinsic Spin-Dependent Thermal Transport," *Physical Review Letters* **107**, p. 216604, Nov. 2011.
- [62] Y. Takezoe, K. Hosono, A. Takeuchi, and G. Tatara, "Theory of spin transport induced by a temperature gradient," *Physical Review B* **82**, p. 094451, Sept. 2010.
- [63] M. Hatami, G. Bauer, Q. Zhang, and P. Kelly, "Thermal Spin-Transfer Torque in Magnetoelectronic Devices," *Physical Review Letters* **99**, p. 066603, Aug. 2007.
- [64] H. Yu, S. Granville, D. P. Yu, and J.-P. Ansermet, "Evidence for Thermal Spin-Transfer Torque," *Physical Review Letters* **104**, p. 146601, Apr. 2010.
- [65] T. T. Heikkilä, M. Hatami, and G. E. W. Bauer, "Spin heat accumulation and its relaxation in spin valves," *Physical Review B* **81**, p. 100408(R), Mar. 2010.

- [66] T. T. Heikkilä, M. Hatami, and G. E. Bauer, “Electron-electron interaction induced spin thermalization in quasi-low-dimensional spin valves,” *Solid State Communications* **150**, pp. 475–479, Mar. 2010.
- [67] H. Pothier, S. Guéron, N. O. Birge, D. Esteve, and M. H. Devoret, “Energy distribution function of quasiparticles in mesoscopic wires,” *Phys. Rev. Lett.* **79**, pp. 3490–3493, Nov 1997.
- [68] D. K. C. MacDonald, *Thermoelectricity, An introduction to the Principles*, Dover Publications, Inc., Mineola, New York, 2006.

## Chapter 3

---

# Interplay of Peltier and Seebeck effects in nanoscale nonlocal spin valves

### Abstract

*We have experimentally studied the role of thermoelectric effects in nanoscale nonlocal spin valve devices. A finite element thermoelectric model is developed to calculate the generated Seebeck voltages due to Peltier and Joule heating in the devices. By measuring the first, second and third harmonic voltage response non locally, the model is experimentally examined. The results indicate that the combination of Peltier and Seebeck effects contributes significantly to the nonlocal baseline resistance. Moreover, we found that the second and third harmonic response signals can be attributed to Joule heating and temperature dependencies of both Seebeck coefficient and resistivity.*

## 3.1 Introduction

The Seebeck and the related Peltier effects are the fundamental phenomena of thermoelectricity, a field subject to extensive research during the previous decades [1]. Although these are bulk material properties, they can be utilized to measure the temperature or to generate heat locally at or close to an interface between different materials. While progress in nanoscale device fabrication has made it possible to study these phenomena at continuously decreasing length scales, they are rarely taken into account to analyze electrical measurements in nanostructures. In the specific field of spintronics, a detailed understanding of the interaction between heat transport and the charge and spin degrees of freedom is highly required [2]. This emerging branch, called *spin caloritronics* [3], has recently drawn considerable attention [4, 5, 6, 7, 8], and (spin-) thermoelectric effects have been experimentally examined in magnetic multilayer nanostructures [6, 7] and in macroscopically large ferromagnetic strips [8]. In this Letter, we use lateral nonlocal spin valve devices as a tool to study the interplay between heat, charge and spin at the nanoscale. The non-local device design enables us to separate the charge and heat current, and hence, excludes spurious effects. We find that the baseline resistance in nonlocal spin valve

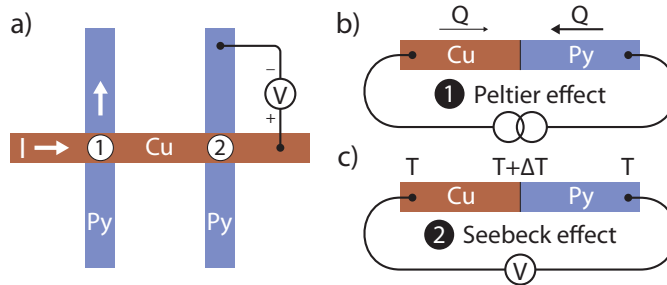


**Figure 3.1:** (a) Schematic drawing of a typical spin valve experiment. Current is sent through the first Cu/Py interface, while the voltage drop is measured at the second interface. (b) Due to the difference in the Peltier coefficients for Cu and Py, the heat current  $Q$  carried by the electrons changes across the interface. Hence, interface 1 is locally heated or cooled depending on the direction of the current. (c) The second interface acts as a thermocouple and detects the local electron temperature via the Seebeck effect.

measurements originates mainly from Peltier heating/cooling at the injector junction and the Seebeck effect at the detector junction. Furthermore, we demonstrate that it is experimentally feasible to use basic thermoelectrics to obtain control over the heat flow in nanostructures.

## 3.2 Nonlocal voltage detection

The nonlocal spin valve experiment is schematically depicted in Fig. 3.1a. Two permalloy (Py) electrodes are overlapped with a Cu strip, creating two ferromagnetic/nonmagnetic metal (F/N) interfaces. Electrical spin injection across a F/N interface is well-described in terms of a two current model [9, 10] and was demonstrated experimentally [11, 12]. Here, a spin current is injected into the Cu strip by sending a charge current through the first F/N interface (Fig. 3.1a). A spin voltage can be detected at the second interface provided that the spacing between injector and detector is shorter than the spin relaxation length of the Cu [12].

Ideally, the voltage detected at the second interface in the nonlocal geometry will be zero in the absence of a spin accumulation. Since the current and voltage path are completely separated, one expects no Ohmic voltage drop at interface 2 (Fig. 3.1a). The voltage arising from a spin accumulation is bipolar, having equal magnitude but opposite sign for the parallel and antiparallel alignment of both ferromagnets. However, the baseline resistance observed in experiments, defined as the resistance in the absence of spin-related effects, is in general nonzero [12]. Current spreading

at the injector can account for an Ohmic resistance at the detector, as discussed by Johnson and Silsbee [13]. The resulting voltage  $V_r$  is found to depend exponentially on the separation  $L$  between the two interfaces as  $V_r \propto e^{-\pi L/W}$ , with  $W$  the width of the Cu strip. Moreover, spin dependent scattering at the detector interface [14] has been invoked to explain an offset voltage, but both effects are not sufficient to describe the data accurately.

Here we address a new origin of the baseline resistance, composed of thermoelectric phenomena which are generally disregarded in the analysis. We show that the Peltier and the related Seebeck effect, when combined in a lateral nanostructure, give rise to a significant modification of the baseline resistance.

### 3.3 Peltier and Seebeck effects

If an electrical current  $I$  flows through a Cu/Py interface, heat accumulates or is absorbed at the interface due to the mismatch of the Peltier coefficients. The heat current carried by the electrons, represented by the Peltier coefficient, is different on both sides of the interface. Since the charge current is continuous across the interface, the heat current has a discontinuity. Consequently, the interface is heated or cooled depending on the sign of the current (Fig. 3.1b). The inverse process, called the Seebeck effect, refers to the generation of a voltage by a temperature gradient. This effect can be exploited to probe the local electron temperature at or close to the interface, similar to the functioning of a thermocouple (Fig. 3.1c). As copper is an excellent thermal conductor, the heat generated at interface 1 can be efficiently transferred to interface 2 and is then, via the Seebeck effect, translated back into a voltage.

In order to quantify the Peltier and Seebeck effects a 3D thermoelectric finite element model (FEM) is developed. The charge current density  $J$  and the heat current density  $Q$  in these nanostructures can be related to the voltage and temperature in the following way:

$$\begin{pmatrix} \vec{J} \\ \vec{Q} \end{pmatrix} = - \begin{pmatrix} \sigma & \sigma S \\ \sigma \Pi & \kappa \end{pmatrix} \begin{pmatrix} \vec{\nabla} V \\ \vec{\nabla} T \end{pmatrix} \quad (3.1)$$

with  $\sigma$  the electrical conductivity,  $\kappa$  the thermal conductivity,  $S$  the Seebeck coefficient and  $\Pi = ST_0$  the Peltier coefficient.  $T_0$  is the reference temperature of the device and taken to be 300K. The charge and heat currents are taken to be continuous across the boundaries and at the end of all contacts we set the temperature at  $T_0$ . Joule heating and charge conservation is incorporated via  $\nabla Q = J^2/\sigma$  and  $\nabla J = 0$ . We use a separate two-current model to calculate the spin signals by introducing spin-dependent conductivities  $J_{\uparrow,\downarrow} = -\sigma_{\uparrow,\downarrow}/e\nabla\mu_{\uparrow,\downarrow}$ , with  $\sigma_{\uparrow,\downarrow}$  and  $\mu_{\uparrow,\downarrow}$  the

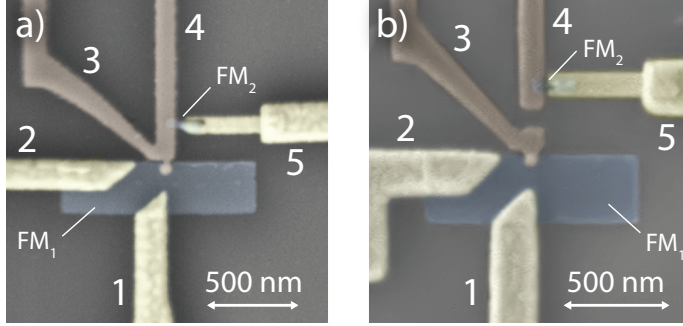


**Figure 3.2:** Scanning Electron Microscope (SEM) image of the device lay-out. (a) Standard nonlocal spin valve geometry. Current is sent from contact 1 to 3, while the voltage is measured between 5 and 4. Contact 2 is not used. (b) Similar device geometry with an electrically isolated detector circuit.

spin-dependent conductivity and electrochemical potential, respectively [9, 10, 15]. Bulk spin relaxation is introduced via  $\nabla J_{\uparrow,\downarrow} = \mp \frac{(1-P^2)\sigma}{4e\lambda} (\mu_{\uparrow} - \mu_{\downarrow})$ , with  $\lambda$  the spin relaxation length and  $P$  the conductivity polarization given by  $\frac{\sigma_{\uparrow} - \sigma_{\downarrow}}{\sigma_{\uparrow} + \sigma_{\downarrow}}$ .

### 3.4 Experimental realization

Two batches of lateral nonlocal spin valve devices were fabricated on a thermally oxidized Si substrate in a five-step e-beam lithography process. Fig. 3.2 shows the scanning electron microscope (SEM) images of the two types of devices. A device consists of two 15 nm thick Py islands, a large injector  $FM_1$  ( $1 \mu\text{m} \times 300 \text{ nm}$ ) and a small detector  $FM_2$  ( $150 \text{ nm} \times 50 \text{ nm}$ ), separated from each other by a distance  $L$ . Both ferromagnets are contacted on one side with Au electrodes and with a 60 nm thick Cu strip on the other side. To reduce Joule heating in the leads, the Au contacts on  $FM_1$  have a thickness of 170 nm. The metallic layers are deposited using an e-beam evaporator with a base pressure of  $1 \times 10^{-6}$  mbar. Prior to deposition of Au and Cu the interfaces are cleaned by Ar ion milling to assure good Ohmic interfaces.

We use a lock-in amplifier for detecting the voltage  $V$  across the Cu/ $FM_2$  interface, between contact 5 and 4 (Fig. 3.2). Simultaneously an AC current  $I$  is sent from contact 1 to 3. If the response of the system is nonlinear, the higher order terms can be extracted separately by measuring the higher harmonics:

$$V = R_1 I + R_2 I^2 + \dots \quad (3.2)$$

with  $R_i$  ( $i = 1, 2, \dots$ ) the  $i$ -th harmonic ‘resistance’ response. The current is applied

at a frequency below 1 kHz, much lower than the relevant time scales for thermal conduction in these nanostructures. All electrical measurements are performed at room temperature.

### 3.5 First, second and third harmonic response

The first harmonic response  $R_1$ , reflects the sum of the baseline resistance and a resistance due to the presence of a spin accumulation. The magnetic field dependence of  $R_1$  is shown in Fig. 3.3b, with  $R_{1s}$  the spin valve signal and  $R_{1b}$  defined as the baseline resistance. To examine the distance dependence as proposed by Johnson and Silsbee [13],  $R_1$  is measured for device type 1 (Fig. 3.2a) with different  $L$ , varying between 75 and 900 nm. The baseline resistance is plotted in Fig. 3.3a. If we neglect thermoelectric effects, the baseline is expected to decrease exponentially as  $R_{1b} \propto e^{-\pi L/W}$ , with  $W$  the width of the Cu contact. The data clearly shows an exponential decrease of resistance for small  $L$ , but decays more slowly for larger separations. Note that the spin valve voltage shows only an exponential dependence due to spin relaxation in the Cu (shown in Fig. 3.3c). Assuming that  $\lambda_F = 5$  nm for Py, we deduce from our spin-dependent two-current model the spin relaxation length of Cu and bulk conductivity polarization of Py to be 350 nm and 25%, respectively.

For the same set of samples, the magnetic field dependence of the higher harmonic responses  $R_2$  and  $R_3$  is investigated for  $L = 200$  nm (shown in Fig. 3.4a and 3.4b). In addition to a nonzero baseline, we observe a spin voltage in  $R_2$  and  $R_3$  as well. The baseline is measured as a function of the separation  $L$  between the two ferromagnets and the result is shown in Fig. 3.4c and 3.4d. We find that for  $R_{2b}$  the exponential relation to  $L$  is absent, whereas  $R_{3b}$  shows similar behavior as  $R_{1b}$ , decreasing exponentially for short  $L$  and having a much weaker decay for larger separations.

In the following, we show that the observed baselines of  $R_{1b}$ ,  $R_{2b}$  and  $R_{3b}$  can be attributed to the Peltier and Seebeck effect. The voltage at the detector can be written as the sum of the spin voltage, a resistive part ( $V_r$ ) and a Seebeck voltage. For these devices two important sources of heat exist, Peltier heating at the injector interface and Joule heating in the entire current path. Heat is carried away by thermal transport through the metallic leads and via the SiO<sub>2</sub> substrate and consequently, a temperature gradient evolves in the vicinity of FM<sub>2</sub>. The generated Seebeck voltage is proportional to a combination of the Seebeck coefficients of Py, Cu and Au and the temperature gradients in the detector circuit. This circuit can essentially be seen as a thermocouple with an effective Seebeck coefficient  $S$ .

In contrast to Peltier heating, being linear with  $I$ , Joule heating scales as  $\Delta T \propto I^2$ .

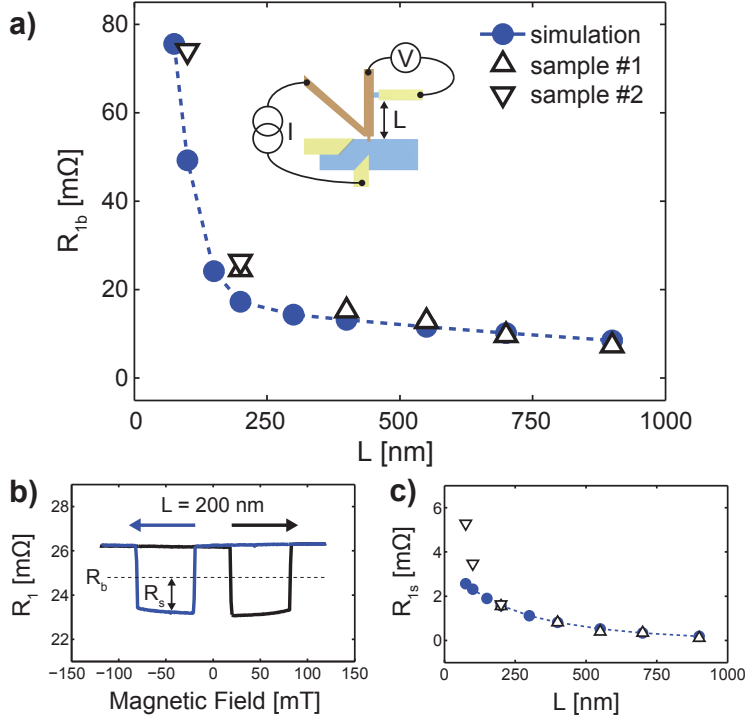


**Figure 3.3:** (a)  $R_{1b}$  measured as a function of the spacing  $L$  between the two ferromagnets, as indicated by the measurement geometry in the inset. The triangles reflect measurements taken for two different samples, whereas the blue dots correspond to the FEM calculations. (b) Nonlocal spin valve measurement with the magnetic field swept back and forth, being indicated by the arrows.  $R_{1s}$  is defined as the resistance due to the presence of a spin accumulation and  $R_{1b}$  is the baseline resistance. (c)  $R_{1s}$  as a function of the separation  $L$  between both ferromagnets.

Hence, the thermoelectric contribution to the baseline,  $S\Delta T$ , originates from Peltier heating for  $R_1$  and from Joule heating for  $R_2$ . In order to explain the observed baseline voltage in  $R_3$ , we introduce a temperature dependent Seebeck coefficient and resistance. In a linear approximation the temperature dependent Seebeck coefficient is written as  $S(T) = S_0(1 + \zeta\Delta T)$ , where  $\Delta T$  the local temperature increase and  $\zeta = 1/T_0$  [16]. The resistivity of a metal increases with temperature as  $\rho(T) = \rho_0(1 + \alpha\Delta T)$ , where  $\alpha$  is in the order of  $10^{-3} \text{ K}^{-1}$  for most metals [17]. Now,  $R_{3b}$  refers to the sum of the changes in Seebeck coefficient and resistance due to Joule



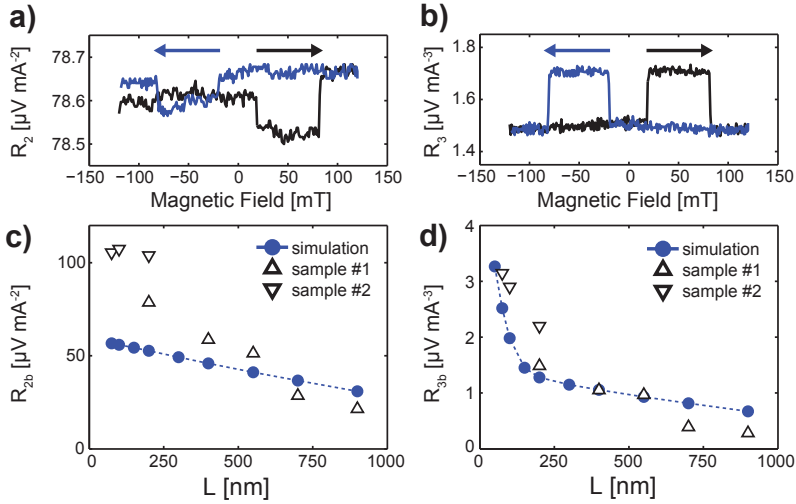


**Figure 3.4:** (a)  $R_2$  as a function of magnetic field. The baseline resistance is mainly caused by the Seebeck voltage induced by Joule heating. (b)  $R_3$  plotted versus magnetic field. The baseline reflects the modification in Seebeck coefficient and resistance due to temperature changes. Likewise, the spin signal indicates how the spin valve signal is altered by temperature. (c) Baseline resistance  $R_{2b}$  as a function of  $L$ . Triangles represent data for two different samples, blue dots are simulation results. (d)  $R_{3b}$  measured versus  $L$ . The shape of  $R_{3b}$  is similar to  $R_{1b}$  because it describes the temperature dependence of the effects that generate  $R_{1b}$ .

heating. Hence,  $R_{3b}$  enables us to study these temperature dependencies directly over a small temperature range of 20K, the highest achievable temperature raise by Joule heating in our devices.  $R_{3b}$  shows similar behavior as  $R_{1b}$ , since  $R_{3b}$  describes essentially the temperature dependence of  $R_{1b}$ . Moreover,  $R_{2b}$  is slightly modified by Peltier heating combined with a temperature dependent Seebeck coefficient and resistance. Nevertheless, we do not find an exponential relationship between  $R_{2b}$  and  $L$ , indicating that the Joule heating induced Seebeck voltage is dominating.

Furthermore, we observe a spin voltage in the higher harmonic responses (shown in Fig. 3.4a and 3.4b). The spin signal in  $R_2$  can be associated both with the temperature dependence of the spin valve signal ( $R_{1s}$ ) and with the spin-dependent Seebeck effect. However, the observed signal has the opposite sign and contradicts with earlier measurements [5, 12, 14]. The exact origin may be found in the spin-dependent Peltier effect [6] or interface scattering [18]. The spin signal in  $R_3$  reflects the change in the spin valve signal caused by Joule heating. From this measurement, we can

**Table 3.1:** Material parameters

Material	$\sigma$ [S/m]	S [ $\mu$ V/K]	$\kappa$ [W/mK]
SiO <sub>2</sub>	0	–	1
Au	$2.2 \times 10^7$	1.7 [17]	300
Cu	$4.3 \times 10^7$	1.6 [17]	300
Py	$4.3 \times 10^6$	–20 [8]	30

derive the spin valve temperature dependence  $\gamma$ , defined as  $R_s(T) = R_s(1 - \gamma\Delta T)$ . We found a  $\gamma$  of approximately 1%, in good agreement with earlier results [12, 14].

The magnitudes of the induced Seebeck voltages have been calculated with the thermoelectric model using Comsol Multiphysics. To obtain the linear response voltage, we have used the parameters presented in Tab. 3.1 [17]. Heat conduction through the substrate is taken into account by assuming a total SI thickness of 1  $\mu$ m. The model includes both charge and heat currents and reproduces the behavior of  $R_{1b}$  remarkably well (Fig. 3.3a, blue dots). For short  $L$ , we find an exponential decrease in the baseline resistance, as discussed previously. For larger separations, calculations show that the baseline diminishes more moderately due to thermoelectric effects. We also incorporated the temperature dependence of the resistance and Seebeck coefficient into our thermoelectric model and the simulations are displayed in Fig. 3.4c and 3.4d. The slope obtained from the simulation of  $R_{2b}$  deviates from the measured data by approximately a factor two. Therefore, we deduce that the Joule heating in the device is two times larger than expected. This discrepancy is ascribed to the oxidation of the Py and the interface resistance of the Au contacts, thereby reducing the thermal conduction. For the calculation of  $R_{3b}$ , we corrected for this, and obtained a perfect agreement between the simulation of  $R_{3b}$  and the experimental data.

To confirm our analysis we excluded charge current effects completely. Therefore, we have measured a similar device with an interrupted Cu strip as shown in Fig. 3.2b. Heat conduction can still occur through the SiO<sub>2</sub>, but charge transport is eliminated. We found a nonzero baseline resistance of 1.85 m $\Omega$  for  $L = 300$  nm, significantly smaller than without the interruption. This change is mainly due to the difference in thermal conductivity between SiO<sub>2</sub> and Cu. FEM calculations predicted a resistance  $R_{1b}$  of 1.9 m $\Omega$ , in perfect agreement with the observed value. For  $R_{2b}$  we found 3.75  $\mu$ V/mA<sup>2</sup>, compared to 4.4  $\mu$ V/mA<sup>2</sup> for the calculations.

## 3.6 Conclusion

In conclusion, we have demonstrated that thermoelectric effects play an important role in nanoscale spin valve devices and lead to a significant increase in baseline resistance. These effects have been employed to locally raise and probe the electron temperature at the interface of two materials and the experimental results are in good agreement with basic thermoelectric rules. By probing the second and third harmonic response separately, higher order thermal effects are observed. In general, these findings open new possibilities for future caloritronic applications using localized electron temperature control.

## Bibliography

- [1] R. D. Barnard, *Thermoelectricity in Metals and Alloys*, Taylor and Francis LTD., London, 1972.
- [2] S. O. Valenzuela, "Nonlocal electronic spin detection, spin accumulation and the spin hall effect.," *International Journal of Modern Physics B: Condensed Matter Physics; Statistical Physics; Applied Physics* **23**(11), pp. 2413 – 2438, 2009.
- [3] G. E. W. Bauer, A. H. MacDonald, and S. Maekawa, "Spin caloritronics," *Solid State Communications* **150**(11-12), pp. 459 – 460, 2010.
- [4] Y. Dubi and M. Di Ventra, "Thermospin effects in a quantum dot connected to ferromagnetic leads," *Phys. Rev. B* **79**, p. 081302, Feb 2009.
- [5] A. Slachter, F. L. Bakker, J.-P. Adam, and B. J. van Wees, "Thermally driven spin injection from a ferromagnet into a non-magnetic metal," *Nature Physics* **6**, pp. 879–882, Sept. 2010.
- [6] L. Gravier, S. Serrano-Guisan, F. Reuse, and J.-P. Ansermet, "Spin-dependent peltier effect of perpendicular currents in multilayered nanowires," *Phys. Rev. B* **73**, p. 052410, Feb 2006.
- [7] Y. Hai-Ming, S. Granville, Y. Da-Peng, and J.-P. Ansermet, "Second harmonic detection of spin-dependent transport in magnetic nanostructures," *Chinese Physics Letters* **27**(2), p. 027201, 2010.
- [8] K. Uchida, S. Takahashi, K. Harii, J. Ieda, W. Koshibae, K. Ando, S. Maekawa, and E. Saitoh, "Observation of the spin seebeck effect," *Nature* **455**, pp. 778–781, 2008.
- [9] P. C. van Son, H. van Kempen, and P. Wyder, "Boundary resistance of the ferromagnetic-nonferromagnetic metal interface," *Phys. Rev. Lett.* **58**, pp. 2271–2273, May 1987.
- [10] T. Valet and A. Fert, "Theory of the perpendicular magnetoresistance in magnetic multilayers," *Phys. Rev. B* **48**, pp. 7099–7113, Sep 1993.
- [11] M. Johnson and R. H. Silsbee, "Interfacial charge-spin coupling: Injection and detection of spin magnetization in metals," *Phys. Rev. Lett.* **55**, pp. 1790–1793, Oct 1985.
- [12] F. J. Jedema, A. T. Filip, and B. J. van Wees, "Electrical spin injection and accumulation at room temperature in an all-metal mesoscopic spin valve," *Nature* **410**, pp. 345–348, 2001.
- [13] M. Johnson and R. H. Silsbee, "Calculation of nonlocal baseline resistance in a quasi-one-dimensional wire," *Phys. Rev. B* **76**, p. 153107, Oct 2007.
- [14] S. Garzon, I. Žutić, and R. A. Webb, "Temperature-dependent asymmetry of the nonlocal spin-injection resistance: Evidence for spin nonconserving interface scattering," *Phys. Rev. Lett.* **94**, p. 176601, May 2005.
- [15] L. Gravier, S. Serrano-Guisan, F. Reuse, and J.-P. Ansermet, "Thermodynamic description of heat and spin transport in magnetic nanostructures," *Phys. Rev. B* **73**, p. 024419, Jan 2006.
- [16] N. F. Mott and H. Jones, *The Theory of the Properties of Metals and Alloys*, Oxford Univ. Press, London, 1936.

- 
- [17] C. Kittel, *Introduction to Solid State Physics -7th ed.*, John Wiley & Sons, Inc., New York, 1995.
- [18] M. Hatami, G. E. W. Bauer, Q. Zhang, and P. J. Kelly, "Thermoelectric effects in magnetic nanostructures," *Phys. Rev. B* **79**, p. 174426, May 2009.



## Chapter 4

---

# Direct observation of the spin-dependent Peltier effect

### Abstract

The Peltier coefficient describes the amount of heat that is carried by an electrical current when it passes through a material [1]. When two materials with different Peltier coefficients are placed in contact with each other, the Peltier effect causes a net flow of heat either towards or away from the interface between them. Spintronics [2] describes the transport of electric charge and spin angular momentum by separate spin-up and spin-down channels in a device. The observation that spin-up and spin-down charge transport channels are able to transport heat independently of each other [3] has raised the possibility that spin currents could be used to heat or cool the interface between materials with different spin-dependent Peltier coefficients. Here, we report the direct observation of the heating and cooling of such an interface by a spin current. We demonstrate this spin-dependent Peltier effect in a spin-valve pillar structure that consists of two ferromagnetic layers separated by a non-ferromagnetic metal. Using a 3-D finite element model, we extract spin-dependent Peltier coefficients in the range of  $-0.9$  to  $-1.3$  mV for permalloy. The magnetic control of heat flow could prove useful for the cooling of nanoscale electronic components or devices [4].

## 4.1 Introduction

Spin caloritronics [5] is a new field that combines concepts from thermoelectricity, such as the Peltier effect, and spintronics. The coupling of heat transport with spintronics [2] has generated novel ideas such as innovative spin sources [6, 7, 8, 9, 10], thermal spin-transfer torque [11, 12], magnetic heat valves [13], Seebeck effects in magnetic tunnel junctions [14, 15] and magnetically switchable cooling [16, 17]. In particular, pioneering experiments by Gravier *et al.* on multiple Co/Cu multilayer nanowires have indicated the existence of spin-dependent Peltier coefficients [3], based on magnetothermoelectric voltage measurements. However, direct experimental evidence for cooling or heating by spin currents has not been reported.

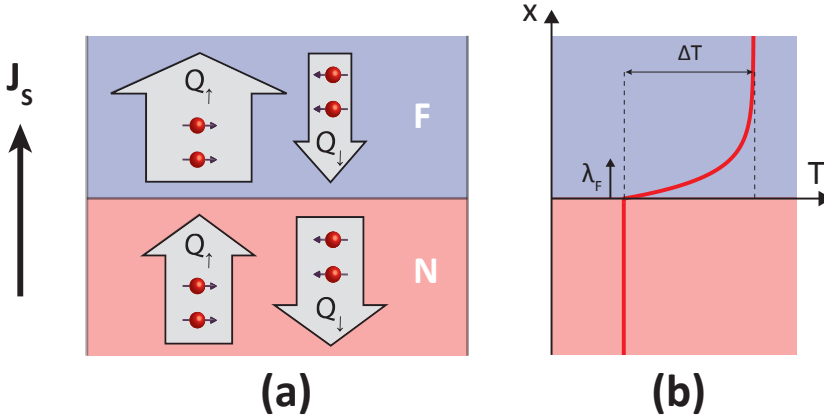


**Figure 4.1:** (a) A pure spin current is sent through a nonmagnetic metal (N) / ferromagnetic metal (F) interface. In the N, the Peltier heat current for both spin species is equal. As the flow direction in the two spin channels is opposite, the total heat current is canceled. In ferromagnets, the heat currents are different for majority and minority carriers, leading to a net heat current from the interface into the ferromagnetic region or vice versa. (b) Generated temperature profile in the system. Spin relaxation in the ferromagnet reduces the spin current, thereby decreasing the induced heat current.

The spin-dependent Peltier effect is based on the ability of the spin-up and spin-down channels to transport heat independently [3]. Figure 4.1a gives a schematic presentation of this concept when a pure spin current ( $J_{\uparrow} = -J_{\downarrow}$ ) passes through a nonmagnetic metal / ferromagnetic metal (N/F) interface. The associated Peltier heat current  $Q_{\Pi}$  is the sum of that of the two spin channels. Since both travel in opposite directions (the charge flow is zero), a net heat flow will only arise if the amount of heat carried by the separate spin species is different. The Peltier coefficients for majority and minority electrons, defined as  $\Pi_{\uparrow,\downarrow} = Q_{\uparrow,\downarrow}/J_{\uparrow,\downarrow}$ , represent the amount of heat carried by the individual spin channels. In N, both coefficients are equal ( $\Pi_{\uparrow} = \Pi_{\downarrow}$ ). However, in the ferromagnet the spin-dependent Peltier coefficient, defined as  $\Pi_s = \Pi_{\uparrow} - \Pi_{\downarrow}$ , is expected to be nonzero [16]. Owing to spin flip processes, the spin current attenuates in the ferromagnet and within a few spin relaxation lengths ( $\lambda_F$ ) from the interface, the Peltier heat current vanishes. Consequently, heat is effectively transferred from the interface into the ferromagnetic region over a finite length (or vice versa), thereby producing a temperature gradient (depicted in Figure 4.1b) and a temperature drop  $\Delta T$ .



## 4.2 Concept of the experiment

In order to demonstrate the effect experimentally, a pure spin current is not required, but it can be accompanied by a charge current  $J_C = J_\uparrow + J_\downarrow$ . To calculate the temperature gradient, the total heat current  $Q = Q_\Pi - \kappa \nabla T$  is evaluated where  $\kappa$  is the thermal conductivity of the electron and phonon systems and  $Q_\Pi = \Pi_\uparrow J_\uparrow + \Pi_\downarrow J_\downarrow$  is the Peltier heat current. If we assume that no heat can enter or leave the stack ( $Q = 0$ ) and disregard Joule heating, the temperature gradient can be expressed as the sum of the charge and spin part of the Peltier effect (see Section 4.5.1). For the spin part, the induced temperature difference between the F/N interface and the bulk of the ferromagnet is given by:

$$\Delta T = \frac{\sigma}{4\kappa} (1 - P^2) \Pi_s \mu_s^0 \quad (4.1)$$

where  $\sigma = \sigma_\uparrow + \sigma_\downarrow$  is the conductivity,  $P_\sigma = (\sigma_\uparrow - \sigma_\downarrow) / \sigma$  the conductivity polarization and  $\mu_s^0 = \mu_\uparrow^0 - \mu_\downarrow^0$  the spin accumulation at the interface. Therefore, we find that the induced temperature drop depends directly on the spin accumulation at the F/N interface.

The device used to study the spin-dependent Peltier effect consists of a stack of two ferromagnetic layers separated by a layer of N (Fig. 4.2). Assuming that the spin relaxation length  $\lambda_N$  is much larger than the thickness of N, we can neglect spin relaxation in N. A charge current  $J_C$  is sent through the stack and the temperature at the top is anchored at  $T_0$ . When both ferromagnets are aligned parallel (P), the spin current is constant over the whole stack and there is no non-equilibrium spin-accumulation, i.e.  $\mu_s = 0$  everywhere. The temperature follows a zigzag pattern [3], caused by the conventional (charge) Peltier effect (Fig. 4.2a). In the anti-parallel (AP) alignment, the situation is different. Now the spin current in the bulk of  $F_1$  is opposite to the spin current in the bulk of  $F_2$ , leading to a spin accumulation at the interfaces [18]. According to Eq. 4.1, this gives rise to an additional temperature difference  $\Delta T$  (Fig. 4.2b) for each F/N interface in the stack. Hence, the induced difference in temperature at the bottom layer between both magnetic configurations is now  $2\Delta T$  (Fig. 4.2c).

The specifically designed device used to study the spin-dependent Peltier effect is depicted in Fig. 4.3. It consists of a permalloy (Py) ( $\text{Ni}_{80}\text{Fe}_{20}$ ) / copper / Py spin valve stack ( $150 \times 80 \text{ nm}^2$  cross section) with a platinum (Pt) bottom contact and a gold (Au) top contact. Cross linked polymethyl methacrylate (PMMA) forms the insulating layer between these two contacts forcing the applied current through the spin valve stack. To probe the temperature of the device a constantan ( $\text{Ni}_{45}\text{Cu}_{55}$ ) - Pt thermocouple is used, where constantan is chosen because of its large Seebeck coefficient ( $-32 \mu\text{V K}^{-1}$ ), see Table 4.1 in Section 4.5.6). The thermocouple is electrically

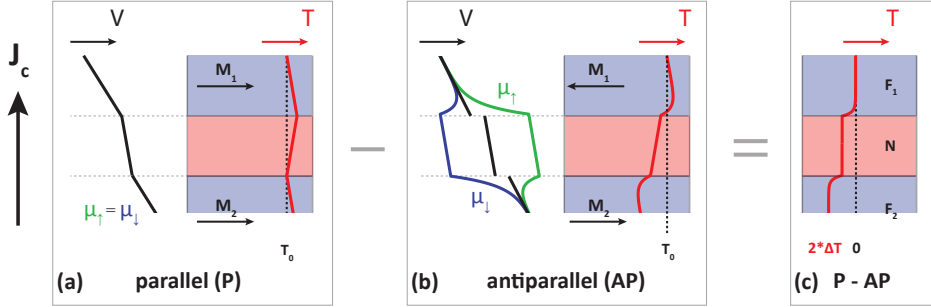


**Figure 4.2:** Schematic figure showing the spin electrochemical potential and temperature throughout the stack for the parallel (P) and anti-parallel (AP) configuration of the ferromagnets. Note that the splitting between  $\mu_{\uparrow}$  and  $\mu_{\downarrow}$  and the heat profile at the F/N interfaces have been exaggerated for clarity (see Section 4.5.2 for the actual electrochemical potential profile extracted from the modeling). Spin-up/spin-down is defined as the spin direction of the majority/minority electrons in  $F_2$ . (a) In the P situation, the spin current in the bulk of both ferromagnets equals the spin current in the N and no non-equilibrium spin-accumulation exists. Hence, there is no spin-dependent Peltier effect. (b) For the AP configuration, the bulk spin currents in  $F_1$  and  $F_2$  are opposite. The resulting spin accumulation at the F/N interface leads to a spin-dependent Peltier contribution and hence, an altered temperature gradient. (c) The spin-dependent Peltier effect causes the temperature at the bottom contact to change between the P and AP alignment.

isolated from the bottom contact by an 8 nm thick aluminum-oxide layer, thereby excluding any spurious voltage pickup. In the measurement a current is sent from contact 1 to 2 through the stack, while recording the thermocouple voltage between contacts 3 and 4. For the 4-point spin valve signal measurements contacts 5 and 6 are used to probe the voltage. Using an ac lock-in measurement technique it is possible to separate the Peltier contribution ( $\Delta T \propto I$ ) and the Joule heating contribution ( $\Delta T \propto I^2$ ) by taking the first harmonic  $V^{(1f)}$  and second harmonic  $V^{(2f)}$  response, respectively [19, 20]. The measurements are performed at room temperature.

### 4.3 Spin-dependent Peltier measurement

The thermovoltage is recorded while sweeping the magnetic field in the in plane direction from negative to positive and back. Figure 4.4a shows the first harmonic response data with  $R_{3-4}^{(1f)}$  defined as  $V_{3-4}^{(1f)}/I$ . The data shows four abrupt changes in  $R_{3-4}^{(1f)}$  when the magnetization of the Py layers switches from P to AP and back.

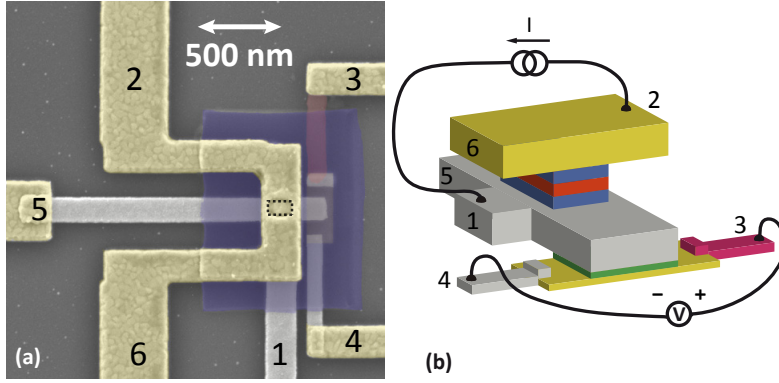


**Figure 4.3:** (a) Scanning electron microscopy image of the measured device. The colors represent the different materials used. Yellow: Au top contact, grey: Pt bottom contacts, blue: cross linked PMMA, red: constantan ( $\text{Ni}_{45}\text{Cu}_{55}$ ). (b) Schematic representation of the device. Current is sent from contact 1 to 2, while recording the voltage between contacts 3 and 4. Contacts 1, 2, 5 and 6 are used for four probe spin valve measurements. The thermocouple is electrically isolated from the bottom contact by an  $\text{Al}_2\text{O}_3$  (green) layer.

A spin signal,  $R_P - R_{AP}$ , of  $-80 \mu\Omega$  is observed on top of a background signal,  $(R_P + R_{AP})/2$ , of  $-0.44 \text{ m}\Omega$ . This corresponds to a temperature difference at the thermocouple between P and AP alignment of around 3 mK at 1 mA. Using the modeling described below we calculated that  $2\Delta T = 7.6 \text{ mK}$  (Eq. 4.1). The second harmonic data is presented in Fig. 4.4b where  $R_{3-4}^{(2f)} = V_{3-4}^{(2f)}/I^2$  and gives a spin signal of  $110 \text{ mV A}^{-2}$  on a background of  $-11.73 \text{ V A}^{-2}$ . This signal originates from the Joule heating [21] in the device and its change between the P and AP configuration (see Section 4.5.3).

The 4-probe spin valve signal shown in Fig. 4.4c gives a  $-100 \text{ m}\Omega$  spin signal. By matching the spin valve signal from our 3-D finite element model [17] to this measured value, we obtain a conductivity polarization ( $P_\sigma$ ) of 0.61, which is close to the bulk value for Py [22, 23]. The same model can now be used to extract the spin-dependent Peltier coefficient,  $\Pi_s = \Pi_\uparrow - \Pi_\downarrow$ , from the first harmonic measurement in Fig. 4.4a. The previously obtained value for  $P_\sigma$  together with the electrical conductivities, thermal conductivities, spin relaxation lengths, the Peltier coefficients and Seebeck coefficients for each material are taken as input parameters (see Table 4.1 in Section 4.5.6).

From the spin-dependent Peltier signal in Fig. 4.4a, we then obtain a spin-dependent Peltier coefficient for Py of  $\Pi_s = -0.9 \text{ mV}$ . Similar results were obtained in two

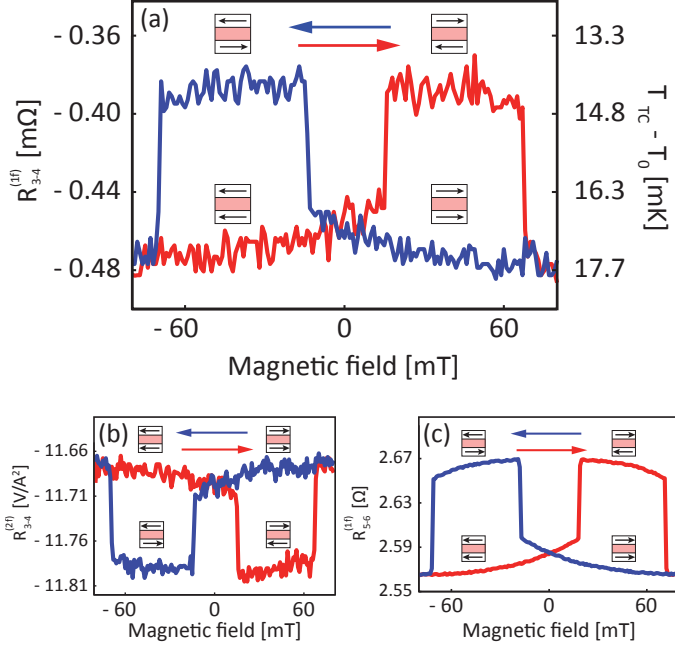


**Figure 4.4:** (a) First-harmonic response signal,  $R_{3-4}^{(1f)} = V_{3-4}^{(1f)}/I$ , measured at the thermocouple with a root mean square current of 1 mA. Switches in  $R_{3-4}^{(1f)}$  are observed when the magnetization of the ferromagnetic layers changes from parallel to anti-parallel and back. On the right y-axis the temperature detected by the NiCu - Pt thermocouple relative to the reference temperature  $T_0$  is given, using  $T - T_0 = V_{3-4}^{(1f)}/(S_{\text{NiCu}} - S_{\text{Pt}})$ . (b) Second-harmonic response signal,  $R_{3-4}^{(2f)} = V_{3-4}^{(2f)}/I^2$ , measured at the thermocouple. (c) Spin valve measurement on the same device.  $R_{5-6}^{(1f)}$  is determined by recording the 4-probe resistance of the stack using contacts 1,2, 5 and 6.

other devices giving values for the spin-dependent Peltier coefficient of  $-1.1$  and  $-1.3$  mV (see Section 4.5.4). The Thomson-Onsager relation applied to the separate spin channels  $\Pi_{\uparrow,\downarrow} = S_{\uparrow,\downarrow}T$  gives us a way to compare these values of  $\Pi_s$  to the previously reported [9] spin-dependent Seebeck coefficient ( $S_s = S_{\uparrow} - S_{\downarrow}$ ) of  $-3.8 \mu\text{V K}^{-1}$ . Using  $\Pi_s = S_s T$  and by taking  $T = 300$  K, we get values for  $S_s$  between  $-3.0 \mu\text{V K}^{-1}$  and  $-4.3 \mu\text{V K}^{-1}$  from our measurements, which is in agreement with ref. [9].

The observed background signal in the first harmonic measurement, due to the conventional Peltier effect, is a factor of 3 lower than we obtain from the modeling. We attribute this difference to difficulties with accurately determining the combina-

tion of Peltier effects for all the interfaces in the current path. Given these uncertainties we allow for the possibility that the actual value of the spin-dependent Peltier coefficient can be slightly higher than obtained from the current modeling.

To confirm that the spin-dependent Peltier effect is indeed the origin of the spin signal, the same device was measured at 77K (see Section 4.5.5). No spin signal could be observed in the measurement as expected from the temperature dependence of  $\Pi_s \propto T^2$ . This dependence is obtained by taking  $S(T) \propto T$  in the Thomson-Onsager relation and gives an upper bound of  $-0.1$  mV for  $\Pi_s$  from the observed noise level at 77K.

## 4.4 Conclusion

In conclusion, we experimentally demonstrated a magnetically controllable heat current, driven by the spin-dependency of the Peltier coefficient. The relatively low efficiency of this effect in ferromagnetic metals restricts the cooling or heating power of the device. For use in applications the effect can possibly be enhanced by the use of nonmetallic materials. Spin-dependent Peltier coefficients that are an order of magnitude larger than that in Py bring the achievable temperature differences in the range of a few Kelvin. With electronic components becoming smaller and smaller the need for local and programmable refrigeration devices is growing and possibly the spin-dependent Peltier effect can fulfill this role.

## 4.5 Supplementary Information

### 4.5.1 Calculation of the temperature gradient

We first derive an expression for the Peltier coefficient of the separate spin channels  $\Pi_{\uparrow,\downarrow}$  in terms of the conventional Peltier coefficient  $\Pi$  and the conductivity polarization  $P_\sigma = (\sigma_\uparrow - \sigma_\downarrow)/\sigma$ . In the bulk of the ferromagnet  $\nabla\mu_\uparrow = \nabla\mu_\downarrow = \nabla\mu_c$  and the Peltier heat current can be written as the sum of that of the separate spin channels,  $-\Pi_\uparrow\sigma_\uparrow\nabla\mu_\uparrow - \Pi_\downarrow\sigma_\downarrow\nabla\mu_\downarrow = -\Pi\sigma\nabla\mu_c$ , where we use  $J_c = -\sigma\nabla\mu_c$  and  $J_{\uparrow,\downarrow} = -\sigma_{\uparrow,\downarrow}\nabla\mu_{\uparrow,\downarrow}$  as the definitions of the electrochemical potentials  $\mu_c$  and  $\mu_{\uparrow,\downarrow}$ . Using the spin-dependent conductivities  $\sigma_{\uparrow,\downarrow} = \frac{\sigma}{2}(1 \pm P_\sigma)$ , we obtain  $\Pi = \frac{\sigma_\uparrow\Pi_\uparrow + \sigma_\downarrow\Pi_\downarrow}{\sigma}$ . Rewriting the result gives us the relation for the Peltier coefficients for majority and minority electrons:

$$\Pi_{\uparrow,\downarrow} = \Pi - \frac{1}{2}(P_\sigma \mp 1)\Pi_s \quad (4.2)$$

where we define  $\Pi_s = \Pi_\uparrow - \Pi_\downarrow$  as the spin-dependent Peltier coefficient.

Next, we derive an expression for the temperature gradient that develops in the ferromagnetic region for the general case when a spin current is accompanied by a charge current  $J_c = J_\uparrow + J_\downarrow$ . The Peltier heat current is given by  $Q_\Pi = \Pi_\uparrow J_\uparrow + \Pi_\downarrow J_\downarrow$  and the temperature gradient is calculated by considering the total heat current in the ferromagnet  $Q = Q_\Pi - \kappa \nabla T$ , where  $\kappa$  describes the thermal conductivity of the electron and phonon system. For simplicity, we assume that no heat can enter or leave the stack ( $Q = 0$ ) and disregard Joule heating. Then we can write  $\nabla T = \frac{1}{\kappa} (\Pi_\uparrow \sigma_\uparrow \nabla \mu_\uparrow + \Pi_\downarrow \sigma_\downarrow \nabla \mu_\downarrow)$  and from the definition of the spin-dependent conductivity and the Peltier coefficients for majority and minority electrons, we find:

$$\nabla T = -\frac{\sigma}{\kappa} (\Pi \nabla \mu_c + \frac{1}{4} (1 - P_\sigma^2) \Pi_s \nabla \mu_s) \quad (4.3)$$

with  $\Pi$  the charge Peltier coefficient and  $\mu_s = \mu_\uparrow - \mu_\downarrow$  the spin accumulation. The electrochemical potential is here derived from current conservation  $J_c = J_\uparrow + J_\downarrow = \sigma \nabla \mu_c$  and by substitution of  $J_{\uparrow,\downarrow}$  with  $-\sigma_{\uparrow,\downarrow} \nabla \mu_{\uparrow,\downarrow}$ , we write  $\nabla \mu_c = \frac{\sigma_\uparrow \nabla \mu_\uparrow + \sigma_\downarrow \nabla \mu_\downarrow}{\sigma}$ .

The first term of Eq. 4.3 describes the conventional Peltier effect in the absence of spin accumulation. The second term describes what happens if a spin accumulation is present in the ferromagnet. According to Eq. 4.3, this gives rise to an additional temperature gradient which depends exclusively on the gradient of the spin accumulation in the ferromagnetic layer and is therefore magnetically controllable. Since spin relaxation forces the spin accumulation to decrease exponentially in the ferromagnetic region [24], we can write  $\mu_s = \mu_s^0 \exp(-x/\lambda_F)$  with  $\lambda_F$  the spin relaxation length. The conventional Peltier term leads to a constant temperature gradient independent of the spin accumulation. By integrating only the spin-dependent Peltier term of Eq. 4.3, we obtain a temperature difference between the F/N interface and the bulk of the ferromagnet of:

$$\Delta T = \frac{\sigma}{4\kappa} (1 - P^2) \Pi_s \mu_s^0 \quad (4.4)$$

where  $\mu_s^0$  is the spin accumulation at the interface. Here we find that the induced temperature drop depends directly on the spin accumulation at the F/N interface.

## 4.5.2 Electrochemical potential profile extracted from the modeling

In the temperature profile we obtain from the modeling, the small temperature change due to the spin-dependent Peltier effect is not visible as the much larger Joule heating and (charge Peltier) heating disguise it. For this reason we do not show the temperature profile here. In Figure 4.5, the modeling results of the electrochemical potential for the individual spin channels are shown.

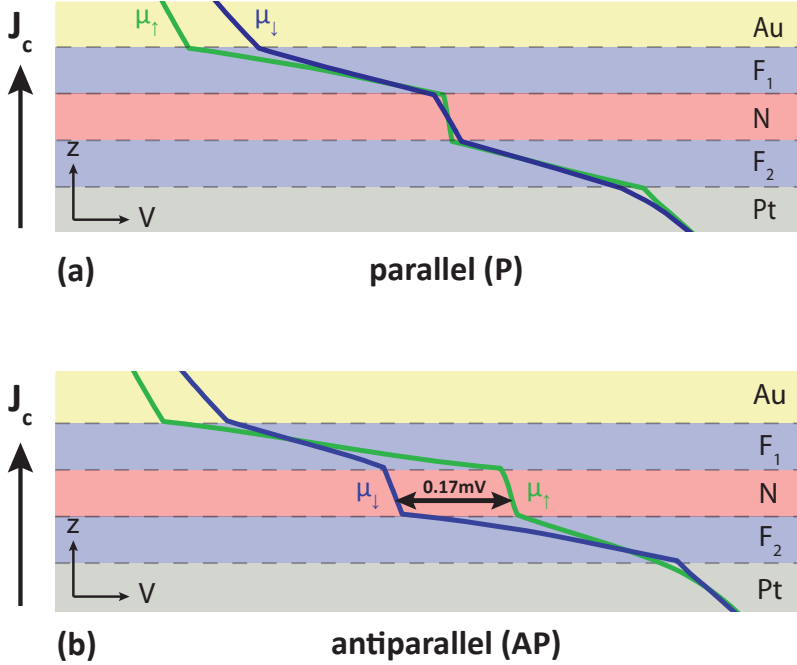


**Figure 4.5:** Spin electrochemical potentials extracted from the modeling. The spin electrochemical potentials throughout the stack for the parallel (P) and anti-parallel (AP) configuration of the ferromagnets as given by the modeling (rms current of 1 mA). Going from the P to AP configuration the magnetization of the  $F_2$  layer is reversed. (a) Parallel configuration. (b) Anti-parallel configuration.

### 4.5.3 Second harmonic response (Joule heating)

The second harmonic response signal (see Fig. 4.6) originates from Joule heating in the device and is proportional to  $I^2R$ . This dependence on  $R$  causes a change in Joule heating [17, 19] when the resistance of the spin valve stack changes from the P to AP configuration and vice versa. Changes in Joule heating in the spin valve stack are picked up by the thermocouple and show up in the second harmonic response measurement,  $R_{3-4}^{(2f)}$ , as they depend on  $I^2$ . In our model we explicitly take in to account the heat generation due to energy dissipation related to spin relaxation [21]. From the model we then obtain the background and spin signal, which are approximately two times higher than observed in the measurement. We explain this by in-

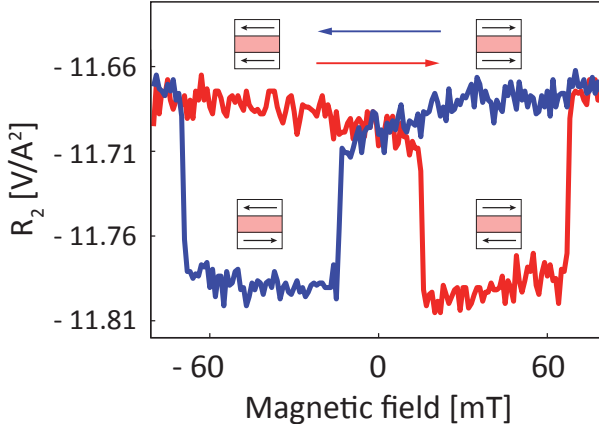


**Figure 4.6:** Joule heating measurement. Second-harmonic response signal,  $R_{3-4}^{(2f)} = V_{3-4}^{(2f)} / I^2$ , measured at the thermocouple with a root mean square current of 1 mA.

efficiency in the temperature sensing, owing to the discrepancy between modeling parameters and the actual, experimental values. Moreover, a big part of the background Joule heating takes place in the Pt bottom contact. The cross linked PMMA, not included in the modeling, covers this contact thereby lowering the background Joule heating signal.

#### 4.5.4 Results for two other samples

The spin-dependent Peltier measurements were performed on two other samples of the same batch and are presented in Fig. 4.7. The first sample (Fig. 4.7a) shows a spin-dependent Peltier signal of  $-100 \mu\Omega$  on a background of  $-0.55 \text{ m}\Omega$  and the second (Fig. 4.7b) a  $-110 \mu\Omega$  spin-dependent Peltier signal on a  $-0.56 \text{ m}\Omega$  background. These values are somewhat higher than for the sample discussed in the main text. The observed variation can be attributed to a slightly higher efficiency of the thermocouple of these samples and/or small differences in thermal anchoring, aluminum oxide thickness and lithographic alignment. The switching that is observed prior to sweeping through zero field is due to interaction between the magnetic dipole fields of the two Py layers, which favors an AP alignment. The sample to sample variation of the switching field position has been seen in several batches for different experiments and can be attributed to for instance small variations in cross section of the pillar. Extracting the spin-dependent Peltier coefficient from this data in the same way as discussed in the main text gives values for  $\Pi_s$  of  $-1.1$  and  $-1.3 \text{ mV}$ .



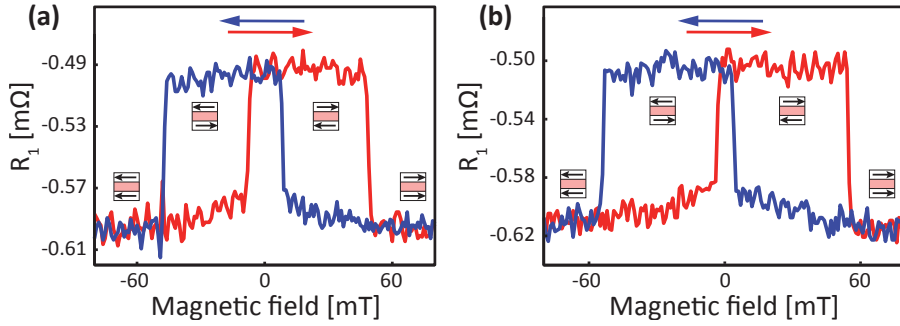


**Figure 4.7:** Spin-dependent Peltier measurements for two other samples. First-harmonic response signal,  $R_{3-4}^{(1f)} = V_{3-4}^{(1f)}/I$ , measured at the thermocouple with a root mean square current of 1 mA. In (a) the results for sample 2 are shown and in (b) those for sample 3.

#### 4.5.5 Measurements at 77K

The presented measurements were repeated on the same sample at liquid nitrogen temperature (77K). This was done to confirm that the first harmonic spin signal is indeed caused by the spin dependency of the Py Peltier coefficient. From the Thomson-Onsager relation,  $\Pi_{\uparrow,\downarrow} = S_{\uparrow,\downarrow}T$ , together with the fact that the Seebeck coefficient shows a dependency on temperature, it becomes clear that  $\Pi_s$  and thereby the spin-dependent Peltier effect will decrease when lowering the temperature. The spin-dependent Peltier measurement at 77K is presented in Fig. 4.8a and shows no difference between P and AP alignment. The disappearance of the spin signal at low temperature supports our conclusion that the room temperature spin signal can be attributed to the spin-dependent Peltier effect. At the same time the background signal, which originates from the conventional Peltier effect, remains almost the same. This can be explained by the fact that for the spin-dependent Peltier effect only the Peltier coefficient of Py plays a role whereas for the Peltier background the difference between all the Peltier coefficients in the current path are important. The Peltier coefficient is proportional to the Seebeck coefficient ( $\Pi = ST$ ) whose temperature dependence does not have to be the same for different materials. Together with a change in thermal conductance between different temperatures it is possible for the regular Peltier effect contribution to not show a decrease when going from room temperature to 77K.

The spin valve measurement shown in Fig. 4.8c shows a decrease in background resistance due to an increase of the conductivities at lower temperatures. The bigger spin signal that is observed is caused by the spin relaxation lengths increasing with lowering of the temperature.

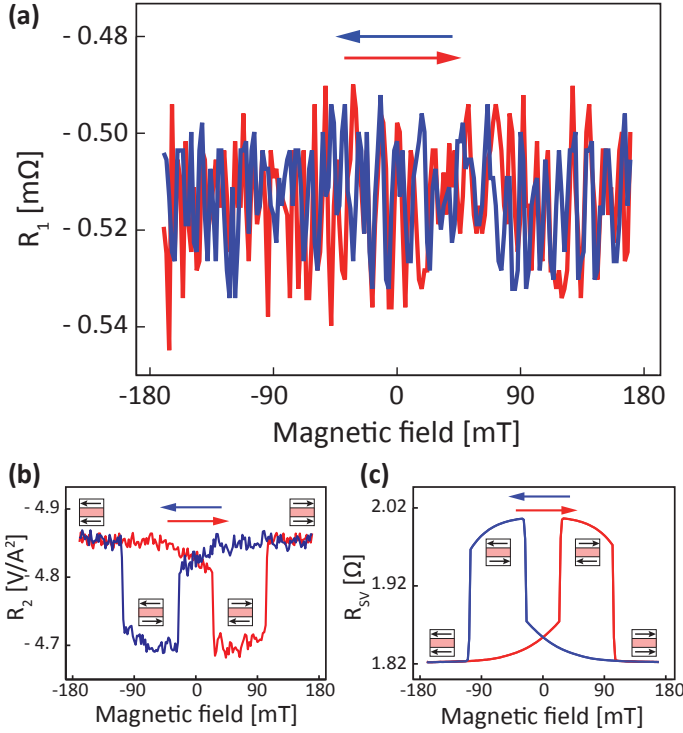


**Figure 4.8:** Measurements at 77K. (a) First-harmonic response signal,  $R_{3-4}^{(1f)} = V_{3-4}^{(1f)} / I$ , at 77K measured at the thermocouple with a root mean square current of 1 mA. (b) Second-harmonic response signal,  $R_{3-4}^{(2f)} = V_{3-4}^{(2f)} / I^2$ , at 77K measured at the thermocouple with a root mean square current of 1 mA. (c) Spin valve measurement at 77K on the same device.

As the Joule heating depends on the resistance, the increase of the materials' conductivities at 77K will give a lower second harmonic background signal, which is in accordance with the measurement shown in Fig. 4.8b. At the same time the second harmonic spin signal goes up because of the increased difference in resistance between P and AP alignment shown in the spin valve measurements. In the measurement this increase is smaller due to temperature dependences of the Seebeck coefficients and thermal conductivities.

In conclusion we can say that the disappearance of the first harmonic signal, while the spin valve signal increases, rules out the possibility of it originating from spin valve voltage pick up and is consistent with the spin-dependent Peltier effect. Furthermore the second harmonic and spin valve measurement behavior confirm

the lowering of the reference temperature and the correct operation of the device and thermocouple.

#### 4.5.6 Modeling parameters

The parameters that were used in the 3-D finite element modeling are summarized in Table 4.1.

**Table 4.1:** *Input parameters for the modeling.*

Material	$\sigma$ [ $\text{S m}^{-1}$ ]	$\Pi$ [mV]	$\lambda$ [nm]	$\kappa$ [ $\text{W m}^{-1} \text{K}^{-1}$ ]
Au	$2.2 \times 10^7$	0.51	80	300
Pt	$9.5 \times 10^6$	-1.5*	5	72
Cu	$4.3 \times 10^7$	0.48	350	300
Py	$4.3 \times 10^6$	-6.0*	5	30
NiCu	$2.0 \times 10^6$	-9.6*	5	20
SiO <sub>2</sub>	$1.0 \times 10^{-13}$	0	-	1
Al <sub>2</sub> O <sub>3</sub>	$1.0 \times 10^{-13}$	0	-	30

\* The Peltier coefficient was determined in a separate device specifically designed to accurately determine the Seebeck/Peltier coefficient of a material (discussed in Chapter 5).

## Bibliography

- [1] D. K. C. MacDonald, *Thermoelectricity, An introduction to the Principles*, Dover Publications, Inc., Mineola, New York, 2006.
- [2] I. Žutić, J. Fabian, and S. Das Sarma, "Spintronics: Fundamentals and applications," *Rev. Mod. Phys.* **76**, pp. 323–410, Apr 2004.
- [3] L. Gravier, S. Serrano-Guisan, F. Reuse, and J.-P. Ansermet, "Spin-dependent peltier effect of perpendicular currents in multilayered nanowires," *Phys. Rev. B* **73**, p. 052410, Feb 2006.
- [4] F. Giazotto, T. T. Heikkilä, A. Luukanen, A. M. Savin, and J. P. Pekola, "Opportunities for mesoscopics in thermometry and refrigeration: Physics and applications," *Rev. Mod. Phys.* **78**, pp. 217–274, Mar 2006.
- [5] G. E. W. Bauer, A. H. MacDonald, and S. Maekawa, "Spin caloritronics," *Solid State Communications* **150**(11-12), pp. 459 – 460, 2010.
- [6] K. Uchida, S. Takahashi, K. Harii, J. Ieda, W. Koshibae, K. Ando, S. Maekawa, and E. Saitoh, "Observation of the spin Seebeck effect," *Nature* **455**, pp. 778–81, Oct. 2008.
- [7] C. M. Jaworski, J. Yang, S. Mack, D. D. Awschalom, J. P. Heremans, and R. C. Myers, "Observation of the spin-Seebeck effect in a ferromagnetic semiconductor," *Nature Materials* **9**, pp. 1–6, Sept. 2010.
- [8] K. Uchida, J. Xiao, H. Adachi, J. Ohe, S. Takahashi, J. Ieda, T. Ota, Y. Kajiwara, H. Umezawa, H. Kawai, G. E. W. Bauer, S. Maekawa, and E. Saitoh, "Spin Seebeck insulator," *Nature Materials* **9**, pp. 1–4, Sept. 2010.
- [9] A. Slachter, F. L. Bakker, J.-P. Adam, and B. J. van Wees, "Thermally driven spin injection from a ferromagnet into a non-magnetic metal," *Nat Phys* **6**, pp. 879–882, 2010.
- [10] J.-C. Le Breton, S. Sharma, H. Saito, S. Yuasa, and R. Jansen, "Thermal spin current from a ferromagnet to silicon by seebeck spin tunnelling," *Nature* **475**, pp. 82–85, 2011.
- [11] M. Hatami, G. E. W. Bauer, Q. Zhang, and P. J. Kelly, "Thermal spin-transfer torque in magnetoelectronic devices," *Phys. Rev. Lett.* **99**, p. 066603, Aug 2007.
- [12] H. Yu, S. Granville, D. P. Yu, and J.-P. Ansermet, "Evidence for thermal spin-transfer torque," *Phys. Rev. Lett.* **104**, p. 146601, Apr 2010.
- [13] T. T. Heikkilä, M. Hatami, and G. E. W. Bauer, "Spin heat accumulation and its relaxation in spin valves," *Phys. Rev. B* **81**, p. 100408, Mar 2010.
- [14] M. Walter, J. Walowski, V. Zbarsky, M. Münzenberg, M. Schäfers, D. Ebke, G. Reiss, A. Thomas, P. Peretzki, M. Seibt, J. S. Moodera, M. Czerner, M. Bachmann, and C. Heiliger, "Seebeck effect in magnetic tunnel junctions," **10**, pp. 742–746, July 2011.
- [15] N. Liebing, S. Serrano-Guisan, K. Rott, G. Reiss, J. Langer, B. Ocker, and H. Schumacher, "Tunneling Magnetothermopower in Magnetic Tunnel Junction Nanopillars," *Physical Review Letters* **107**, p. 177201, Oct. 2011.

- 
- [16] M. Hatami, G. E. W. Bauer, Q. Zhang, and P. J. Kelly, "Thermoelectric effects in magnetic nanostructures," *Phys. Rev. B* **79**, p. 174426, May 2009.
- [17] A. Slachter, F. L. Bakker, and B. J. van Wees, "Modeling of thermal spin transport and spin-orbit effects in ferromagnetic/nonmagnetic mesoscopic devices," *Physical Review B* **84**, p. 174408, Nov. 2011.
- [18] M. D. Stiles and J. Miltat, *J. Spin Dynamics in confined Magnetic Structures III: Topics in Applied Physics*, vol. 101, Springer Berlin / Heidelberg, 2006.
- [19] F. L. Bakker, A. Slachter, J.-P. Adam, and B. J. van Wees, "Interplay of Peltier and Seebeck Effects in Nanoscale Nonlocal Spin Valves," *Physical Review Letters* **105**, p. 136601, 2010.
- [20] A. Slachter, F. L. Bakker, and B. J. van Wees, "Anomalous Nernst and anisotropic magnetoresistive heating in a lateral spin valve," *Physical Review B* **84**, p. 020412(R), July 2011.
- [21] A. Tulapurkar and Y. Suzuki, "Boltzmann approach to dissipation produced by a spin-polarized current," *Physical Review B* **83**, p. 012401, Jan. 2011.
- [22] S. Dubois, L. Piraux, J. M. George, K. Ounadjela, J. L. Duvail, and A. Fert, "Evidence for a short spin diffusion length in permalloy from the giant magnetoresistance of multilayered nanowires," *Phys. Rev. B* **60**, pp. 477–484, Jul 1999.
- [23] S. Steenwyk, S. Hsu, R. Loloee, J. Bass, and W. P. Jr., "Perpendicular-current exchange-biased spin-valve evidence for a short spin-diffusion length in permalloy," *Journal of Magnetism and Magnetic Materials* **170**(1-2), pp. L1 – L6, 1997.
- [24] T. Valet and A. Fert, "Theory of the perpendicular magnetoresistance in magnetic multilayers," *Physical Review B* **48**, p. 7099, 1993.



## Chapter 5

---

# Nanoscale temperature detection using the Seebeck effect

### Abstract

*We experimentally study the effect of Joule heating on the electron temperature in metallic nanoscale devices and compare the results with a diffusive 3D finite element model. The temperature is probed using four thermocouples located at different distances from the heater. A good quantitative agreement, within 30 %, between the experimental data and the modeling is obtained. Since we observe a strong thickness dependence of the electrical conductivity of our metals, we find that the Joule heating in nanoscale devices is often incorrectly calculated if bulk conductivities are used. Furthermore, Peltier heating/cooling is investigated and the combination with Seebeck temperature measurements provides us with a method to determine the Seebeck coefficient of a material.*

## 5.1 Introduction

Sensing and controlling heat flow in electronic devices becomes more important as the dimensions approach the nanoscale [1]. In contrast to charge transport, experimental studies of heat transport in mesoscopic structures are scarce [2, 3] though interesting new physics has been predicted. For example, electron-lattice relaxation processes can lead to a difference between phonon and electron temperatures at small length scales [4]. Moreover, the discovery of spin-dependent thermal effects [5, 6], e.g. the spin-Seebeck effect [7], thermal spin injection [8] and very recently the spin-dependent Peltier effect [9, 10], has stimulated the interest in small scale heat flow control. Local temperature control and detection are crucial in the experimental study of these effects.

In this paper, we study local Joule heating in nanoscale strips by probing the electron temperature with thermocouples consisting of junctions between two different metals. We model the devices with 3D finite element methods in Comsol Multiphysics [11] and focus on the influence of the device dimensions on the transport behavior. Furthermore, the role of the substrate and the effect of electron-phonon scattering on the heat transport are discussed. By comparison of the measurement

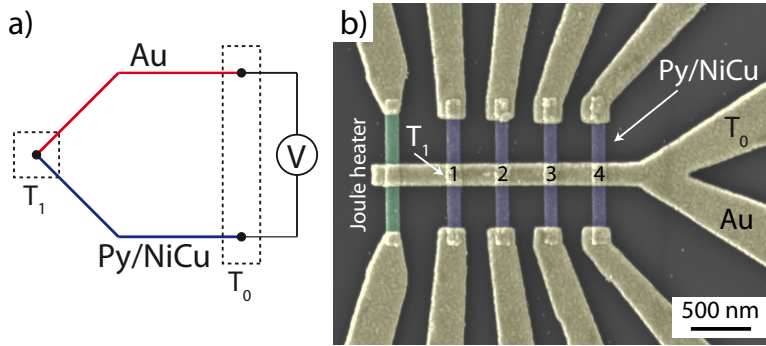


**Figure 5.1:** (a) Schematic representation of a temperature measurement using a thermocouple. In our devices, we measure the difference between the electron temperature at junction of the two materials ( $T_1$ ) and in the leads ( $T_0$ ) by making use of the Seebeck effect. (b) Scanning electron microscope (SEM) image of the device. The temperature is locally increased using Joule heating in a narrow constriction (green). Consequently, a thermal gradient is generated across the Au strip and across the NiCu/Py strips. Via the Seebeck effect, this allows for an electron temperature measurement at each of the four interfaces (1-4).

results with the model calculations, we aim for a better fundamental understanding of heat transport in nanoscale systems.

In quasi-equilibrium, when the device dimensions are much larger than the electron-electron relaxation length, the electron energy distribution is well defined. This distribution obeys Fermi-Dirac statistics and the system can be described in terms of a temperature  $T$  and a potential  $V$ . The conductivity is then energy dependent, which leads to a gradient in the potential whenever a temperature gradient is present. This relation,  $\nabla V = -S\nabla T$ , is called the Seebeck effect and for simple metals  $S$  is given by the Mott relation [12]:

$$S = \frac{\pi^2}{3} \left( \frac{k_B^2 T}{e} \right) \left( \frac{\partial \ln(\sigma(E))}{\partial E} \right)_{E=E_F} \quad (5.1)$$

where  $\sigma$  is the electrical conductivity and  $E$  the electron energy. Since the Seebeck effect is a property of the electron system it can be exploited for a temperature measurement of the electrons, for instance by using a thermocouple (depicted in Fig. 5.1a). The Seebeck coefficient  $S$  is strongly material dependent and has, for metals like Cu and Au, a rather small value ( $\approx 2 \mu\text{V}/\text{K}$ ). However, for Ni alloys the effect is enhanced due to the specific band structure (up to  $-40 \mu\text{V}/\text{K}$  for NiCu).



## 5.2 Experimental Techniques

The samples are fabricated using a two-step electron beam lithography process on top of a thermally oxidized Si substrate with a SiO<sub>2</sub> layer thickness of 300 nm. A scanning electron microscopy (SEM) image of the device is shown in Fig. 5.1b. The device consists of four 40 nm thick Ni<sub>45</sub>Cu<sub>55</sub> (Constantan) or Py (Ni<sub>80</sub>Fe<sub>20</sub>) strips that form a thermocouple with a 120 nm thick top contact of Au. For the deposition of the NiCu, we use a double-layer resist technique with a large undercut area (PMMA-MA and PMMA 950K) in combination with sputtering to preserve the right alloy composition. The Au and Py are deposited using an e-beam evaporator with a base pressure of  $1 \times 10^{-7}$  mbar. Prior to the deposition of Au, the NiCu or Py surface is cleaned with Ar ion milling to ensure transparent interfaces.

We have studied four types of devices where we varied the heater material and its dimensions and the thermocouple materials. A heater consists of a metallic constriction that is electrically heated via Joule heating. It is connected by a metal strip to the four junction areas where we have measured the electron temperature. For the heating, an ac current with a low frequency (20 Hz) is used which allows us to treat the heat transport as stationary for our device dimensions. The thermo voltages are measured using a lock-in measurement technique in order to separate linear ( $\Delta T \propto I$ ) and quadratic ( $\Delta T \propto I^2$ ) contributions, by taking the first harmonic  $V_1$  and second harmonic  $V_2$  response, respectively. In this way, we can separate the effects due to Joule heating (quadratic with the current) from other (linear) effects as, for instance, the Peltier [13] or Nernst [11] effect. All measurements are performed at room temperature.

## 5.3 Model

The stationary heat transport is modeled based on Fourier's law as described in earlier work [11, 13]. In the model, both the charge current  $\vec{J}$  and the heat current  $\vec{Q}$  are coupled to the electrochemical potential  $eV$  and temperature  $T$  by the electrical conductivity  $\sigma$ , the thermal conductivity  $\kappa$ ,  $\Pi$  and  $S$ , via:

$$\begin{pmatrix} \vec{J} \\ \vec{Q} \end{pmatrix} = - \begin{pmatrix} \sigma & \sigma S \\ \sigma \Pi & \kappa \end{pmatrix} \begin{pmatrix} \vec{\nabla} V \\ \vec{\nabla} T \end{pmatrix} \quad (5.2)$$

The off-diagonal terms represent the Seebeck and Peltier effect, where  $\Pi = ST_0$ . Here,  $T_0$  is the reference temperature of the device and taken to be 300K. At the end of all the leads and at the bottom of the substrate we set the temperature at  $T_0$ . Joule heating is incorporated using  $\vec{\nabla} \cdot \vec{Q} = J^2/\sigma$  and charge conservation is put in by

**Table 5.1:** Modeling parameters. Electrical conductivities  $\sigma$  are measured in a separate device, whereas the thermal conductivities  $\kappa$  are derived from  $\sigma$  and the literature values  $\kappa_l$  and  $\sigma_l$  using the Wiedemann-Franz law as  $\kappa = \frac{\sigma}{\sigma_l} \kappa_l$ . The Seebeck coefficients  $S$  of Au and Pt are taken from literature, whereas the coefficients of Py and NiCu are determined by comparing the experimental results with the model. The thermal conductivity for SiO<sub>2</sub> is obtained from phonon conduction [15].

Mat.	t [nm]	$\sigma$ [S/m]	$\kappa$ [W/(mK)]	$S$ [ $\mu$ V/K]
Au	40	$1.8 \times 10^7$	120	1.7
Au	120	$2.7 \times 10^7$	180	1.7
Pt	40	$4.2 \times 10^6$	32	-5
Py	40	$2.9 \times 10^6$	20	-18
NiCu	40	$1.0 \times 10^6$	10	-30
SiO <sub>2</sub>	300	$1.0 \times 10^{-13}$	1.3	0

the constraint  $\vec{\nabla} \cdot \vec{J} = 0$ . As input for the model we use for the metals the electrical conductivities that are experimentally determined in a dedicated device whereas the thermal conductivities are derived from the Wiedemann-Franz law. The Seebeck coefficients of Au and Pt are taken from literature [14], while the Seebeck coefficients of Py and NiCu are the only free parameters in the model. Heat conduction through the substrate is taken into account for a total substrate thickness of 300 nm. All model input parameters are summarized in Table 5.1.

In our nanoscale devices, both phonons and electrons participate in the heat transport. For metals, the thermal conductance  $\kappa$  can be then seen as the sum of the contribution of the electron ( $\kappa_e$ ) and phonon ( $\kappa_p$ ) system if we assume that the electrons and phonons are at the same temperature, i.e. the electron-phonon coupling is strong. On the other hand, if the electron-phonon coupling is weak, the electron and phonon system temperature cannot equilibrate fast enough and hence, at very short length scales we can neglect the phonon contribution completely. In fact, since thermal transport in metals is dominated by electrons ( $\kappa_e \gg \kappa_p$ ) and since we are heating and detecting only the electron system, we argue that a description based on solely the electron system ( $\kappa = \kappa_e$ ) is sufficient in purely metallic systems.

For the SiO<sub>2</sub> substrate, the situation is different since the heat conduction in insulators is fully determined by the phonons ( $\kappa = \kappa_p$ ). When heat transfer across metal-insulator interfaces is taken into account, electron-phonon coupling is essential because heat needs to be transferred from the electrons (metal) to the phonons (insulator). For electron-phonon relaxation lengths comparable to the device di-

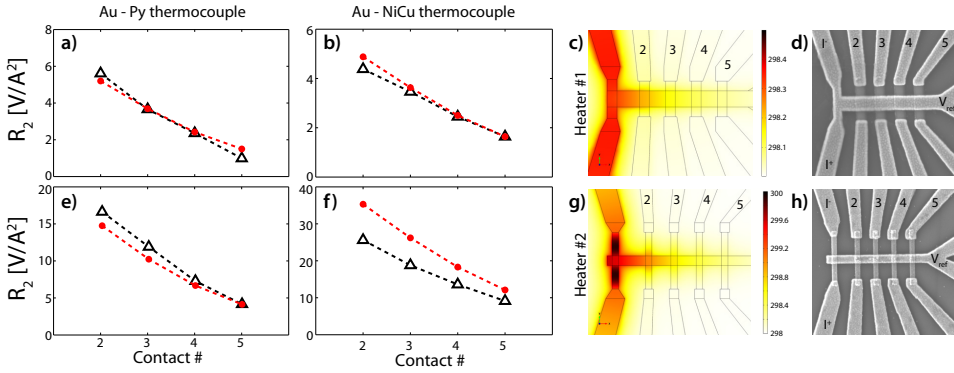


**Figure 5.2:** (a) Seebeck voltage (triangles) at the different Py - Au thermocouples for a 120 nm thick Au heater. (b) For a similar Joule heater as in (a), but now with NiCu - Au thermocouples. (c) Modeling results for the device, where the obtained voltages are depicted in (a) and (b) (red dots). (d) SEM image of the device. (e) Py - Au thermocouple in combination with a 40 nm thick Au heater strip. (f) NiCu - Au thermocouple with a heater consisting of 40 nm thick Pt strip. (g) Temperature distribution obtained from thermoelectric modeling. (h) SEM image of the device.

mensions, the modeling needs in principle to be extended with electron-phonon interactions [16, 17]. However, since the electron-phonon interaction length is expected to be in the order of tens of nanometers in metals at room temperature, we have assumed that phonons and electrons have equal temperatures everywhere.

## 5.4 Results and Discussion

The main results of the electron temperature measurements are shown in Fig. 5.2 where we have used a Joule heating rms current of 1 mA. In the first row of the figure, the results for heater type 1 are shown. Heater type 1 consists of a 120 nm thick Au strip as displayed in Fig. 5.2d. The data obtained for heater type 2 are plotted in the second row of Fig. 5.2. This heater consists of a narrow strip with a thickness of 40 nm such that the heat is generated more locally (Fig. 5.2g). For both heaters we have measured the second harmonic response voltage  $V_2$  which divided by  $I^2$  gives us the second harmonic resistance  $R_2$ . These Seebeck voltages are measured at four contacts with respect to a reference voltage  $V_{ref}$  for two different thermocouples, namely Py/Au (triangles in Fig. 5.2a and e) and NiCu/Au (triangles in Fig. 5.2b and f). The corresponding temperature distributions obtained from the modeling are shown in Fig. 5.2c and Fig. 5.2g where we have observed that the

maximum temperature for the thin heater is higher than for the thick heater. The dots in Fig. 5.2a, b, e and f refer to the Seebeck voltages ( $V - V_{\text{ref}}$ ) that are calculated with the model.

The experimental observations are in good quantitative agreement with the calculations. We have slightly adjusted ( $< 25\%$  with respect to the literature values) the Seebeck coefficient of NiCu and Py to obtain a better agreement with the data (Table 5.1). Since Joule heating scales inversely proportional with the conductivity of the material ( $\vec{\nabla} \cdot \vec{Q} = J^2/\sigma$ ), a correct value for the electrical conductivity is essential. Therefore, we have separately measured the conductivity for different materials and thicknesses. The results of these measurements are shown in Table 5.1, where we have observed a thickness dependence for the electrical conductivity in Au. When this is taken into account, we find that our model is able to predict the Seebeck voltages fairly well. We note that the heat loss through the substrate plays a major role in these Joule heated devices. Calculations without substrate lead to a mismatch up to one order of magnitude between experiment and theory. Furthermore, we have excluded magnetic effects by performing magnetic field dependent measurements and did not find any dependence on magnetic field.

Fig. 5.3 shows a similar measurement where the heat source is changed from Joule heating to Peltier heating at one of the thermocouple interfaces. In the experiment, current is sent from contact  $I^+$  to  $I^-$  and the first harmonic response voltage is measured at contacts 3, 4 and 5. Here, Joule heating is irrelevant, because that can only be observed in the second harmonic voltage response. The resistances ( $R_1 = V_1/I$ ) are shown in Fig. 5.3b for a Py/Au thermocouple and in Fig. 5.3c for a NiCu/Au thermocouple. Again, we find a good agreement between the observations and the modeling, which confirms the validity of the diffusion model. Moreover, the observations are also in agreement with earlier measurements obtained in Py/Cu spin valves [13].

The comparison between experiments and modeling of Joule heating presented in Fig. 5.2 emphasizes the importance of electrical conductivity measurements for all materials in the current path. For Peltier heating, which does not depend on the electrical conductivity, this requirement is not present and the modeling is often in better agreement with the data. For example, in Ref. 8 and Ref. 13 the observed Seebeck voltages generated by the Joule heating were up to three times higher than expected from modeling, whereas the Peltier heating could be modeled very well. We expect that the actual electrical conductivity of the materials in the current path was probably smaller and led to the mismatch between the model and experimental signals. The lower conductivities (compared to bulk) that are frequently observed in nanoscale devices and thin film multilayer structures are difficult to estimate and therefore require additional measurements [18, 19]. Furthermore, the large surface

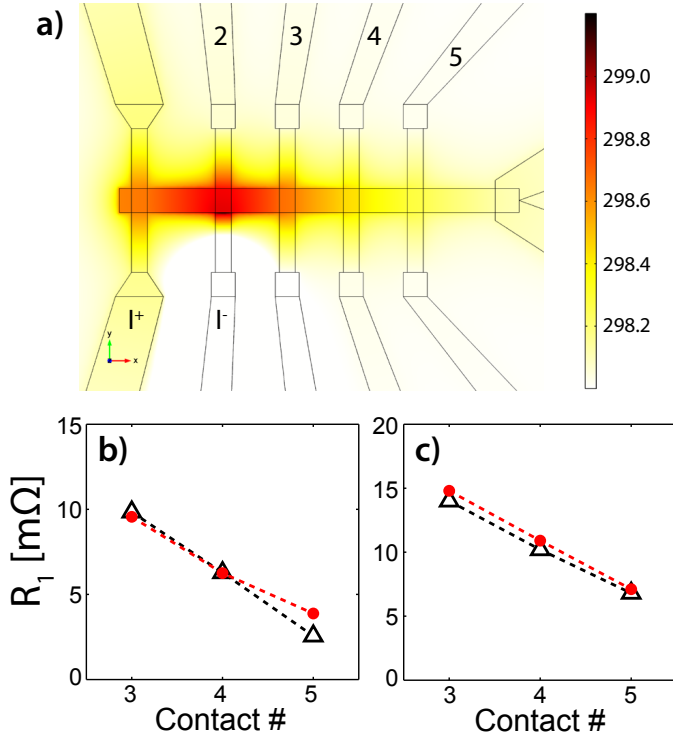


**Figure 5.3:** Measurement of the Peltier heating and subsequent Seebeck voltage pick-up, where we exclude the effect of Joule heating by measuring solely the linear response voltage. (a) Modeling of the heating due to the Peltier effect for a current of 1 mA. In the temperature distribution shown, the effect of Joule heating is disregarded for clarity. (b) Results for the same device as discussed in Fig. 5.2a. (c) Results for the same device as discussed in Fig. 5.2b.

to volume ratio of our nanosized contacts can lead to extra heat loss by thermal radiation to the environment as reported by Léonard [20]. We did not observe this phenomenon, which can be explained by the fact that our device dimensions are still large compared to the nanowires considered in their article.

The thermoelectric model in principle allows for temperature dependent parameters. However, in practice little is known about their temperature dependence which makes our model not directly applicable to temperatures other than room temperature. Moreover, the initial assumption that the electron-phonon interaction length is much smaller than the device dimensions is not necessarily valid at lower temperatures [4]. Small overall temperature variations, on the other hand, will not

significantly alter the obtained results, since they can be assumed to be constant over the very short length scales measured here. Based on the minimum Seebeck voltage that is detectable (i.e. exceeds the noise level), we estimate that the highest sensitivity that can be obtained with these type of devices is a temperature difference of approximately 1 mK.

The agreement between our model and the experiment suggests that the initial assumption that electrons and phonons are at the same temperature everywhere is valid for the device dimensions discussed here. Additional experimental work is needed to study the heat transport across thin barriers of insulating material, as in for example tunnel barriers. In order to obtain accurate results, the modeling needs then to be extended with extra interface thermal conductances [21].

## 5.5 Conclusion

In summary, we have presented an accurate measurement of the electron temperature in metallic nanoscale devices and compared it to finite-element modeling using Fourier's law based on diffusive transport. We found that the model was in good agreement with the experiments when the electrical conductivities of the materials are all well known. We allowed for small adjustments of the Seebeck coefficient from literature values for Py and NiCu to improve the agreement with the experiments. Furthermore, heat conduction through the substrate can be modeled accurately by assuming that the electron and phonon coupling is strong. We hope that this research stimulates further experimental investigation of nanoscale heat transport and in particular, at smaller length- and timescales and by including non-metallic elements.

## Bibliography

- [1] D. G. Cahill, W. K. Ford, K. E. Goodson, G. D. Mahan, A. Majumdar, H. J. Maris, R. Merlin, and S. R. Phillpot, "Nanoscale thermal transport," *Journal of Applied Physics* **93**(2), p. 793, 2003.
- [2] A. D. Avery, R. Sultan, D. Bassett, D. Wei, and B. L. Zink, "Thermopower and resistivity in ferromagnetic thin films near room temperature," *Physical Review B* **83**, p. 100401, Mar. 2011.
- [3] W. Sun, H. Liu, W. Gong, L.-M. Peng, and S.-Y. Xu, "Unexpected size effect in the thermopower of thin-film stripes," *Journal of Applied Physics* **110**(8), p. 083709, 2011.
- [4] F. Giazotto, T. Heikkilä, A. Luukanen, A. Savin, and J. Pekola, "Opportunities for mesoscopies in thermometry and refrigeration: Physics and applications," *Reviews of Modern Physics* **78**, pp. 217–274, Mar. 2006.
- [5] G. E. Bauer, A. H. MacDonald, and S. Maekawa, "Spin Caloritronics," *Solid State Communications* **150**, pp. 459–460, Mar. 2010.
- [6] M. Hatami, G. Bauer, Q. Zhang, and P. Kelly, "Thermoelectric effects in magnetic nanostructures," *Physical Review B* **79**, p. 174426, May 2009.
- [7] K. Uchida, S. Takahashi, K. Harii, J. Ieda, W. Koshibae, K. Ando, S. Maekawa, and E. Saitoh, "Observation of the spin Seebeck effect.," *Nature* **455**, pp. 778–81, Oct. 2008.
- [8] A. Slachter, F. L. Bakker, J.-P. Adam, and B. J. van Wees, "Thermally driven spin injection from a ferromagnet into a non-magnetic metal," *Nature Physics* **6**, pp. 879–882, Sept. 2010.
- [9] J. Flipse, F. L. Bakker, A. Slachter, F. K. Dejene, and B. J. van Wees, "Cooling and heating with electron spins: Observation of the spin Peltier effect," *arXiv:1109.6898v1 [cond-mat.mes-hall]*, 2011.
- [10] L. Gravier, S. Serrano-Guisan, F. Reuse, and J.-P. Ansermet, "Spin-dependent peltier effect of perpendicular currents in multilayered nanowires," *Phys. Rev. B* **73**, p. 052410, Feb 2006.
- [11] A. Slachter, F. L. Bakker, and B. J. van Wees, "Modeling of thermal spin transport and spin-orbit effects in ferromagnetic/nonmagnetic mesoscopic devices," *Phys. Rev. B* **84**, p. 174408, Nov 2011.
- [12] N. F. Mott and H. Jones, *The Theory of the Properties of Metals and Alloys*, Oxford Univ. Press, London, 1936.
- [13] F. L. Bakker, A. Slachter, J.-P. Adam, and B. J. van Wees, "Interplay of Peltier and Seebeck Effects in Nanoscale Nonlocal Spin Valves," *Physical Review Letters* **105**, p. 136601, Sept. 2010.
- [14] C. Kittel, *Introduction to Solid State Physics -7th ed.*, John Wiley & Sons, Inc., New York, 1995.
- [15] T. Yamane, N. Nagai, S.-i. Katayama, and M. Todoki, "Measurement of thermal conductivity of silicon dioxide thin films using a  $3\omega$  method," *Journal of Applied Physics* **91**(12), p. 9772, 2002.

- [16] J. Lai and A. Majumdar, "Concurrent thermal and electrical modeling of sub-micrometer silicon devices," *Journal of Applied Physics* **79**(9), pp. 7353–7361, 1996.
- [17] G. Chen, "Ballistic-diffusive heat-conduction equations," *Phys. Rev. Lett.* **86**, pp. 2297–2300, Mar 2001.
- [18] K. Fuchs, "The conductivity of thin metallic films according to the electron theory of metals," *Mathematical Proceedings of the Cambridge Philosophical Society* **34**(01), pp. 100–108, 1938.
- [19] W. Steinhögl, G. Schindler, G. Steinlesberger, and M. Engelhardt, "Size-dependent resistivity of metallic wires in the mesoscopic range," *Phys. Rev. B* **66**, p. 075414, Aug 2002.
- [20] F. Léonard, "Reduced joule heating in nanowires," *Applied Physics Letters* **98**(10), p. 103101, 2011.
- [21] E. T. Swartz and R. O. Pohl, "Thermal resistance at interfaces," *Applied Physics Letters* **51**(26), pp. 2200–2202, 1987.



# Magnetization dynamics

### Abstract

*In this chapter, an introduction into the fundamental theory of magnetization dynamics is given based on the macrospin approach. First, the most important mechanisms originating from the dynamical behaviour of the magnetization are discussed such as the spin-transfer torque and spin pumping. The main part of this chapter focuses on the magnetization dynamics during ferromagnetic resonance (FMR). Based on the different energies of importance in magnetic systems such as Zeeman, demagnetizing, exchange and anisotropy energies, an analytical expression in terms of susceptibilities is derived for the dissipation during FMR. Furthermore, different techniques to measure FMR are discussed and numerical simulations using OOMMF are included where the dissipation during resonance is explicitly calculated and compared with the analytical results. The chapter concludes with a short summary and outlook.*

## 6.1 Introduction

The study of magnetization dynamics in ferromagnetic materials is vital for the development of future spintronic applications. Merging the time-dependent precessional motion of the spin with the stationary spin transport mechanisms [1], described in Chapter 2, offers various new possibilities for data storage and processing. One of the most promising mechanisms is the spin-transfer torque (STT) effect [2], originally proposed by Slonczewski [3] and Berger [4]. Here, the angular momentum associated with the electrons in a spin current is transferred to the magnetization of a ferromagnetic element, provided that the magnetization and the polarization of the spin current are non-collinear [5]. The resulting torque on the magnetization leads to excitation or eventually switching of the ferromagnetic layer. This effect is mainly studied in spin valve devices, consisting of two ferromagnetic layers (F) separated by a nonmagnetic layer N ( $F_1/N/F_2$ ). When a charge current is sent through such a device, angular momentum will be transported from  $F_1$  to  $F_2$  and vice versa. Suppose that the magnetization of the first ferromagnetic layer is fixed and  $F_2$  is a soft ferromagnet. Then, the orientation of  $F_2$  can be switched

between parallel and anti-parallel (with respect to  $F_1$ ) depending on the direction of the applied current (and thus its associated spin current) [6, 7]. In addition to the work on metallic multilayers, where high currents are required and low magnetoresistances are obtained, magnetic tunnel junctions (MTJ's) are promising candidates for the development of fast and small non-volatile memory elements [8]. Moreover, in Chapter 2 it has been shown that besides a voltage gradient, a thermal gradient across a F/N junction induces a spin current. Magnetization reversal driven by a temperature gradient, the so-called thermal torque, is an innovative technique to make use of the waste heat in integrated circuits and memory cells [9, 10].

Magnetization dynamics is also studied in nonlocal spin valves, where the effect of pure spin currents can be investigated without spurious effects caused by the charge current. Yang *et al.* have demonstrated spin-torque switching induced by a pure spin current in a nonlocal spin valve device [11] at low temperatures. Similar results have been obtained in a three-terminal geometry using magnetic tunnel junctions [12]. Furthermore, it has been shown that spin currents are affected by magnetic fields due to their precessional motion. Electrically injected spins that diffuse through a material do precess in the presence of a magnetic field and can be oriented anti-parallel to their initial direction when they arrive at the detector. This effect has been shown experimentally by Jedema *et al.* [13] in an Aluminum strip where the detected collinear spin accumulation depends on the precession frequency (i.e. magnetic field strength). Such a Hanle precession measurement is nowadays a well established method to study spin transport phenomena in novel materials as for instance graphene [14].

Using the spin-transfer torque effect one can induce a stable precessional motion of the magnetization of a ferromagnet [15]. These gigahertz resonance phenomena observed in nanopillars may be applicable for tunable microwave sources in the near future [16, 17, 18, 19, 20]. Alternatively, control of resonance of ferromagnetic layers can be achieved by STT. Using the spin Hall effect, spin currents can be injected in the ferromagnetic layer and change the effective damping parameter, leading to amplification or suppression of the magnetization dynamics [21, 22].

Since spin currents can induce magnetization motion, one can expect that an inverse effect is also present. Indeed, it turns out that a precessing magnetization emits a spin current into an adjacent conductive medium, a phenomenon which is called spin pumping. The first experimental observations of this effect go back to 1979, when a coupling between the ferromagnetic and conduction spin-resonance modes was found at a F/N interface [23]. Theoretically, the spin-pumping process has been fully described by Tserkovnyak *et al.* [24, 25, 26] and it leads to an enhanced Gilbert damping in the ferromagnetic material. At every instant of time, the spins that are emitted into N are oriented transverse to the magnetization (parallel to the

damping term). Depending on the relaxation rate of N this either enhances the Gilbert damping (large relaxation rate) or induces a spin accumulation in N (small relaxation rate). The latter enables the fabrication of a spin source or, spin battery driven by magnetization dynamics [27].

In the first experimental observations, the spin pumping effect has been shown indirectly by the effect of adjacent layers on the Gilbert damping parameter in metallic ferromagnets [28, 29] and later in ferromagnetic insulators as Yttrium Iron Garnet (YIG) [30]. Recent experimental work has demonstrated the possibility of spin injection across semiconductor/ferromagnetic metal or ferromagnetic insulator/metal interfaces using the spin pumping mechanism [31, 32, 33]. Here, the spin current is detected via the inverse spin Hall effect, where a spin current induces a transverse voltage in the detector due to the spin-orbit coupling. Interesting applications of the spin pumping effect can be found in the transmission of electrical signals using spin waves as reported by Kajiwara *et al.* [34].

In the remainder of this chapter, the focus lies on the magnetization dynamics during ferromagnetic resonance (FMR). An analytical expression for the dissipation during FMR is derived and different techniques to measure FMR are discussed. Additionally, the fundamental theory of magnetic energy and magnetization dynamics is covered in order to provide a solid base for understanding the experimental results of Chapter 7. This chapter concludes with numerical simulations of FMR using the micromagnetics software package OOMMF.

## 6.2 Magnetic energy

The magnetic energy associated with a magnetic moment  $\vec{m}$  in the presence of a magnetic field can be divided in multiple magnetostatic contributions. The most important contribution is the self-energy which describes the interaction of a magnetic moment with an external field or with a field it creates by itself. The interaction with the external field is described by the Zeeman energy and is given by:

$$E = -\mu_0 \int_V \vec{M} \cdot \vec{H}_{\text{ext}} dV \quad (6.1)$$

with  $\vec{H}_{\text{ext}}$  the externally applied magnetic field and  $\mu_0$  the permeability of free space.  $\vec{M}$  is the magnetization, which can be normalized by dividing it by the saturation magnetization as  $\vec{m} = \vec{M}/M_s$ . The field that any finite size ferromagnetic element generates in order to reduce its total magnetic moment is called its demagnetizing field  $H_D$ , or stray field, and arises because magnetic field lines form closed loops (i.e.  $\nabla \cdot B = 0$ ). The demagnetizing field gives rise to shape anisotropy and  $\vec{H}_D$  is related to the magnetization  $\vec{M}$  by a demagnetization tensor according to  $\vec{H}_D =$

$-N\vec{M}$ . For an arbitrary shaped object, the tensor  $N$  is often difficult to calculate, however, for simple shapes as for example ellipsoids the demagnetization factors can be derived analytically [35]. In a thin film, the in-plane factors are assumed to be zero and since  $N_x + N_y + N_z = 1$ , the perpendicular to plane factor is 1. Because the demagnetizing field can become comparable to the saturation magnetization  $M_s$ , in metallic ferromagnets such as Co or NiFe the demagnetizing fields can achieve considerably large values of around 1 T. The associated demagnetizing energy of a ferromagnetic element of volume  $V$  is:

$$E = -\frac{1}{2}\mu_0 \int_V \vec{M} \cdot \vec{H}_D dV \quad (6.2)$$

where the factor  $\frac{1}{2}$  is included to avoid double counting in the integral since every element contributes both as a source term and a magnetic moment.

The exchange interaction between magnetic moments leads to an exchange energy which tends to align neighbouring electron spin states to reduce the total energy of ferromagnetic materials. For the macrospin approach or in the absence of gradients in the magnetization, the exchange energy can be regarded as constant and has no influence on the magnetization motion and dissipation. Furthermore, there exists a crystallographic anisotropy energy in many materials that have a preferred crystallographic axis of magnetization, the so-called easy axes which are independent of the shape. In the ferromagnetic metals discussed in this thesis, this energy is not relevant since these materials are not crystalline.

For the simple case of an uniform magnetization in the presence of a static magnetic field, the magnetostatic self energy of the system can be represented by the Stoner-Wohlfarth picture [36]. Consider a ferromagnet with an uniaxial anisotropy where the demagnetizing field is now governed by the anisotropy constant  $K_{1u}$ . The total energy is now given by the sum of Eq. 6.1 and Eq. 6.2:

$$E = K_{1u}V \sin^2(\phi) - \mu_0 M_s H V \cos(\phi - \phi_0) \quad (6.3)$$

with  $\phi$  and  $\phi_0$  the angles of the magnetization orientation and field orientation with respect to the uniaxial axis, respectively. The second term expresses the Zeeman energy of the system. The phenomenological constant  $K_{1u}$  depends on the shape of the ferromagnet (i.e. demagnetization factors), the saturation magnetization, strain and temperature. Under the influence of an increasing magnetic field opposite to the magnetization direction, Eq. 6.3 describes the orientation of the magnetization with respect to its uniaxial axis. The system gradually follows the local minimum in energy till eventually, its magnetization is reversed.

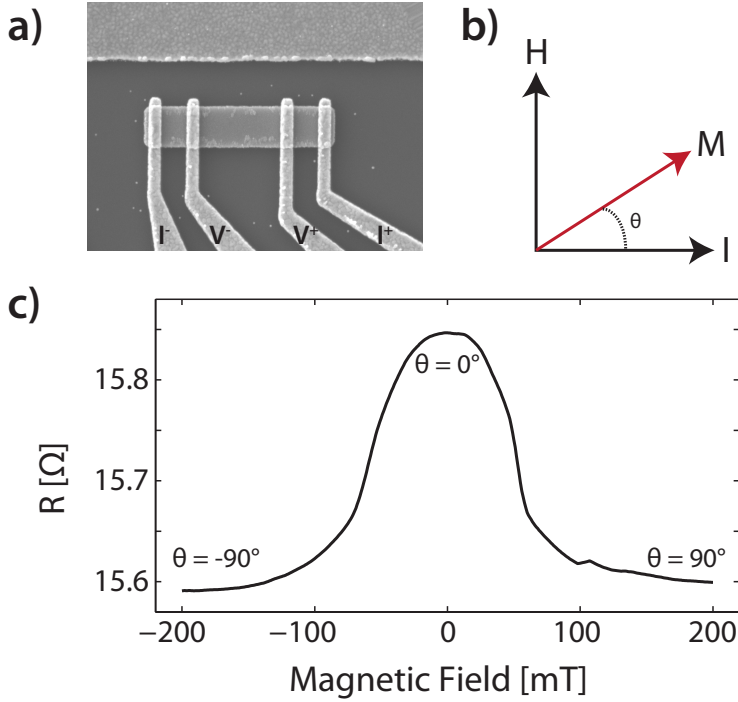


**Figure 6.1:** (a) Ferromagnetic (Py) strip contacted by four Au leads. The resistance of the strip is measured by sending a current through the outer two contacts while measuring the voltage between the inner contacts. (b) The anisotropic magnetoresistance (AMR) effect describes how the resistance changes depending on the angle  $\theta$  between the direction of the current  $\vec{I}$  and the magnetization  $\vec{M}$ . An external magnetic field  $\vec{H}$  is applied to rotate the magnetization with respect to the direction of the current. (c) Measurement of the AMR effect in a Py strip. The resistance changes approximately 1% between the parallel and perpendicular alignment of the current and the magnetization.

### 6.3 Anisotropic magnetoresistance

In order to study the rotation of the magnetization of a ferromagnetic element experimentally, one can make use of the anisotropic magnetoresistance (AMR) effect. This effect describes the change in resistance when the angle  $\theta$  between the current direction and the magnetization varies. The relation between resistance of a ferromagnet strip and  $\theta$  is given by:

$$R(\theta) = R_{||} - \Delta R \sin^2 \theta \quad (6.4)$$

with  $R_{\parallel}$  the resistance of the strip if the magnetization is aligned parallel to the current direction and  $\Delta R$  the difference between the parallel and perpendicular configuration of the magnetization and the current direction. Figure 6.1 shows an example of an AMR measurement in a Permalloy ( $\text{Ni}_{80}\text{Fe}_{20}$ ) microstrip contacted by four Au leads. The current is sent through the outer contacts while the voltage is measured between the inner contacts (Fig. 6.1b). In this so-called four terminal geometry, the resistance of the Py can be measured exclusively. An external magnetic field is applied perpendicular to the direction of the current, such that the magnetization rotates from the parallel to the perpendicular configuration as the field increases (Fig. 6.1b). A resistance difference of approximately  $0.2 \Omega$  is observed between both configurations, which is in the order of 1% of the total resistance. The AMR effect can be used to detect the angle of precession during ferromagnetic resonance as shown by Costache *et al.* [37] and in Section 6.4.2 this will be discussed in more detail. Since the dissipation of the current is proportional to  $I^2 R$ , the anisotropic magnetoresistance can also be detected thermally as demonstrated by Slachter *et al.* [38].

## 6.4 Magnetization dynamics

In the limit of slowly varying magnetic fields, the magnetization can be described in terms of the free energy as discussed in the Section 6.2. However, for short magnetic field pulses or fast varying magnetic fields one needs to describe the system's magnetization dynamics differently. For a macroscopic magnetic moment  $\vec{M}$ , or macrospin, subject to a fast changing magnetic field, the magnetization dynamics can be described by the Landau-Lifshitz-Gilbert-Slonczewski (LLGS) equation:

$$\frac{d\vec{M}}{dt} = -\gamma \left( \vec{M} \times \vec{H} \right) + \frac{\alpha}{M_s} \left( \vec{M} \times \frac{d\vec{M}}{dt} \right) - \frac{\gamma \hbar}{2eVM_s^2} \vec{M} \times \left( \vec{I}_s \times \vec{M} \right) \quad (6.5)$$

with  $\gamma = \mu_0 \frac{g|e|}{2m_e}$  the gyromagnetic ratio,  $\alpha$  a phenomenological damping term and  $M_s$  the saturation magnetization. The first term of Eq. 6.5 describes the Larmor precessional motion of the magnetic moment around the effective field, whereas the second term describes the damping towards this field. The effective field  $\vec{H}$  has various sources such as the external field, anisotropy, exchange and demagnetizing fields. The last term of Eq. 6.5 is called the Slonczewski term and determines the effect of spin transfer torque on the magnetization dynamics [3]. This torque on the magnetization depends on the magnitude and polarization direction of the spin current  $I_s$  that is injected and is inversely proportional to the volume  $V$  of the ferromagnet. Figure 6.2a gives a schematic representation of the three different terms

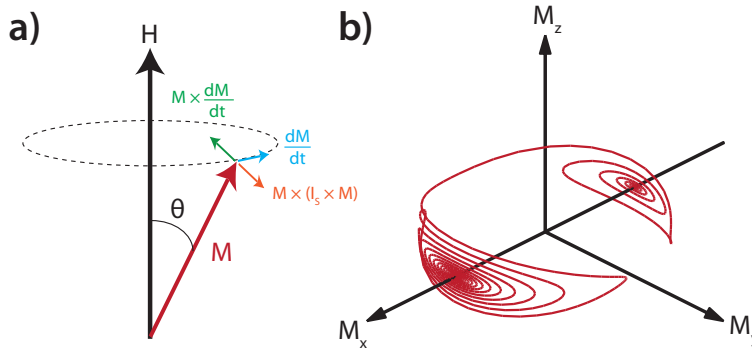


**Figure 6.2:** (a) Larmor precession described by the Landau-Lifshitz-Gilbert-Slonczewski (LLGS) equation. The magnetization precesses around the magnetic field  $\vec{H}$  in the direction of  $\frac{d\vec{M}}{dt}$  (blue). The damping towards the direction of the field is described by the cross product  $\vec{M} \times \frac{d\vec{M}}{dt}$  (green). In the case of spin injection, the spin-transfer torque will result in an extra torque in the direction opposite to the damping. (b) Numerical simulation of the magnetization dynamics in a system ( $150 \times 40 \times 5$  nm) with the initial magnetization ( $M_s = 1T$ ) pointing in the positive  $\hat{x}$  direction. At  $t = 0$ , a spin current of 1 mA (polarized in the  $-\hat{x}$  direction) is injected which induces a precessional motion of the magnetization. If the spin current is sufficient, the spin-torque term can overcome the damping and the system behaves as undamped. When the magnetization has rotated more than  $90^\circ$  ( $\theta > 90^\circ$ ), the magnetization motion is strongly damped towards the negative x-axis.

in the LLGS equation. The magnetization  $\vec{M}$  (red) precesses around the field  $\vec{H}$  (black) in the direction indicated by the blue arrow. The damping towards the field,  $\vec{M} \times \frac{d\vec{M}}{dt}$ , is shown in green, whereas the spin torque term  $\vec{M} \times (I_s \times \vec{M})$  (orange) is pointing in the opposite direction. The speed of the damping is determined by the phenomenological damping factor  $\alpha$  and has a value of approximately 0.01 for Py [37, 39].

The effect of the spin transfer torque can be visually demonstrated using numerical simulations. In Fig. 6.2b, the LLGS-equation is solved numerically for an ellipsoidal system ( $150 \times 40 \times 5$  nm) with an easy axis along  $\hat{x}$  direction and an initial magnetization pointing in the  $\hat{x}$  direction. The demagnetizing fields are the only fields that are taken into account and there is no external field applied. At  $t = 0$ , a spin current of 1 mA polarized in the negative  $\hat{x}$  direction is injected. The red line in Fig. 6.2b represents the magnetization motion starting from the positive x-axis, precessing around the effective magnetic field and slowly damping towards the negative x-axis. For  $\theta < 90^\circ$ , the spin torque term cancels the damping and the

system behaves as if it is undamped. When the magnetization has rotated more than  $90^\circ$  ( $\theta > 90^\circ$ ), the spin torque and damping term add up and the system is strongly damped towards the x-axis. A more analytical approach of this problem can be found in Ref. [40]. In the next section, an analytical expression will be derived for a situation where the magnetization is in a stable precessional motion induced by a microwave frequency (GHz) magnetic field.

### 6.4.1 Theory of ferromagnetic resonance (FMR)

The ferromagnetic resonance (FMR) technique is widely used to study the coherent magnetization precession induced by a microwave magnetic field. The precessional motion depends on the externally applied static magnetic field  $H_{\text{ext}}$  and the microwave angular frequency  $\omega$  and can be calculated using the LLG equation (without the Slonczewski term). In the limit of small angle precession of the magnetization of a thin ferromagnetic microstrip, the magnetization motion can be expressed in terms of the susceptibilities  $\chi_y$  and  $\chi_z$ . Consider a strip with an uniform equilibrium magnetization  $\vec{M} = (m_x, m_y, m_z)$  along the  $\hat{x}$  direction with a saturation magnetization  $M_s$ . The external field is also applied in the  $\hat{x}$  direction such that  $\vec{H}_{\text{ext}} = (h_0, 0, 0)$ , while the microwave field  $H_m = (0, 0, h_1)$  is in the  $\hat{z}$  direction. The total field inside the strip can now be written as  $\vec{H} = (h_0 - N_x m_x, -N_y m_y, h_1 - N_z m_z)$  where the demagnetizing fields are included using the demagnetizing factors  $N_x$ ,  $N_y$  and  $N_z$ . The LLG equation (Eq. 6.5) without the spin transfer torque term can now be filled in for the different components of the magnetization:

$$\begin{aligned} \dot{m}_x &= -\gamma(h_1 + (N_y - N_z)m_z)m_y + \frac{\alpha}{M_s}(m_y\dot{m}_z - m_z\dot{m}_y) \\ \dot{m}_y &= -\gamma(h_0 - (N_x - N_z)m_x)m_z + \frac{\alpha}{M_s}(m_z\dot{m}_x - m_x\dot{m}_z) + \gamma h_1 m_x \\ \dot{m}_z &= \gamma(h_0 - (N_x - N_y)m_x)m_y + \frac{\alpha}{M_s}(m_x\dot{m}_y - m_y\dot{m}_x) \end{aligned} \quad (6.6)$$

For a small angle precessional motion, these equations can be simplified by assuming that  $\frac{d\vec{M}_x}{dt} = 0$  and  $\vec{M}(t) = (M_s, m_y(t), m_z(t))$ :

$$\begin{aligned} \dot{m}_y &= -\omega_z m_z - \alpha \dot{m}_z + \omega_1 M_s \\ \dot{m}_z &= \omega_y m_y + \alpha \dot{m}_y \end{aligned} \quad (6.7)$$

with  $\omega_y = \gamma(h_0 - (N_x - N_y)M_s)$ ,  $\omega_z = \gamma(h_0 - (N_x - N_z)M_s)$  and  $\omega_1 = \gamma h_1$ . Combining both equations and by disregarding the  $\alpha^2$  term, the second derivative gives  $\ddot{m}_y + \alpha(\omega_y + \omega_z)\dot{m}_y + \omega_y\omega_z m_y = \dot{\omega}_1 M_s$ . Suppose the microwave field equals  $h_1(t) = h_1 \cos \omega t$ , this equation becomes  $\ddot{m}_y + \alpha(\omega_y + \omega_z)\dot{m}_y + \omega_y\omega_z m_y = -\omega\omega_1 M_s \sin \omega t$ .



The steady state solution to this problem can be written as the sum of a sine and cosine function. The magnetization is split up into in-phase and out-of-phase (with the microwave field) susceptibilities via  $m_y = \chi'_y M_s \omega_1 \cos \omega t + \chi''_y M_s \omega_1 \sin \omega t$  and  $m_z = \chi'_z M_s \omega_1 \cos \omega t + \chi''_z M_s \omega_1 \sin \omega t$ , where:

$$\begin{aligned}\chi'_y &= \frac{\alpha \omega^2 (\omega_y + \omega_z)}{(\omega^2 - \omega_y \omega_z)^2 + (\alpha \omega)^2 (\omega_y + \omega_z)^2} \\ \chi''_y &= \frac{\omega (\omega^2 - \omega_y \omega_z)}{(\omega^2 - \omega_y \omega_z)^2 + (\alpha \omega)^2 (\omega_y + \omega_z)^2}\end{aligned}\quad (6.8)$$

The  $\chi'_z$  and  $\chi''_z$  are related via  $\chi'_z = \alpha \chi'_y - \omega_y / \omega \chi''_y$  and  $\chi''_z = \alpha \chi''_y + \omega_y / \omega \chi'_y$ , respectively. In Figure 6.3a the in- and out-of-phase susceptibilities for  $m_z$  are displayed as a function of magnetic field for an infinite thin film and for a fixed driving frequency of 10 GHz. At the resonance field, the amplitude is maximized and  $m_z$  is exactly out-of-phase with the applied microwave magnetic field in the  $\hat{z}$  direction. An optimal absorption of energy from the microwave field is then realized because the energy absorption is given by:

$$\frac{dE}{dt} = \vec{M} \cdot \frac{d\vec{B}}{dt} \quad (6.9)$$

The field  $B = \mu_0(\vec{H} + \vec{M})$  includes both the magnetic fields  $\vec{H}$  and the magnetization  $\vec{M}$ . However, since the magnetization cancels out in the dot product of Eq. 6.9, one needs to take into account only the applied microwave field and the demagnetization fields. By averaging out all the contributions of the demagnetizing fields which vary with a frequency  $\omega$  or  $2\omega$ , the absorption of energy becomes proportional to the microwave field:

$$\left\langle \vec{M} \cdot \frac{d\vec{B}}{dt} \right\rangle = -\chi''_z \omega_1 \omega h_1 M_s \langle \sin^2 \omega t \rangle = -\frac{\chi''_z \omega_1^2 \omega M_s}{2\gamma} \quad (6.10)$$

Hence,  $\langle dE/dt \rangle$  depends purely on the the out-of-phase component of  $\chi_z$ . The temperature increase due to the energy absorption and dissipation of the ferromagnetic material is calculated with finite-element methods using Comsol Multiphysics (version 4.1). For the calculations, the thermoelectric model as described in Section 2.4 is used. The dissipation during ferromagnetic resonance is implemented in the model by adding the following extra source term to Eq. 2.9:

$$\vec{\nabla} \cdot \vec{Q} = -\frac{\chi''_z \omega_1^2 \omega M_s}{2\gamma} \quad (6.11)$$

Here we assumed that the heat input is uniform throughout the whole ferromagnetic material, which is valid for the macrospin approach. This gives rise to a temperature increase of approximately 30 mk for a thin film of Py ( $25 \mu\text{m} \times 25 \mu\text{m}$

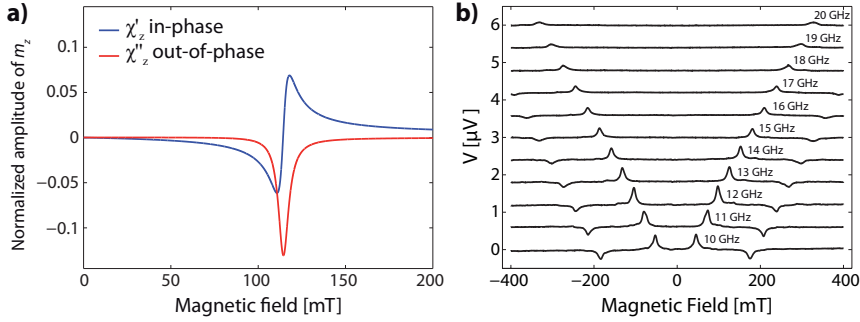


**Figure 6.3:** (a) In- and out-of-phase susceptibility for  $m_z$ . At the resonance condition, the motion of  $m_z$  is exactly out-of-phase with the applied microwave field, leading to optimal absorption of energy from the field. The susceptibility is normalized such that a precession angle of  $90^\circ$  would correspond to a susceptibility of 1. (b) Set of FMR measurements for different frequencies as a function of the externally applied magnetic field. The measurements are performed using a frequency modulation technique of two alternating frequencies which are separated by 5 GHz. The peaks and dips correspond to the resonance for the low and high frequency, respectively.

$\times 50$  nm) on top of a  $\text{SiO}_2$  substrate. Experimentally, this effect has been demonstrated in a similar system and will be discussed in Chapter 7 of this thesis. The electrical detection of ferromagnetic resonance is the subject of the next section.

### 6.4.2 Detection of ferromagnetic resonance

Ferromagnetic resonance can be observed with various experimental techniques such as for example stripline, vector network analyzer, pulsed inductive microwave magnetometer [41] or thermal techniques [42, 43]. The methods discussed in this thesis are based on the anisotropic magnetoresistance effect (Section 6.3) [44, 37] and thermoelectricity (Chapter 7). Figure 6.3b shows a set of measurements of the AMR voltage that is detected in a ferromagnetic microstrip (depicted in Fig. 6.1a). For different microwave frequencies the AMR voltage is measured as a function of the externally applied magnetic field. In order to increase the signal to noise ratio and to remove spurious effects, these measurements are often performed using a frequency modulation technique. In this measurement the applied microwave frequency is alternated between two different values ( $f_{\text{low}}$  and  $f_{\text{high}}$ ) separated by 5 GHz. A lock-in amplifier, tuned to the same frequency, can pick up the difference in AMR voltage between these two frequencies. Since the resonance conditions can not

be fulfilled for both frequencies at the same magnetic field strength, the observed voltage corresponds essentially to the difference in the AMR voltage between in- and off-resonance. Hence, the current  $I_{dc}$  multiplied with the resistance change,  $V = I_{dc}\Delta R \sin^2 \theta$ , provides us with a way to obtain the precession angle  $\theta$ . The peaks and dips of Fig. 6.3b represent the ferromagnetic resonance for the low and high frequency, respectively.

## 6.5 OOMMF Simulations

The OOMMF (Object Oriented Micromagnetic Framework) project [45] from the National Institute of Standards and Technology (NIST) is an open source micromagnetic program for solving the LLG equation (Eq. 6.5). OOMMF is capable of calculating the magnetization motion of complex multi-domain magnetic structures and includes both external and demagnetizing fields as well as anisotropy and exchange interactions. Here, OOMMF has been used to calculate the dissipated power during ferromagnetic resonance in ferromagnetic microstrip using the macrospin approach. This macrospin assumption means that the magnetization is represented by a single domain, which greatly reduces the computation time.

Figure 6.4a shows the total energy versus time of the system ( $2000 \times 400 \times 50$  nm) which is brought into ferromagnetic resonance. The total energy consists of the sum of the Zeeman and demagnetizing energy, whereas the exchange energy is disregarded because of the macrospin approximation. At  $t = 0$  both the externally applied static and microwave magnetic fields are switched on and the precession angle starts to increase. After approximately 10 ns the system is in resonance and the total energy becomes constant. In this situation the energy that is added to the system by the oscillating magnetic field equals the energy lost through heat dissipation. At  $t = 25$  ns, the microwave magnetic field is abruptly switched off and the total energy will decrease due to damping of the magnetization motion. By determining the slope of the total energy directly after the microwave field is set to zero, the heat dissipation during the precessional motion is found. Unfortunately, there exists no possibility in OOMMF to calculate the dissipation directly by solving Eq. 6.9.

The simulation has been performed for a permalloy strip with a damping parameter of  $\alpha = 0.01$ . The time steps between two successive points were ranging from  $10^{-16}$  till  $10^{-14}$  s. An oscillating field with a frequency of 10 GHz and a magnitude of 1 mT was used. The dissipation has been determined for several values of the static magnetic field, ranging from 20 to 60 mT and is plotted in Figure 6.4b. At the resonance field ( $H = 39.5$  mT), the obtained dissipation is 43 nW. This value can be compared to the value found using Eq. 6.11, which will give for an equal volume

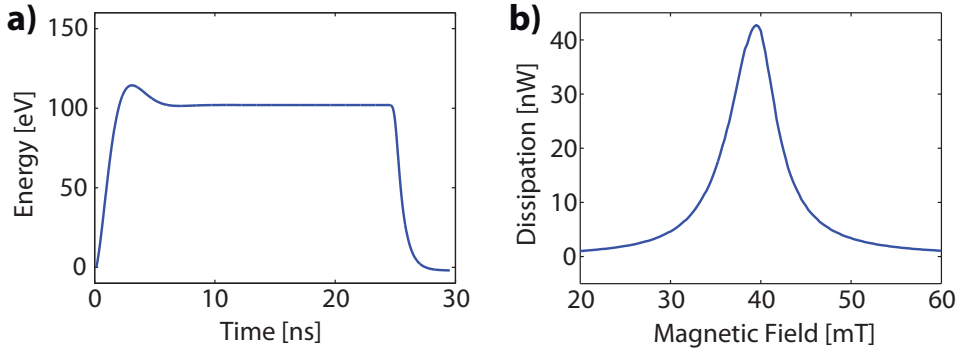


**Figure 6.4:** (a) Macrospin simulation of the sum of the Zeeman and demagnetizing energy for a system which is brought into ferromagnetic resonance. At  $t = 0$  ns, the microwave (10 GHz) and static magnetic field are switched on and the system is driven into resonance. During the stable precessional motion (after  $t = 10$  ns), the total energy is constant. The microwave field is suddenly switched off at  $t = 25$  ns and consequently, the energy drops to zero due to the damping. From the slope of the energy, the dissipation during the resonance can be derived. (b) Dissipation versus externally applied magnetic field. The resonance conditions are fulfilled for a magnetic field of 39 mT and exactly at the resonance the obtained dissipation is 43 nW.

a dissipation of 26 nW. The discrepancy can be attributed to the different demagnetization factors. In Eq. 6.11, the demagnetization factors for a thin film are used, whereas the OOMMF simulation is performed for a microstrip. In Chapter 7 of this thesis the dissipation during ferromagnetic resonance is demonstrated experimentally.

## 6.6 Conclusion and outlook

An overview of recent experiments on magnetization dynamics has been given where angular momentum was transferred from injected spin currents to the local magnetization and vice versa. The spin-transfer torque effect as a means to induce magnetization dynamics has been described and related to its reciprocal mechanism, the spin pumping effect. An analytical expression for the magnetization dynamics during ferromagnetic resonance is derived. It has been shown that the self-energy and demagnetization energy are the most important energies to take into account when the dissipation during ferromagnetic resonance is calculated. Furthermore, the comparison between numerical micromagnetic simulations and the

analytical solution for the dissipation showed a small discrepancy, which was attributed to the different magnetization factors used.

Interesting new experimental possibilities can be found in the combination of spin caloritronics and magnetization dynamics. For example, the charge currents that drive spin-transfer torque oscillators or memory elements can be replaced with heat currents in future devices. Alternatively, heat and charge currents can work alongside, thereby reducing the critical current needed for magnetization reversal. The opposite approach would be to achieve spin-dependent Peltier cooling/heating, as discussed in Chapter 4, by a spin-pumping current. Another innovative concept is the generation of spin currents using the spin-Seebeck effect as discovered by Uchida *et al.* [46]. The interaction between the magnetization dynamics and thermal gradients is still not fully understood and a systematic study of all these effects will definitely increase the current understanding of both spin caloritronics and magnetization dynamics.

## Bibliography

- [1] I. Žutić and S. Das Sarma, "Spintronics: Fundamentals and applications," *Reviews of Modern Physics* **76**, pp. 323–410, Apr. 2004.
- [2] D. Ralph and M. Stiles, "Spin transfer torques," *Journal of Magnetism and Magnetic Materials* **320**, pp. 1190–1216, Dec. 2007.
- [3] J. Slonczewski, "Current-driven excitation of magnetic multilayers," *Journal of Magnetism and Magnetic Materials* **159**, p. L1, June 1996.
- [4] L. Berger, "Emission of spin waves by a magnetic multilayer traversed by a current," *Physical Review B* **54**(13), p. 9353, 1996.
- [5] A. Brataas, G. Bauer, and P. Kelly, "Non-collinear magnetoelectronics," *Physics Reports* **427**, pp. 157–255, Apr. 2006.
- [6] P. M. Braganca, I. N. Krivorotov, O. Ozatay, a. G. F. Garcia, N. C. Emley, J. C. Sankey, D. C. Ralph, and R. a. Buhrman, "Reducing the critical current for short-pulse spin-transfer switching of nanomagnets," *Applied Physics Letters* **87**(11), p. 112507, 2005.
- [7] J. Katine, F. Albert, R. Buhrman, E. Myers, and D. Ralph, "Current-driven magnetization reversal and spin-wave excitations in Co /Cu /Co pillars," *Physical review letters* **84**, p. 3149, Apr. 2000.
- [8] Y. Huai, F. Albert, P. Nguyen, M. Pakala, and T. Valet, "Observation of spin-transfer switching in deep submicron-sized and low-resistance magnetic tunnel junctions," *Applied Physics Letters* **84**(16), p. 3118, 2004.
- [9] M. Hatami, G. Bauer, Q. Zhang, and P. Kelly, "Thermal Spin-Transfer Torque in Magnetoelectronic Devices," *Physical Review Letters* **99**, p. 066603, Aug. 2007.
- [10] H. Yu, S. Granville, D. P. Yu, and J.-P. Ansermet, "Evidence for Thermal Spin-Transfer Torque," *Physical Review Letters* **104**, p. 146601, Apr. 2010.
- [11] T. Yang, T. Kimura, and Y. Otani, "Giant spin-accumulation signal and pure spin-current-induced reversible magnetization switching," *Nature Physics* **4**, pp. 851–854, Oct. 2008.
- [12] J. Z. Sun, M. C. Gaidis, E. J. OSullivan, E. a. Joseph, G. Hu, D. W. Abraham, J. J. Nowak, P. L. Trouilloud, Y. Lu, S. L. Brown, D. C. Worledge, and W. J. Gallagher, "A three-terminal spin-torque-driven magnetic switch," *Applied Physics Letters* **95**(8), p. 083506, 2009.
- [13] F. J. Jedema, H. B. Heersche, A. T. Filip, J. J. A. Baselmans, and B. J. van Wees, "Electrical detection of spin precession in a metallic mesoscopic spin valve.," *Nature* **416**, p. 713, Apr. 2002.
- [14] N. Tombros, C. Jozsa, M. Popinciuc, H. T. Jonkman, and B. J. van Wees, "Electronic spin transport and spin precession in single graphene layers at room temperature.," *Nature* **448**, p. 57, Aug. 2007.

- [15] M. Stiles, J. Xiao, and A. Zangwill, "Phenomenological theory of current-induced magnetization precession," *Physical Review B* **69**, p. 054408, Feb. 2004.
- [16] O. Boulle, V. Cros, J. Grollier, L. G. Pereira, C. Deranlot, F. Petroff, G. Faini, J. Barnaś, and a. Fert, "Shaped angular dependence of the spin-transfer torque and microwave generation without magnetic field," *Nature Physics* **3**, pp. 492–497, May 2007.
- [17] D. Houssameddine, U. Ebels, B. Delaët, B. Rodmacq, I. Firastrau, F. Ponthenier, M. Brunet, C. Thirion, J.-P. Michel, L. Prejbeanu-Buda, M.-C. Cyrille, O. Redon, and B. Dieny, "Spin-torque oscillator using a perpendicular polarizer and a planar free layer.," *Nature materials* **6**, p. 447, June 2007.
- [18] S. I. Kiselev, J. C. Sankey, I. N. Krivorotov, N. C. Emley, R. J. Schoelkopf, R. a. Buhrman, and D. C. Ralph, "Microwave oscillations of a nanomagnet driven by a spin-polarized current.," *Nature* **425**, p. 380, Sept. 2003.
- [19] I. N. Krivorotov, N. C. Emley, J. C. Sankey, S. I. Kiselev, D. C. Ralph, and R. a. Buhrman, "Time-domain measurements of nanomagnet dynamics driven by spin-transfer torques.," *Science (New York, N.Y.)* **307**, pp. 228–31, Jan. 2005.
- [20] A. Tulapurkar, Y. Suzuki, A. Fukushima, H. Kubota, H. Maehara, K. Tsunekawa, D. D. Djayaprawira, N. Watanabe, and S. Yuasa, "Spin-torque diode effect in magnetic tunnel junctions.," *Nature* **438**, p. 339, Nov. 2005.
- [21] V. E. Demidov, S. Urazhdin, E. R. J. Edwards, and S. O. Demokritov, "Wide-range control of ferromagnetic resonance by spin Hall effect," *Applied Physics Letters* **99**(17), p. 172501, 2011.
- [22] L. Liu, T. Moriyama, D. Ralph, and R. Buhrman, "Spin-Torque Ferromagnetic Resonance Induced by the Spin Hall Effect," *Physical Review Letters* **106**, p. 036601, Jan. 2011.
- [23] R. H. Silsbee, A. Janossy, and P. Monod, "Coupling between ferromagnetic and conduction-spin-resonance modes at a ferromagnetic-normal-metal interface," *Phys. Rev. B* **19**, pp. 4382–4399, May 1979.
- [24] Y. Tserkovnyak, A. Brataas, and G. Bauer, "Enhanced Gilbert Damping in Thin Ferromagnetic Films," *Physical Review Letters* **88**, p. 117601, Feb. 2002.
- [25] Y. Tserkovnyak, A. Brataas, and G. Bauer, "Spin pumping and magnetization dynamics in metallic multilayers," *Physical Review B* **66**, p. 224403, Dec. 2002.
- [26] Y. Tserkovnyak, A. Brataas, G. E. W. Bauer, and B. I. Halperin, "Nonlocal Magnetization Dynamics in Ferromagnetic Heterostructures," *ChemInform* **37**, July 2006.
- [27] A. Brataas, Y. Tserkovnyak, G. Bauer, and B. Halperin, "Spin battery operated by ferromagnetic resonance," *Physical Review B* **66**, p. 060404(R), Aug. 2002.
- [28] K. Lenz, T. Toliski, J. Lindner, E. Kosubek, and K. Baberschke, "Evidence of spin-pumping effect in the ferromagnetic resonance of coupled trilayers," *Physical Review B* **69**, p. 144422, Apr. 2004.
- [29] S. Mizukami, Y. Ando, and T. Miyazaki, "Effect of spin diffusion on Gilbert damping for a very thin permalloy layer in Cu/permalloy/Cu/Pt films," *Physical Review B* **66**, pp. 1–9, Sept. 2002.

- [30] B. Heinrich, C. Burrowes, E. Montoya, B. Kardasz, E. Girt, Y.-Y. Song, Y. Sun, and M. Wu, "Spin Pumping at the Magnetic Insulator (YIG)/Normal Metal (Au) Interfaces," *Physical Review Letters* **107**, p. 066604, Aug. 2011.
- [31] K. Ando, S. Takahashi, J. Ieda, H. Kurebayashi, T. Trypiniotis, C. Barnes, S. Maekawa, and E. Saitoh, "Electrically tunable spin injector free from the impedance mismatch problem," *Nature Materials* **10**(9), pp. 655–659, 2011.
- [32] O. Mosendz, V. Vlaminck, J. Pearson, F. Fradin, G. Bauer, S. Bader, and A. Hoffmann, "Detection and quantification of inverse spin Hall effect from spin pumping in permalloy/normal metal bilayers," *Physical Review B* **82**, p. 214403, Dec. 2010.
- [33] C. Sandweg, Y. Kajiwara, A. Chumak, A. Serga, V. Vasyuchka, M. Jungfleisch, E. Saitoh, and B. Hillebrands, "Spin Pumping by Parametrically Excited Exchange Magnons," *Physical Review Letters* **106**, p. 216601, May 2011.
- [34] Y. Kajiwara, K. Harii, S. Takahashi, J. Ohe, K. Uchida, M. Mizuguchi, H. Umezawa, H. Kawai, K. Ando, K. Takanashi, S. Maekawa, and E. Saitoh, "Transmission of electrical signals by spin-wave interconversion in a magnetic insulator," *Nature* **464**, p. 262, Mar. 2010.
- [35] J. Coey, *Magnetism and magnetic materials*, Cambridge University Press, 2010.
- [36] E. C. Stoner and E. P. Wohlfarth, "A Mechanism of Magnetic Hysteresis in Heterogeneous Alloys," *Phil. Trans. R. Soc. Lond. A* **240**(826), p. 599, 1948.
- [37] M. V. Costache, S. M. Watts, M. Sladkov, C. H. van der Wal, and B. J. van Wees, "Large cone angle magnetization precession of an individual nanopatterned ferromagnet with dc electrical detection," *Applied Physics Letters* **89**(23), p. 232115, 2006.
- [38] A. Slachter, F. L. Bakker, and B. J. van Wees, "Anomalous Nernst and anisotropic magnetoresistive heating in a lateral spin valve," *Physical Review B* **84**, p. 020412(R), July 2011.
- [39] G. D. Fuchs, J. C. Sankey, V. S. Pribiag, L. Qian, P. M. Braganca, a. G. F. Garcia, E. M. Ryan, Z.-P. Li, O. Ozatay, D. C. Ralph, and R. a. Buhrman, "Spin-torque ferromagnetic resonance measurements of damping in nanomagnets," *Applied Physics Letters* **91**(6), p. 062507, 2007.
- [40] J. Sun, "Spin-current interaction with a monodomain magnetic body: A model study," *Physical Review B* **62**, p. 570, July 2000.
- [41] S. S. Kalarickal, P. Krivosik, M. Wu, C. E. Patton, M. L. Schneider, P. Kabos, T. J. Silva, and J. P. Nibarger, "Ferromagnetic resonance linewidth in metallic thin films: Comparison of measurement methods," *Journal of Applied Physics* **99**(9), p. 093909, 2006.
- [42] R. Meckenstock, "Invited Review Article: Microwave spectroscopy based on scanning thermal microscopy: resolution in the nanometer range.," *The Review of scientific instruments* **79**, p. 041101, Apr. 2008.
- [43] F. Sakran, a. Coptly, M. Golosovsky, D. Davidov, and P. Monod, "Scanning ferromagnetic resonance microscopy and resonant heating of magnetite nanoparticles: Demonstration of thermally detected magnetic resonance," *Applied Physics Letters* **84**(22), p. 4499, 2004.



- 
- [44] M. V. Costache, M. Sladkov, C. H. van der Wal, and B. J. van Wees, "On-chip detection of ferromagnetic resonance of a single submicron Permalloy strip," *Applied Physics Letters* **89**(19), p. 192506, 2006.
- [45] M. Donahue and D. G. Porter *OOMMF User's guide, Version 1.0, Interagency Report NISTIR 6376, NIST, Gaithersburg, MD, 1999. See also <http://math.nist.gov/oommf> for more information* .
- [46] K. Uchida, S. Takahashi, K. Harii, J. Ieda, W. Koshibae, K. Ando, S. Maekawa, and E. Saitoh, "Observation of the spin Seebeck effect.," *Nature* **455**, p. 778, Oct. 2008.



## Chapter 7

---

# Thermoelectric detection of ferromagnetic resonance of a nanoscale ferromagnet

### Abstract

*We present thermoelectric measurements of the heat dissipated due to ferromagnetic resonance of a Permalloy strip. A microwave magnetic field, produced by an on-chip coplanar strip waveguide, is used to drive the magnetization precession. The generated heat is detected via Seebeck measurements on a thermocouple connected to the ferromagnet. The observed resonance peak shape is in agreement with the Landau-Lifshitz-Gilbert equation and is compared with thermoelectric finite element modeling. Unlike other methods, this technique is not restricted to electrically conductive media and is therefore also applicable to for instance ferromagnetic insulators.*

## 7.1 Introduction

Thermal effects in ferromagnetic materials are subject to extensive research since the discovery of the spin-Seebeck effect [1, 2, 3]. Recently, spin dynamics and (spin-) caloritronics, two popular branches of spintronics, started to come together as spin pumping induced by spin dynamics has been proposed as the origin of the spin-Seebeck effect [4, 5]. Magnetization dynamics has been studied thoroughly in magnetic systems as it is an important mechanism for future spintronic applications, e.g. for microwave generators [6, 7] and spin sources via spin pumping [8, 9]. However, dissipation mechanisms that accompany magnetization dynamics, and cause local heating, are still not fully understood [10, 11].

Here, we focus on a new aspect, the coupling between magnetization dynamics and the generation of heat. We deduce from thermoelectric measurements on a Permalloy (Py) island the heat dissipation during ferromagnetic resonance. This on-chip detection technique, based on the Seebeck effect, offers a novel method for characterizing ferromagnetic resonance and hence is distinctly different from other techniques, such as scanning thermal microscopy [12, 13]. Due to the thermal detection, electrical contact to the ferromagnet is in principle not required. Hence, this

method allows for FMR measurements on non-conductive materials like ferromagnetic insulators.

## 7.2 Heat generation during ferromagnetic resonance

When a ferromagnet is brought into resonance, energy is absorbed from the applied microwave field. This energy causes the magnetization  $\vec{M}$  to precess around an effective field  $\vec{H}$  and the motion is well described by the Landau-Lifshitz-Gilbert (LLG) equation  $d\vec{M}/dt = -\gamma\vec{M} \times \vec{H} + (\alpha/M_s)\vec{M} \times d\vec{M}/dt$  with  $\gamma = 176$  GHz/T the gyromagnetic ratio. The last term in the LLG equation describes the damping of the magnetization towards the direction of the effective field  $\vec{H}$ , using the phenomenological damping parameter  $\alpha$ . This process is purely dissipative and converts magnetostatic energy into heat. During ferromagnetic resonance (FMR) this continuous dissipation leads to heating of the ferromagnetic material.

In this experiment, we measured the temperature of a ferromagnet while subject to a microwave magnetic field. A ferromagnetic strip is placed close to the shortened end of a coplanar strip waveguide (CSW) as shown in Fig. 7.1. Microwave power is applied to the CSW, leading to an out of plane rf magnetic field. A static magnetic field  $h_0$  is applied along the easy axis of the magnet. In addition, a thermocouple consisting of a NiCu and Pt wire is connected to the ferromagnet by a Au bridge. In this way, the temperature can be measured by making use of the Seebeck effect. The Seebeck effect describes the generation of a voltage due to a temperature gradient,  $\nabla V = -S\nabla T$ , with  $S$  the material dependent Seebeck coefficient. The voltage that develops across the Pt wire is different than the voltage that develops across the NiCu wire, leading to a nonzero voltage between the two wires. This thermovoltage scales with the Seebeck coefficients ( $S_{\text{Pt}} - S_{\text{NiCu}}$ ) and the temperature difference ( $T_1 - T_0$ ). Note that NiCu is chosen because of its relatively high Seebeck coefficient ( $S_{\text{NiCu}} = -32\mu\text{V}/\text{K}$  and  $S_{\text{Pt}} = -5\mu\text{V}/\text{K}$ ). The Seebeck coefficients were determined in a separate device specifically designed to accurately determine the Seebeck coefficient of a material. In the following, we calculate the temperature rise during FMR from the dissipated power.

The energy of a ferromagnetic particle in a magnetic field, the Zeeman energy, is given by:

$$E = - \int_V \vec{M} \cdot \vec{B} dV \quad (7.1)$$

with  $\vec{M}$  the magnetization,  $\vec{B} = \mu_0 (\vec{H}_{\text{ext}} + \vec{H}_D/2)$  the sum of the externally applied magnetic field and the demagnetizing field and  $V$  the volume of the particle. Here,  $\vec{H}_D$  is divided by two to compensate for double counting because each element con-

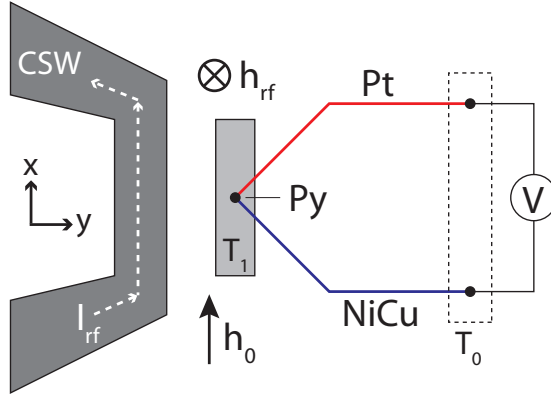


**Figure 7.1:** Concept of the thermoelectric detection of ferromagnetic resonance. A coplanar strip waveguide generates a microwave magnetic field  $h_{rf}$  in the  $\hat{z}$  direction acting on a small ferromagnetic strip. A static magnetic field  $h_0$  is applied along the  $\hat{x}$  axis. When the strip is brought into resonance, it absorbs energy from the field which is dissipated as heat. The dissipation is detected by a Pt-NiCu thermocouple which probes the temperature  $T_1$  of the ferromagnet with respect to a reference temperature  $T_0$  via the Seebeck effect.

tributes as a field source and as a moment in the integral [14]. For this experiment, a static magnetic field,  $h_0$ , is applied in the  $\hat{x}$  direction and a driving rf field,  $h_{rf} \cos \omega t$ , in the  $\hat{z}$  direction, making  $\vec{B} = (h_0 - N_x m_x/2, -N_y m_y/2, h_{rf} \cos \omega t - N_z m_z/2)$  with  $N_x$ ,  $N_y$  and  $N_z$  the demagnetization factors. The dissipation energy can now be calculated from the time derivative of  $E$ , assuming a uniform  $\vec{M}$  and  $\vec{B}$ :

$$\frac{dE}{dt} = -V \left( \frac{d\vec{M}}{dt} \cdot \vec{B} + \vec{M} \cdot \frac{d\vec{B}}{dt} \right) \quad (7.2)$$

where the first part of Eq. 7.2 expresses the dissipation due to the magnetization motion and the second part the energy absorbed from the microwave field. In equilibrium, the absorption of energy from the microwave field equals the dissipation,  $\langle dE/dt \rangle = 0$ , leading to heating of the ferromagnet. In order to find an expression for the dissipated power, we use a procedure similar to Ref. [15] where the magnetization dynamics is described by the linearized LLG equation. We assume that for small angle precessional motion  $dm_x/dt = 0$  such that  $m_x$  is constant and the solution to the Landau-Lifshitz-Gilbert (LLG) equation can be written in terms of the sum of in-phase and out-of-phase susceptibilities. The components  $m_y$  and  $m_z$  are now defined as  $m_y = \chi'_y \omega_1 M_s \cos \omega t + \chi''_y \omega_1 M_s \sin \omega t$  and

$m_z = \chi'_z \omega_1 M_s \cos \omega t + \chi''_z \omega_1 M_s \sin \omega t$  with:

$$\begin{aligned}\chi'_y &= \frac{\alpha \omega^2 (\omega_y + \omega_z)}{(\omega^2 - \omega_y \omega_z)^2 + (\alpha \omega)^2 (\omega_y + \omega_z)^2} \\ \chi''_y &= \frac{\omega (\omega^2 - \omega_y \omega_z)}{(\omega^2 - \omega_y \omega_z)^2 + (\alpha \omega)^2 (\omega_y + \omega_z)^2}\end{aligned}\quad (7.3)$$

Here,  $\omega$  is the frequency of the driving rf field,  $\omega_y = \gamma(h_0 - (N_x - N_y)M_s)$ ,  $\omega_z = \gamma(h_0 - (N_x - N_z)M_s)$ ,  $\omega_1 = \gamma h_{rf}$  and  $M_s$  the saturation magnetization. The  $\chi'_z$  and  $\chi''_z$  are related via  $\chi'_z = \alpha \chi'_y - \omega_y / \omega \chi''_y$  and  $\chi''_z = \alpha \chi''_y + \omega_y / \omega \chi'_y$ , respectively. With these expressions for  $m_x$ ,  $m_y$ ,  $m_z$  and  $B_x$ ,  $B_y$ ,  $B_z$  one can easily find its time derivatives and calculate the relevant dot product of Eq. 7.2. We are not interested in high frequency variations in the dissipated power and hence, average out all contributions that vary with a frequency  $\omega$  or  $2\omega$  and find:

$$\left\langle \frac{dE}{dt} \right\rangle_{\text{dissipation}} = \frac{\chi''_z \omega_1^2 \omega M_s V}{2\gamma} \quad (7.4)$$

From this expression we can deduce that the resonance peak shape of the dissipated power is determined by  $\chi''_z$  and scales with the applied microwave field and frequency. In order to convert this power into a temperature rise, we make use of 3D finite element thermoelectric modeling. For details about the modeling we refer to earlier publications [16, 17].

### 7.3 Experimental realization

The samples are fabricated using a three-step electron beam lithography process on top of a thermally oxidized Si substrate. A scanning electron microscope (SEM) image of the investigated devices is shown in Fig. 7.2. The devices consist of a 50nm thick Py strip ( $2 \mu\text{m} \times 400 \text{ nm}$ ) close to a 100 nm thick Au coplanar strip waveguide. The CSW is made using an optical lithography process. In the thermoelectric device (Fig. 7.2a), there are two 40 nm thick contacts (Pt and NiCu) forming a thermocouple. The Py island is connected to the thermocouple by a highly thermal conductive Au contact (thickness: 120 nm). The other side of the thermocouple is connected by 120 nm thick Au contacts to the bonding pads. In the case of the anisotropic magnetoresistance (AMR) device (Fig. 7.2b), four 120 nm thick Au contacts directly connect to the Py strip. The NiCu is deposited by DC sputtering to preserve the original alloy composition (45% Ni, 55% Cu). To avoid lift-off problems a double-layer resist technique with a large undercut (PMMA-MA and PMMA 950K) is used. The Au, Pt and Py are deposited using an e-beam evaporator (base pressure  $1 \times 10^{-7}$  mbar)

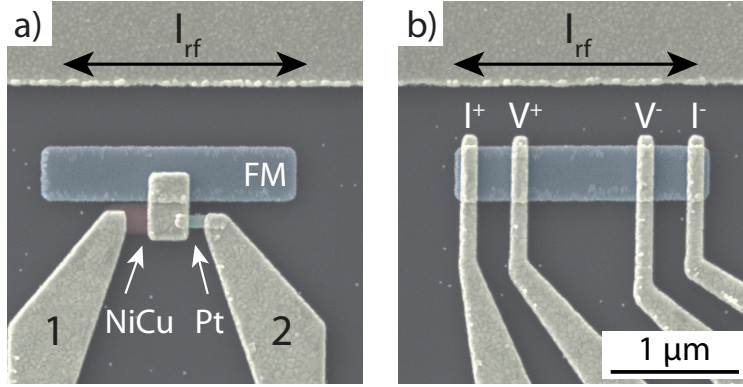


**Figure 7.2:** (a) Scanning electron microscope (SEM) image of the thermoelectric FMR device. (b) Image of a device with four contacts for dc AMR detection of FMR.

and a single layer resist (PMMA 950K). Prior to the Au deposition, the NiCu, Pt and Py surfaces are cleaned with Ar ion milling.

For the measurements, we have used a frequency modulation method to obtain a better signal to noise ratio and to remove background voltages due to heating of the CSW short. The microwave field frequency is alternated between two different values with a separation of 5 GHz. A lock-in amplifier, tuned to the same frequency (17 Hz), measures the difference in dc voltage across contacts 1 and 2 (Fig. 7.2a) between the two frequencies ( $V = V_{f=\text{high}} - V_{f=\text{low}}$ ). Because of the large separation between  $V_{f=\text{low}}$  and  $V_{f=\text{high}}$ , they can not both fulfill the resonance condition at a specific magnetic field. With this method, one effectively measures the difference in the Seebeck or AMR voltage when the ferromagnet is in- and off-resonance. All measurements were performed at room temperature.

## 7.4 Thermoelectric detection of FMR

Fig. 7.3a shows the measured Seebeck voltage as a function of magnetic field for different rf field frequencies (10 - 20 GHz) for 12 dBm rf power. The position of the peaks and dips correspond to the resonance field for  $f_{\text{low}}$  and  $f_{\text{high}}$ , respectively. We have plotted the peak position as a function of the applied rf frequency in Fig. 7.3b and found peak heights ranging from 46 nV at 10 GHz to 105 nV at 17 GHz. For a uniform precessional mode, the resonance field is related to  $\omega$  by the Kittel equation [18]:

$$\omega^2 = \gamma^2 (h_0 - (N_x - N_y)M_s)(h_0 - (N_x - N_z)M_s) \quad (7.5)$$

The line corresponds to a fit of Eq. 7.5 and confirms the precessional motion. We obtained the following fitting parameters:  $N_x = 0.01$ ,  $N_y = 0.09$ ,  $N_z = 0.90$  and  $\mu_0 M_s = 1.11$  T. These parameters have been used to calculate the dissipated power of Eq. 7.4 for different frequencies. However, in order to do this accurately one first need to determine the magnitude of the rf magnetic field experimentally.

To obtain the correct experimental value for the magnitude of the rf magnetic field, we have measured the dc anisotropic magnetoresistance (AMR) in a dedicated device with a four-terminal geometry (shown in Fig. 7.2b). The AMR effect describes the dependence of the resistance on the angle  $\theta$  between the current  $\vec{I}$  and the direction of magnetization  $\vec{M}$  by  $R = R_0 - \Delta R \sin^2 \theta$ , where  $R_0$  is the resistance of the strip when  $\vec{I}$  and  $\vec{M}$  are parallel, and  $\Delta R$  the difference in resistance between the parallel and perpendicular alignment of  $\vec{I}$  and  $\vec{M}$ . A measurement of  $R$  as a function of a perpendicular applied magnetic field is plotted in Fig. 7.4c. From this measurement, we determined the magnitude of the AMR effect and found  $\Delta R/R_0 = 1.5\%$ . For a steady resonant precession, the average cone angle  $\theta_c$  of the precession can now be extracted from the observed AMR voltage.

Fig. 7.4a displays the AMR voltage versus magnetic field for different microwave field frequencies. For this measurement, we have used a dc current  $I_{dc}$  of  $300 \mu\text{A}$ . The obtained voltage now corresponds to the dc current multiplied with the resistance change, being  $V = I_{dc} \Delta R \sin^2 \theta_c$ , and the precession angle can be extracted. Using Eq. 7.3 and an expression for the average cone angle:

$$\langle \theta_c^2 \rangle = \omega_1^2 (\chi_y'^2 + \chi_y''^2 + \chi_z'^2 + \chi_z''^2) / 2 \quad (7.6)$$

one can deduce  $h_{r,f} = \omega_1 / \gamma$  from a fit of the measured peak height, and the result is plotted in Fig. 7.4b for a microwave power of 12 dBm. The field strength is found to decrease twofold when the frequency is increased from 10 to 20 GHz. We attribute this to frequency dependent attenuation of the microwave signal, leading to smaller rf fields at higher frequencies.

Now we can calculate, using finite element modeling in Comsol Multiphysics, the Seebeck voltage that is generated due to the heating of the ferromagnet. In this model we impose the constant heat flux, given by Eq. 7.4, through the top layer of the ferromagnet and solve the thermoelectric model [16, 17]. Here we use the electrical conductivities and Seebeck coefficients obtained from measurements in a dedicated test device, whereas the thermal conductivities are taken from literature. Both, the heat flux and the calculated Seebeck voltage are plotted in Fig. 7.3c (solid lines) for multiple frequencies. Peak heights ranging from 98 till 197 nV are calculated. For comparison, the observed peak height of Fig. 7.3a is replotted in Fig. 7.3c as black dots.

For a fixed rf field strength, the Seebeck voltage should increase monotonically



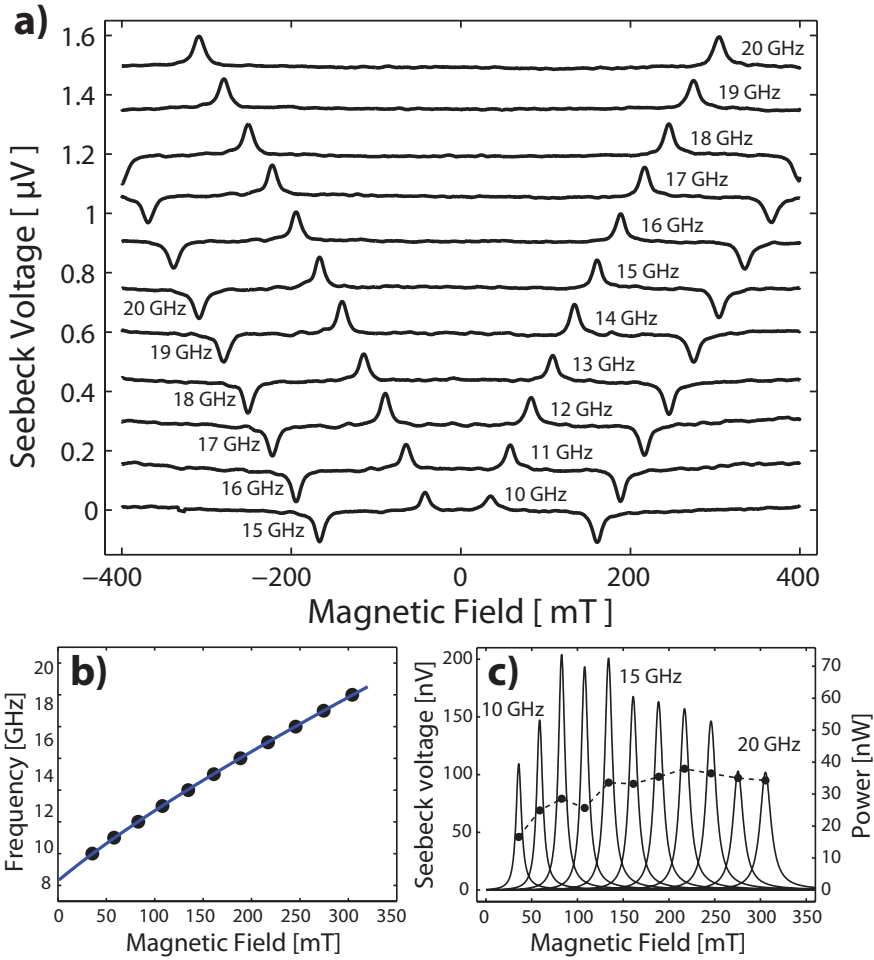


**Figure 7.3:** (a) Series of Seebeck voltage versus magnetic field measurements for 11 different frequencies. The traces are offset by 150 nV for clarity. Due to the modulation technique using two driving frequencies that are 5 GHz apart, peaks and dips are observed at the resonance fields for both frequencies. (b) Frequency versus the magnetic field at the center of the resonance peak. The line corresponds to a fit of the Kittel equation. (c) Generated power and corresponding Seebeck voltage calculated using Eq. 7.4 and thermoelectric finite-element modeling for multiple frequencies. The measured peak heights of a) are indicated by the black dots.

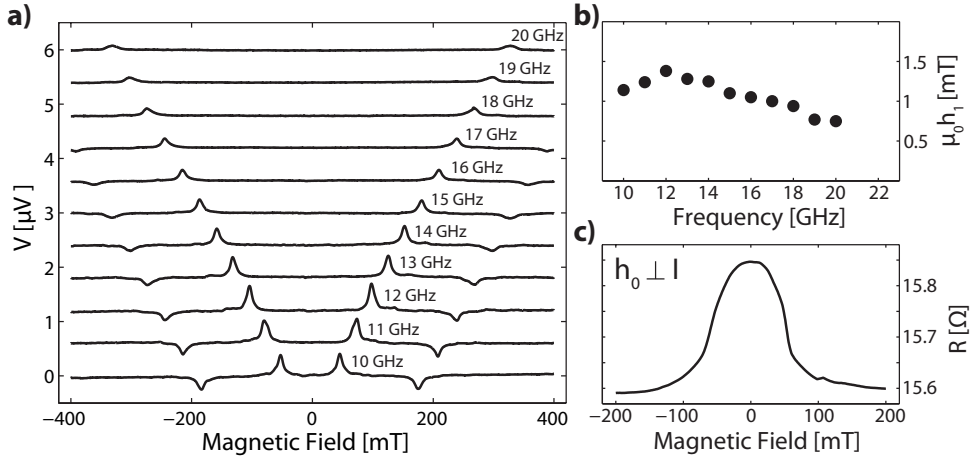


**Figure 7.4:** (a) AMR voltage vs. magnetic field. Peaks and dips are observed for the resonance fields of the two driving frequencies (5 GHz apart). The different traces are offset for clarity reasons. (b) The magnitude of the rf field is extracted from the peak height of the resonance ( $V = I_{dc} \Delta R \sin^2 \theta_c$ ). c) Anisotropic magnetoresistance measurement with  $\vec{I}$  and  $\vec{B}$  perpendicularly aligned.

with frequency due to an increasing dissipation (see Eq. 7.4). However, because of the experimental variation in rf field strength for different frequencies, a specific relation between the calculated Seebeck voltage and the frequency is found (Fig. 7.3c). The experimental data is in agreement with the calculations within a factor of two and follows partially the same trend. This discrepancy is attributed to small sample to sample variations in the rf field strength. Since the AMR measurements are performed on a separate device, the fields can differ for the thermoelectric device. Moreover, small shifts in the contact area of the thermocouple can lead to changes in the heat transport and hence, different thermo voltages. Uncertainties in the thermal conductivities of the materials in the finite element modeling do introduce an extra error, but based on previous work [16, 17] we expect the modeling to be accurate within a factor of two.

Furthermore, circulating rf currents combined with an oscillating magnetoresistance at the same frequency can cause dc voltages via a rectifying effect and mimic the observed thermal behavior in our devices [15]. We have excluded these effects by using a similar device with an Au-Au thermocouple such that the Seebeck effect vanishes. For this device we observed a flat background voltage without peaks and dips. We note that thermal voltages can be of importance in other device geometries

where ferromagnets are electrically connected to nonmagnetic metals. For example, detection of interface voltages that arise due to spin-pumping [19, 20] cannot be easily distinguished from generated Seebeck voltages. Thorough temperature or material dependent measurements might offer a solution to discriminate between both mechanisms.

## 7.5 Conclusion

In conclusion, we have demonstrated a new thermoelectric detection technique for ferromagnetic resonance. The observed resonance peaks are in good agreement with the LLG equation and thermoelectric finite element modeling. Additionally, this technique can be applied on the nanoscale and is not limited to conductive ferromagnetic media. Thermal detection offers a valid, alternative method for studying the dissipation, i.e. the Gilbert damping term, in nanoscale ferromagnetic islands. We hope that these results stimulate research for new physical effects that arises from coupling between magnetization dynamics and caloritronics.

## Bibliography

- [1] K. Uchida, S. Takahashi, K. Harii, J. Ieda, W. Koshibae, K. Ando, S. Maekawa, and E. Saitoh, "Observation of the spin Seebeck effect.," *Nature* **455**, pp. 778–81, Oct. 2008.
- [2] C. M. Jaworski, J. Yang, S. Mack, D. D. Awschalom, J. P. Heremans, and R. C. Myers, "Observation of the spin-Seebeck effect in a ferromagnetic semiconductor," *Nature Materials* **9**, pp. 1–6, Sept. 2010.
- [3] K. Uchida, J. Xiao, H. Adachi, J. Ohe, S. Takahashi, J. Ieda, T. Ota, Y. Kajiwara, H. Umezawa, H. Kawai, G. E. W. Bauer, S. Maekawa, and E. Saitoh, "Spin Seebeck insulator," *Nature Materials* **9**, pp. 1–4, Sept. 2010.
- [4] J. Xiao, G. E. W. Bauer, K. Uchida, E. Saitoh, and S. Maekawa, "Theory of magnon-driven spin seebeck effect," *Phys. Rev. B* **81**, p. 214418, Jun 2010.
- [5] H. Adachi, J.-i. Ohe, S. Takahashi, and S. Maekawa, "Linear-response theory of spin seebeck effect in ferromagnetic insulators," *Phys. Rev. B* **83**, p. 094410, Mar 2011.
- [6] S. I. Kiselev, J. C. Sankey, I. N. Krivorotov, N. C. Emley, R. J. Schoelkopf, R. A. Buhrman, and D. C. Ralph, "Microwave oscillations of a nanomagnet driven by a spin-polarized current.," *Nature* **425**, pp. 380–3, Sept. 2003.
- [7] D. Houssameddine, U. Ebels, B. Delaët, B. Rodmacq, I. Firastrau, F. Ponthenier, M. Brunet, C. Thirion, J.-P. Michel, L. Prejbeanu-Buda, M.-C. Cyrille, O. Redon, and B. Dieny, "Spin-torque oscillator using a perpendicular polarizer and a planar free layer.," *Nature materials* **6**, pp. 441–7, June 2007.
- [8] A. Brataas, Y. Tserkovnyak, G. Bauer, and B. Halperin, "Spin battery operated by ferromagnetic resonance," *Physical Review B* **66**, pp. 1–4, Aug. 2002.
- [9] Y. Tserkovnyak, A. Brataas, and G. E. W. Bauer, "Spin pumping and magnetization dynamics in metallic multilayers," *Phys. Rev. B* **66**, p. 224403, Dec 2002.
- [10] Y. Tserkovnyak, A. Brataas, and G. E. W. Bauer, "Enhanced gilbert damping in thin ferromagnetic films," *Phys. Rev. Lett.* **88**, p. 117601, Feb 2002.
- [11] A. Brataas, Y. Tserkovnyak, and G. E. W. Bauer, "Scattering theory of gilbert damping," *Phys. Rev. Lett.* **101**, p. 037207, Jul 2008.
- [12] R. Meckenstock, "Invited review article: Microwave spectroscopy based on scanning thermal microscopy: Resolution in the nanometer range," *Rev. Sci. Instrum.* **79**(4), p. 041101, 2008.
- [13] F. Sakran, A. Copty, M. Golosovsky, D. Davidov, and P. Monod, "Scanning ferromagnetic resonance microscopy and resonant heating of magnetite nanoparticles: Demonstration of thermally detected magnetic resonance," *Applied Physics Letters* **84**(22), pp. 4499–4501, 2004.
- [14] J. Coey, *Magnetism and magnetic materials*, Cambridge University Press, 2010.
- [15] M. V. Costache, S. M. Watts, M. Sladkov, C. H. van der Wal, and B. J. van Wees, "Large cone angle magnetization precession of an individual nanopatterned ferromagnet with dc electrical detection," *Applied Physics Letters* **89**(23), p. 232115, 2006.

- 
- [16] F. L. Bakker, A. Slachter, J.-P. Adam, and B. J. van Wees, "Interplay of Peltier and Seebeck Effects in Nanoscale Nonlocal Spin Valves," *Physical Review Letters* **105**, pp. 1–4, Sept. 2010.
- [17] A. Slachter, F. L. Bakker, and B. J. van Wees, "Thermal spin transport and spin-orbit interaction in ferromagnetic/non-magnetic metals," *ArXiv e-prints*, July 2011.
- [18] C. Kittel, *Introduction to Solid State Physics -7th ed.*, John Wiley & Sons, Inc., New York, 1995.
- [19] X. Wang, G. E. W. Bauer, B. J. van Wees, A. Brataas, and Y. Tserkovnyak, "Voltage generation by ferromagnetic resonance at a nonmagnet to ferromagnet contact," *Phys. Rev. Lett.* **97**, p. 216602, Nov 2006.
- [20] M. V. Costache, M. Sladkov, S. Watts, C. H. van der Wal, and B. J. van Wees, "Electrical Detection of Spin Pumping due to the Precessing Magnetization of a Single Ferromagnet," *Physical Review Letters* **97**, pp. 1–4, Nov. 2006.



## Appendix A

---

# Fabrication & measurement techniques

This appendix is organized in the following way. First, the different steps for optical- and electron-beam lithography are summarized. Then, a recipe for sputtering of nanosized strips is introduced. The last part focuses on the measurement setup and techniques.

### A.1 Fabrication techniques

The nanoscale devices discussed in this thesis are all fabricated with standard lithographic techniques using the facilities of the Groningen department of NanoLab NL and the Zernike Institute for Advanced Materials. For the samples, a combination of optical- and electron-beam lithography is performed in order to reduce the total fabrication time. The optical lithography is performed on a full 2-inch Si/SiO<sub>2</sub> wafer (300 nm of thermally oxidized Si) to create the standard large (millimeter to micrometer) contact patterns that do not vary from sample to sample. This optical technique allows for batch processing such that many (> 100) samples can be made at once. On the other hand, the disadvantage of using lithographic photo masks is that the patterning can not be adjusted easily. Figure A.1a shows the standard contact pattern that is made using the optical lithography on a single sample (2 mm × 2 mm) glued on a chip carrier. Using wire bonding techniques, the Au pattern is connected to the chip carrier with thin wires of AlSi (99% Al, 1% Si). The contacts come together at the center of the sample in an area of 100 by 100 μm (depicted in Figure A.1b). Here, the actual device is created using electron-beam lithography techniques combined with e-beam evaporation and sputtering.

#### A.1.1 Deep-UV Lithography

The optical pattern is created using the EVG-620 Deep-UV Mask Aligner system in combination with a specifically designed mask. The lithographic steps are shortly described below:

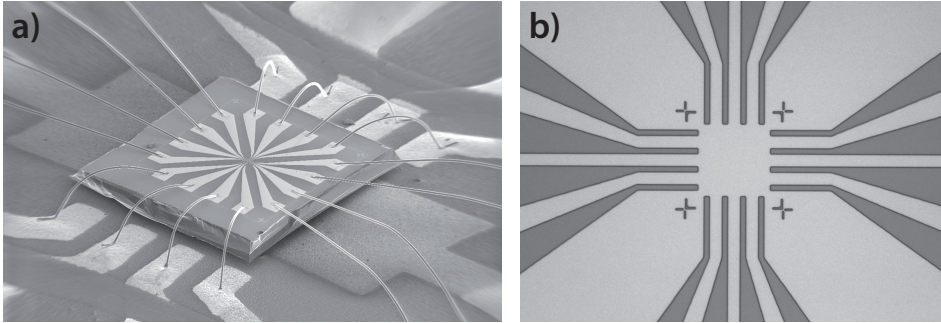


**Figure A.1:** (a) Scanning electron microscopy image of a single sample glued on top of a chip carrier. The sample contacts are bonded to the chip carrier with small wires. On top of the Si/SiO<sub>2</sub> substrate, a standard, 100 nm thick, contact pattern of Au is deposited. This pattern is created using deep-UV optical lithographic methods. (b) In the center of a sample where the contacts come together, the actual device is fabricated using e-beam lithography. The cross-shaped markers enable a accurate alignment of the e-beam column such that successive lithographic steps can be positioned as desired.

### Resist spinning

- Most electron-beam photo resists are also sensitive to deep UV light ( $\lambda < 300$  nm) and hence, the polymer PMMA is in principle suitable for deep-UV lithography. However, for multiple reasons, we have chosen to use ZEP-520 dissolved in Anisole. The photo resist is spun at 4000 RPM for 60 seconds on a full 2-inch wafer, which results in a layer thickness of  $\approx 300$  nm. Subsequently, the wafer is baked for 90 seconds on the hotplate at 180°C.

### Deep-UV Exposure

- For the exposure, a constant dose of  $700 \text{ mJ cm}^{-2}$  is used. Note that the dose can depend on the age of the resist. New resists are usually more sensitive than older ones. The system is operated in hard contact mode.

### Development

- The exposed areas are developed in n-Amyl acetate for 60 seconds, immediately followed by rinsing in IPA for 30 seconds.



## Deposition

- For all samples we have evaporated a layer of 5 nm Cr or Ti followed by a 100 nm thick layer of Au, usually at a deposition rate between 0.1 and 0.5 nm s<sup>-1</sup>. These layers can be deposited in any directional evaporator (no sputtering, since that leads to deposition on the side walls of the resist pattern). For the devices in this thesis we have used a TFC-2000 e-beam evaporator from Temescal.

## Lift-off

- To remove the photo resist, the wafer is put in hot PRS3000 (90°C) for 10 minutes. For easy lift-off, a pipette can be used or, if necessary, it can be put in the ultrasonic bath at low power.
- To remove all resist residue, the wafer is plasma etched for 1 minutes (100W) with O<sub>2</sub> (flow: 25 sccm) in the load lock of the KJL sputter system.

### A.1.2 Electron beam lithography (EBL)

In the center of the samples, there is space to pattern the actual device (shown in Figure A.1b). In this 100 × 100 μm working area, the actual device is patterned using a Raith e-line EBL system. With this system it is possible to design and fabricate patterns down to approximately 20 nm and its outstanding stage stability enables multi-layer fabrication with a position accuracy of < 10 nm. For the processing of the spin-dependent Peltier devices, we have performed up to 7 successive EBL lithography cycles which all needed to be positioned accurately with respect to each other. Below the different steps for a single EBL cycle are discussed.

#### Resist spinning

- For all steps we have made use of the EBL photo resist PMMA 950K (2 - 4 % dissolved in ethyllactate). The thickness of these layers vary between 70 and 400 nm, depending on the percentage and spinning procedure. The photo resist is spun at 4000 RPM for 60 seconds on a small piece of wafer (usually 4 × 4 devices). Subsequently, the wafer is baked for 90 seconds on the hotplate at 180°C.

## Exposure

- The exposure is performed in the Raith e-line electron-beam lithography system at a pressure  $< 1 \times 10^{-5}$  mbar. Using an automatic script for the scanning of the cross-shaped markers (shown in Figure A.1b the e-beam column is aligned to the sample (automatic write-field alignment). The patterns are written with an e-beam accelerated up to 30 kV and an aperture size of 10  $\mu\text{m}$ , using a dose of 450  $\mu\text{C}/\text{cm}^2$ .

## Development

- The exposed areas are developed in a mixture of MIBK:IPA (1:3) for 30 seconds, immediately followed by rinsing in IPA for 30 seconds.

## Deposition

- The different materials are deposited in the Temescal TFC-2000 e-beam evaporator system with a base pressure of  $10^{-7}$  mbar. If clean Ohmic contact is required between materials from successive EBL cycles, the sample is cleaned using 15 seconds of Ar ion milling prior to deposition. The ion beam is set at an accelerator voltage of 500 V and a current of 14 mA in combination with a neutralizer. The etching process damages the photo resist layer and can therefore not be performed with extremely thin resist layers ( $< 100$  nm).

## Lift-off

- To remove the photo resist, the wafer is put in hot Acetone (40°C) for 10 minutes. For easy lift-off, a pipette can be used. Ultrasonic treatment is here avoided since this could lead to accidental lift-off of the small device structures.

### A.1.3 Sputtering of lithographically defined strips

In many situations, the use of pure metals is not sufficient and the deposition of alloys is required. If the melting point (in fact, for evaporation the vapour pressure is of importance) of all materials that form the alloy is equal, the deposited material has a similar composition as the target material. However, if this is not the case, the composition of the deposited alloy is completely different and uncontrolled. For these alloys, sputtering is preferred above e-beam evaporation. However, for the fabrication of nanosized structures the sputtering technique has some disadvantages. Due to the relatively high pressure during sputtering ( $> 10^{-3}$  mbar), the

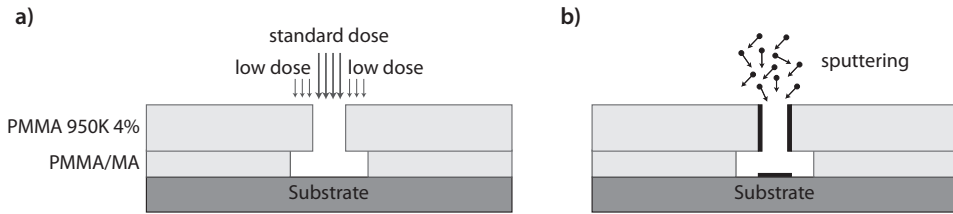


**Figure A.2:** Double-layer resist technique for the sputtering of nanoscale strips. The first layer of PMMA/MA has a thickness of 150 nm, whereas the second layer of PMMA 950 K is 300 nm thick. (a) By using the difference in sensitivity between the two resists, one can create an undercut structure as indicated. (b) Since sputter deposition techniques are not very directional, the double-layer resist pattern avoids the deposition of material on the side-walls of the under layer. Hence, after lift-off no 'ears' will be attached to the deposited strips.

deposition is not very directional and hence, material deposits on the side-walls of the photo resist (indicated in Fig. A.2). In order to avoid that this process leads to rough edges of the deposited film, a double-layer resist with an overhanging profile is created. The complete recipe is described below.

### Resist spinning

- The first photo resist layer that is spun is a copolymer resist named PMMA-MA, dissolved in Ethyllactate, with a thickness of 150 nm. The sample is baked for 90 seconds on the hotplate at 180°C. Then, a second (thicker) layer of PMMA 950K (4% in Ethyllactate) is spun and baked for 90 seconds on the hotplate at 180°C.

### Exposure

- The exposure is performed in the electron-beam lithography system. The patterns are written with an e-beam accelerated up to 30 kV and an aperture size of 10  $\mu\text{m}$ . The overhanging profile is created by using a different dose for the open ( $450 \mu\text{C}/\text{cm}^2$ ) and overhanging areas ( $112.5 \mu\text{C}/\text{cm}^2$ ) as indicated in Fig. A.2. For an optimal result, the width of the overhanging areas has to be larger than 100 nm.

### Development

- The exposed areas are developed in a mixture of MIBK:IPA (1:3) for 30 seconds, immediately followed by rinsing in IPA for 30 seconds.

## **Deposition**

- The alloy material is deposited using the KJL sputter system at a pressure of  $5 \times 10^{-3}$  mbar with a deposition rate of approximately 1 nm/s.

## **Lift-off**

- To remove the photo resist, the wafer is put in hot Acetone (40°C) for 10 minutes. For easy lift-off, a pipette can be used.

## **A.2 Measurement setup and techniques**

All devices discussed in this thesis are measured at room temperature and in air. Figure A.3a shows an example of a sample glued onto a chip carrier which is placed between the two poles of a GMW Dipole Electromagnet (type 5403). Via wire bonding and the lithographic contacts shown in Fig. A.3b the measurement setup is connected to the actual device (fabricated in the center area of Fig. A.3b). Two types of measurements are mainly performed. The stationary (spin-) caloritronic effects are studied with current driven voltage measurements using a lock-in technique. For this technique, low-frequencies ( $< 100$  Hz) are used to assure that the system is always in an equilibrium state. The details of this technique will be described in the next section. In Chapter 7, the magnetization dynamics are investigated using a modulated microwave frequency magnetic field. This frequency modulation method is the subject of Section A.2.2.

### **A.2.1 Harmonic response voltages**

The stationary (spin-) caloritronic effects are investigated using a set of three Stanford SR-830 Lock-in amplifiers combined with a homebuilt IV measurement box which is used as a floating current source and signal amplifier. The setup is computer controlled by specifically designed applications using National Instruments' LabVIEW software. One of the lock-in systems modulates the input current  $I(t)$  with a typical frequency of approximately 17 Hz. The output voltage  $V(t)$  of the device is amplified up to a factor  $10^3$  using the IV measurement box and is then returned to the lock-in systems. The three lock-in systems measure the first, second and third harmonic response voltages, respectively, and enable the separate measurement of linear, quadratic and higher order effects. For the measurements discussed in this thesis, distinguishing between voltages that depend linear and for instance quadratic on the applied current is of great importance. The total response

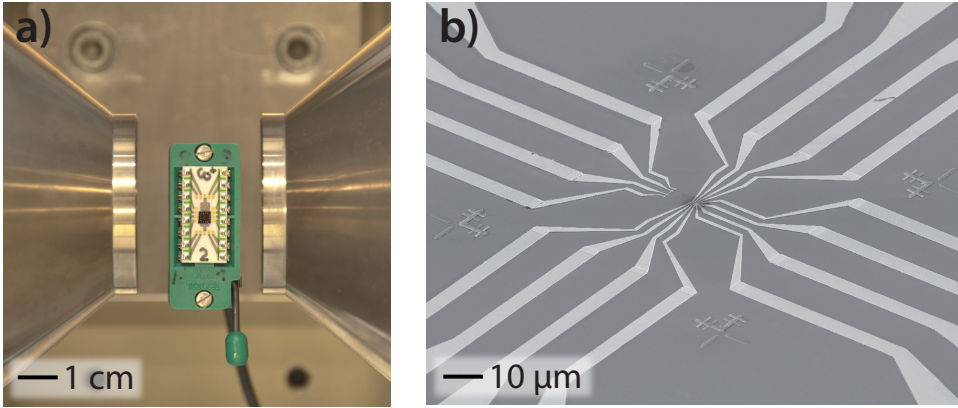


**Figure A.3:** (a) The sample is glued on a chip carrier (white) and placed between the two poles of an electromagnet. Via wire bonding the Au contacts on the sample are attached to the chip carrier which is via a cable connected to the measurement setup. All measurements are performed in air and at room temperature. (b) Zoom-in of the sample area. On the Si/SiO<sub>2</sub> substrate, large Au contacts connect the actual device (fabricated in the center of (b)) with the contact pads at the outer sides.

voltage can be written as follows:

$$V(t) = R_1 I(t) + R_2 I^2(t) + R_3 I^3(t) + \dots \quad (\text{A.1})$$

with  $R_i$  the  $n$ -th harmonic response. For an alternating current with an angular frequency  $\omega$ , these harmonic responses can be obtained separately by detecting the voltage response at different frequencies ( $1\omega$ ,  $2\omega$ , etc).

Lock-in amplifiers are mainly used to extract a signal with a known carrier wave from a noisy background environment. The mechanism is based on the orthogonality of sinusoidal functions. When two sine wave functions with different frequencies are multiplied and integrated over a time much longer than one period, the result is zero. However, only if the two frequencies are equal and if both signals are in phase with each other, a nonzero output is expected being equal to half of the product of the amplitudes. One of the largest advantages of the lock-in technique above dc voltage measurements is reduction of the noise in the signal. Since a lock-in measurement is only sensitive to a very narrow frequency spectrum, the white noise is greatly reduced compared to a dc measurement. Additionally, if the signal of interest is nearly constant,  $1/f$  noise is often overwhelming the signal. Modulation of the signal using the reference signal of a lock-in can help in significantly reducing this type of noise.

Suppose that the magnitude of the applied current is set to a rms value of  $I_0$ , then the time-dependent current is written as  $I(t) = \sqrt{2}I_0 \sin \omega t$ . The dc output voltage of the lock-in system is given by the multiplication of the measured voltage with a reference signal (with a frequency and phase which equals that of the applied current) integrated over time as:

$$V_n = \frac{\sqrt{2}}{T} \int_{t-T}^t \sin(n\omega s + \phi) V(s) ds \quad (\text{A.2})$$

with  $\phi$  the phase that can be set on the lock-in system. Setting the phase to  $\phi = 90^\circ$ , the out-of-phase components can be measured which are usually generated if capacitances or inductances are present in the circuitry. With the assumption that only first, second and third order responses are present, we can use equations A.1 and A.2 to find an expression for the output voltages of the lock-in amplifier for the different harmonic responses:

$$\begin{aligned} V_1 &= I_0 R_1 + \frac{3}{2} R_3 I_0^3 & \text{for } \phi = 0^\circ \\ V_2 &= \frac{1}{\sqrt{2}} I_0^2 R_2 & \text{for } \phi = -90^\circ \\ V_3 &= -\frac{1}{2} I_0^3 R_3 & \text{for } \phi = 0^\circ \end{aligned} \quad (\text{A.3})$$

In the case of a measurement, the values for  $R_n$  can now be calculated using the corresponding lock-in dc voltage  $V_n$  and the applied current  $I_0$ . Note that in the first harmonic response of the lock-in there is a contribution of the third order response resistance. In many cases, this contribution is much smaller than the linear response and can therefore be neglected. However, in rare cases (for example for strong temperature dependencies) a large third harmonic response might be present. By measuring the first harmonic response as a function of the applied current, one can verify its linearity and exclude these effects. The even harmonics should be measured with a phase shift of  $-90^\circ$ .

### A.2.2 High frequency measurements

The magnetization dynamics discussed in Chapters 6 and 7 is studied using the signal generator of a Rhode & Schwarz ZVA40 Vector Network Analyzer. This system can provide microwave frequencies up to 50 GHz with a maximum power of 20 dBm. The signals are transmitted to the sample via special microwave cabling and a set of GGB Picoprobes in order to achieve the best impedance matching. On the sample, a specifically designed coplanar waveguide brings the microwave signal

to the center of the device where it is short-circuited in order to generate an alternating magnetic field. This field drives the magnetization dynamics. The dimensions of the waveguide are calculated using the free software Transmission Line Calculator (TXline).

In order to separate the ferromagnetic resonance features from  $1/f$  noise and spurious heating effects, a modulation technique is implemented. Using a lock-in amplifier as a reference source, the generated microwave signal is modulated between two frequencies (e.g. 5 and 10 GHz) at a low frequency (typically 20 Hz). The lock-in amplifier is tuned to the same modulation frequency (20 Hz) and detects effectively the difference in the measured voltage between a driving frequency of 5 and 10 GHz,  $V = V_{f=5\text{GHz}} - V_{f=10\text{GHz}}$ . If the modulation is performed at large enough frequency, the  $1/f$  noise is reduced significantly. Furthermore, voltages that are present at both microwave frequencies cancel out which reduces the (thermal) baseline voltage.





---

## Summary

The transport of negatively charged electrons in solid-state nanostructures (often called devices) is an essential mechanism for the functioning of modern computers and for a whole range of other electrical equipment. Whenever a voltage is applied between two spatially separated points on a metallic conductor, the freely available electrons start to diffuse from the negatively biased side towards the positive side, which leads to a flow of charge (an electrical current). Due to the high number of free electrons that are available for conduction in metallic systems, such a cloud of electrons moves at an extremely slow pace, typically a fraction of a millimeter per second for everyday currents. Nevertheless, the average velocity of a single electron is large, in the order of a fraction of the speed of light ( $c = 300.000.000$  m/s). This contrast is caused by the many collisions between electrons which makes the system diffusive and behave like a gas, an electron gas. If instead of a voltage a temperature difference is applied between the two sides, the electron gas contributes to the transport of energy (heat) through the conductor. Hot electrons can transfer their energy to neighboring (colder) electrons during collisions and thereby create a flow of heat through the material, without electrons being physically moved from one side to the other. Since both charge transport and heat transport are a property of the electron gas it is not surprising that there exists an interaction between them. This interaction is called thermoelectricity and describes the generation of a voltage due to a temperature gradient (Seebeck effect) and the inverse effect, heating or cooling by charge currents (Peltier effect).

Additionally to charge and energy, electrons possess a third property: the electron spin or simply spin. This quantum mechanical spin describes the angular momentum that is associated with the electron. Since the electron has both a charge and spin it behaves as a small magnet with an intrinsic magnetic moment. The transport of electrons implies thus automatically a flow of magnetic moments, i.e.

a spin current. If the directions of the magnetic moments are completely randomized, then the charge current is not accompanied by a net flow of spin. However, in magnetic materials the majority of the electron spins point in the same direction and together they form the magnetization of the material. Hence, a charge flow in a magnetic material effectively transports magnetism. Whenever this current enters an adjacent non-magnetic metal, it injects this magnetic moment into the metal. This mechanism is called spin injection and makes the non-magnetic metal slightly magnetic. These injected spins can only survive over very short distances (in the order of hundreds of nanometers), whereafter a relaxation mechanism destroys this non-equilibrium situation. The relation between charge and spin transport has led to the research field of spin-based electrons (abbreviated: spintronics). By using the electron spin instead of its charge for processing and storage of information, novel and innovative functionality becomes possible for future spintronic devices.

This thesis describes the fundamental interactions between the three types of transport (charge, heat, spin) in magnetic nanostructures consisting of metallic elements. The work described here is part of a wider research direction, called spin-caloritronics, that studies the coupling between heat and spin transport in many different materials ranging from metals to ferromagnetic insulators. The spin-caloritronic experiments discussed in this thesis are based on the spin-dependency of regular thermoelectric effects, such as the Seebeck and Peltier effect. In spintronic devices, the transport of charge is generally described by two transport channels. A majority spin channel (usually named spin-up) for the electron spins that are pointing in the direction of the magnetization and a minority channel (usually named spin-down) for electron spins pointing anti-parallel to the magnetization. Spins pointing in a direction non-collinear with the magnetization do not survive for long in a magnetic material and can therefore be neglected. Generally, in ferromagnetic metals the majority channel has a larger conductivity since this channel contains more electrons than the minority channel. We have experimentally demonstrated that a similar approach is valid for the thermoelectric effects. One can assign different Seebeck and Peltier coefficients to the majority and minority electrons in a magnetic metal and hence, produce spin-thermoelectric effects without charge currents being involved. Whenever a temperature gradient is applied to a ferromagnet, due to the difference in Seebeck coefficients for spin-up and spin-down electrons, a spin current is generated in the ferromagnet. Such a spin current is special in the sense that it is a pure spin current, without an associated charge current. This spin current can for example be used as a thermally driven spin source for future spintronic devices. Inversely, we have shown that a spin current which is injected into a ferromagnet leads to the generation of a heat current, driven by the spin-dependent Peltier effect. This principle offers new functionality in the form of magnetically

programmable heating and cooling using spin currents. Both these effects could add new (thermoelectric) functionality to spintronic devices.

Besides spin-dependent thermoelectric effects, regular thermoelectric effects are an interesting subject to study at the nanoscale. At shorter length scales, macroscopic (classical) models that are used to describe the physics at larger scales often break down at the nanoscale due to quantum-mechanical effects. Therefore, we experimentally investigated the regular Seebeck and Peltier effect in magnetic and nonmagnetic nanostructures and compared them to numerical simulations. It turns out that even though the device dimensions are approaching the mean free path length of the electrons, the system is still perfectly described by the classical equations for charge and heat transport. Moreover, we have found that thermoelectric effects are responsible for the spin-independent voltages that are often present in measurements of magnetic nanostructures, for example in nonlocal spin valves. The numerical simulations that are performed are 3D finite-element calculations using a diffusive transport model based on Ohm's and Fourier's law which is, for the spin-dependent thermoelectric effects, extended to a two (spin) channel model.

Thusfar, the discussed effects are stationary, i.e. they do not vary in time. However, magnetization reversal or the precessional motion of the magnetization are dynamical effects. The stable precession of the magnetization of a ferromagnet is called ferromagnetic resonance and adds a whole range of other effects to the field of spintronics. For example, the transfer of angular momentum from an adjacent metal into a ferromagnet leads to a torque on the magnetization and can ultimately, induce ferromagnetic resonance. On the other hand, a precessional magnetization motion pumps spins into an adjacent nonmagnetic metal as if it is a spin battery. In this thesis, the experimental work has focused on the coupling of magnetization dynamics with heat, being another branch of spin-caloritronics. We have studied the generation of heat during ferromagnetic resonance due to the damping and measured the temperature increase thermoelectrically. This novel technique provides an alternative method to characterize ferromagnetic resonance in a material and is applicable to conductive and non-conductive media.

The potential advantages of spin-caloritronic effects with respect to regular thermoelectricity can be found in the easy manipulation of magnetic textures at the nanoscale. This enables very localized and programmable control of heat flow which might prove useful for thermopower energy harvesting or refrigeration. However, the previously discussed effects are still weak and far from direct applications. Nonetheless, a combination of new developments in this field and by exploring novel materials it could one day lead to the implementation of spin-caloritronics in our everyday electronic devices.



---

## Samenvatting

Het transport van negatief geladen elektronen in vaste-stof nanostructuren (ook wel devices genoemd) is essentieel voor het functioneren van diverse elektrische apparaten en in het bijzonder voor moderne computers. Wanneer een spanning wordt aangelegd tussen twee punten op een metallische geleider, beginnen de vrije elektronen te bewegen in de richting van de positieve pool. Dit leidt tot een stroom van lading (een elektrische stroom). Ten gevolge van het enorme aantal elektronen dat beschikbaar is voor geleiding in metallische systemen beweegt zo'n wolk van elektronen zich slechts heel langzaam door het materiaal, met een fractie van een millimeter per seconde voor alledaagse stromen. Desalniettemin is de gemiddelde snelheid van een enkel elektron erg groot, ongeveer een fractie van de lichtsnelheid ( $c = 300.000.000$  m/s). Dit grote contrast wordt veroorzaakt door de grote hoeveelheid botsingen die elektronen onderling hebben en maakt het systeem diffuus. Zo'n systeem gedraagt zich als een gas is, een elektronengas. Als in plaats van een spanning een temperatuurverschil wordt aangelegd tussen de twee uiteinden van een geleider, dan draagt het elektronengas bij aan het transport van energie (warmte) door de geleider. Warme elektronen kunnen hun energie overdragen aan naastgelegen (koudere) elektronen tijdens botsingen en op deze manier een warmtestroom veroorzaken, zonder dat elektronen zich daadwerkelijk fysiek verplaatsen van het ene uiteinde naar het andere. Omdat zowel ladingstransport als warmte-transport eigenschappen van het elektronengas zijn, is het niet verbazingwekkend dat er een interactie bestaat tussen beide vormen van transport. Deze interactie wordt thermo-elektricititeit genoemd en beschrijft het opwekken van een spanning ten gevolge van het aanleggen van een temperatuurverschil (Seebeck effect) en het omgekeerde effect, verwarmen of koelen door middel van ladingstromen (Peltier effect).

Naast lading en energie, bezitten elektronen nog een derde eigenschap: de elektronenspin of kortweg spin. Deze kwantummechanische spin beschrijft het impulsmoment dat wordt geassocieerd met het elektron. Omdat een elektron zowel een spin als een lading heeft, gedraagt het zich als een magneetje met een intrinsiek magnetisch moment. Het transport van elektronen impliceert dus automatisch een stroom van magnetisch moment, ook wel spinstroom genoemd. Indien de richtingen van al deze magnetische momenten volledig willekeurig georiënteerd zijn, heeft een ladingstroom geen spinstroom tot gevolg. Dit is echter niet het geval in magnetische materialen waar het merendeel van de elektronenspins in dezelfde richting wijzen en samen de magnetisatie vormen. Een ladingstroom in een magnetisch materiaal leidt daarom wél tot het transport van spin, oftewel magnetisme. Indien deze stroom vervolgens in een naastgelegen niet-magnetisch metaal terechtkomt, neemt het zijn magnetisch moment mee. Hierdoor kunnen effectief spins geïnjecteerd worden en wordt het niet-magnetisch metaal dus licht magnetisch. Zulke spins kunnen in metalen maar over zeer korte afstanden (enkele honderden nanometers) overleven, waarna een relaxatie mechanisme zorgt voor het verdwijnen van deze niet-evenwichtssituatie. Het onderzoek naar dit soort effecten is daarom alleen mogelijk in nanostructuren. De relatie tussen lading en spin heeft geleid tot het ontstaan van het onderzoeksveld van spin-gebaseerde elektronica (afgekort: spintronica). Het gebruik van de spin in plaats van de lading voor het verwerken en opslaan van informatie biedt nieuwe mogelijkheden en creëert functionaliteit voor toekomstige spintronica devices die voorheen niet bestond.

Dit proefschrift beschrijft de fundamentele interacties tussen de drie vormen van transport (lading, warmte en spin) in magnetische nanostructuren opgebouwd uit metallische elementen. Het beschreven werk is een onderdeel van een breder onderzoeksgebied dat spin-caloritronica wordt genoemd. Deze onderzoeksrichting bestudeert de koppeling tussen warmte- en spintransport in verschillende materialen, variërend van metalen tot ferromagnetische isolatoren. De spin-caloritronische experimenten die worden behandeld in dit proefschrift zijn gebaseerd op de spinafhankelijkheid van de reguliere thermo-elektrische effecten, zoals bijvoorbeeld het Seebeck en Peltier effect. Voor de beschrijving van het transport in spintronische devices worden de elektronen in het algemeen opgesplitst in twee transportkanalen. Een spin-up kanaal voor de elektronenspins die in de richting van de magnetisatie wijzen en een spin-down kanaal voor de elektronenspins die tegengesteld aan de magnetisatie gericht zijn. Spins die niet collineair georiënteerd zijn met de magnetisatie, kunnen slechts voor zeer korte tijd overleven en worden daarom meestal niet meegenomen in de beschrijving. Over het algemeen heeft het spin-up kanaal een grotere geleiding in ferromagnetische materialen, omdat dit kanaal meer elektronen bevat dan het spin-down kanaal. Wij hebben experimenteel aangetoond dat

eenzelfde benadering ook opgaat voor thermo-elektrische effecten. Het blijkt zo te zijn dat in een magnetisch materiaal de twee spin kanalen beide een ander Seebeck en Peltier coëfficiënt hebben. Hierdoor kunnen spin-thermoelektrische effecten plaatsvinden zonder dat er een ladingstroom nodig is. Wanneer een temperatuurgradiënt wordt aangelegd tussen de twee uiteinden van een ferromagneet wordt een spinstroom gegeneerd, die wordt gedreven door het verschil in de Seebeck coëfficiënten voor spin-up en spin-down. Deze spinstroom is een pure spinstroom wat betekent dat er geen ladingstroom mee geassocieerd is. De spinstroom kan bijvoorbeeld worden toegepast als een thermische bron voor spins in toekomstige spintronische devices. Omgekeerd hebben we laten zien dat een spinstroom die wordt geïnjecteerd in een magnetisch materiaal kan leiden tot een warmtestroom, gedreven door de spin-afhankelijke Peltier coëfficiënt. Dit principe biedt nieuwe functionaliteit in de vorm van magnetisch programmeerbare verwarming en koeling met behulp van spinstromen.

Naast spin-afhankelijke thermo-elektrische effecten zijn de reguliere Seebeck en Peltier effecten op de nanoschaal een interessant studie object. Op zeer korte lengteschalen werken klassieke fysische modellen vaak niet meer door de toenemende invloed van kwantummechanische effecten op de nanoschaal. We hebben daarom experimenteel het Seebeck en Peltier effect onderzocht in magnetische en niet-magnetische nanostructuren en dit vergeleken met numerieke computersimulaties. Het blijkt dat, ondanks het feit dat de grootte van onze devices nagenoeg de vrije padlengte van de elektronen benadert, het systeem nog steeds goed beschreven wordt door de klassieke vergelijkingen voor lading- warmtetransport. Daarnaast hebben we aangetoond dat thermo-elektrische effecten verantwoordelijk zijn voor de spin-onafhankelijke spanningen die vaak aanwezig zijn in metingen van magnetische nanostructuren, bijvoorbeeld in niet-lokale spinkleppen. De numerieke simulaties die zijn uitgevoerd bestaan uit 3D eindige-elementen berekeningen waarbij gebruik is gemaakt van een diffuus transportmodel gebaseerd op de wetten van Ohm en Fourier. Voor de spin-afhankelijke thermo-elektrische effecten is dit model uitgebreid naar een twee (spin) kanalen model.

De tot dusver besproken effecten zijn allemaal stationair, ze variëren niet in de tijd. Het ompolen van de magnetisatie of de precessionele beweging van de magnetisatie zijn echter dynamische effecten. De stabiele precessie van de magnetisatie van een ferromagneet wordt ook wel ferromagnetische resonantie genoemd en dergelijke effecten maken nieuwe spintronische concepten mogelijk. Het overbrengen van het impulsmoment van een niet-magnetisch metaal naar een naastgelegen ferromagneet (spin-injectie genoemd) leidt tot een impulsmoment op de magnetisatie van de ferromagneet en kan uiteindelijk ferromagnetische resonantie veroorzaken. Andersom kan een precederende magnetisatie spins in een naastgelegen niet-

magnetisch metaal pompen, vergelijkbaar met een spin-batterij. In dit proefschrift is het experimentele werk gefocust op de koppeling tussen magnetisatiedynamica en warmte, een ander deelgebied van spin-caloritronica. De warmtegeneratie ten gevolge van de demping gedurende ferromagnetische resonantie is bestudeerd en gemeten met thermo-elektrische technieken. Deze nieuwe techniek voorziet in een alternatieve methode voor het karakteriseren van ferromagnetische resonantie in een materiaal en is zowel toepasbaar in geleidende als niet-geleidende media.

De meerwaarde van deze spin-caloritronische effecten ligt, ten opzichte van reguliere thermo-elektriciteit, in het gemak van het controleren van de magnetische textuur op de nanoschaal. Dit biedt daarom een sterk gelokaliseerde en programmeerbare controle over warmtestromen en zou bruikbaar kunnen zijn voor het genereren van thermo-elektrische energie of voor koeling. De gemeten effecten zijn echter nog steeds erg klein en zijn nog ver weg van directe toepassingen. Desalniettemin zouden nieuwe ontwikkelingen binnen dit onderzoeksveld gecombineerd met het verkennen van nieuwe materialen op een dag kunnen leiden tot de implementatie van spin-caloritronica in onze dagelijkse elektronische apparatuur.



---

## Acknowledgements

Approximately four and a half year ago, I started as a PhD student working in the field of spintronics in the Physics of Nanodevices group of the University of Groningen. During my bachelor in Applied Physics, I did never consider the option of becoming a PhD student after finishing my study. However, by the time I performed my Master research, the actual scientific and experimental work attracted me so much that I changed my mind. I decided to go for it and I've never regretted that decision. Although the research went in a slightly different direction than initially planned, I can now look back at a pretty successful PhD time. But I would never have come this far without the help of all the people in my surroundings.

Let me start with expressing my thanks to Bart, my professor. I believe you are an outstanding physicist with an impressive research group, well equipped and very friendly. Thank you for giving me the freedom and confidence to perform the research along my own route and for guiding me when necessary. I think these are among the most important ingredients for a successful PhD. Moreover, I admire your analytical skills and your ability to dismantle a problem, no matter how complex, into understandable concepts. Your role as the "devils advocate" during the group meetings was, although sometimes a bit disturbing, very helpful in finding flaws in the interpretation of the data.

Dear professors Arne Brataas, Christian Back and Thom Palstra, thank you for being part of the reading committee and for the constructive suggestions to improve this thesis. Arne, thanks for inviting me to this wonderful scientific/ski meeting in Oppdal (Norway) in the beginning of this year. Moreover, I would like to express my gratitude to all the members of the spin-caloritronics community for all the nice meetings we had in the past at so many different locations.

Caspar, thank you for being my supervisor for my teaching duties with high school students and for the advice on the breakjunction exhibit. Tamalika, thanks for all the chocolate sweets during the coffeebreaks, even though we sometimes disagreed about proper Temescal use.

Of course, I would like to spend a few words on Bram. Bram, when I started my PhD you just switched from being an optics guy to metallic spintronics. Since that was exactly the topic I was supposed to work on, a collaboration was born. Although we struggled in the beginning to get results on (supposed to be) simple experiments (e.g. to reproduce earlier work performed by Maksym), I think our collaboration was quite successful if I look back over the past years. In any case, I was more than happy that I could work together with you. Your persistence in trying to understand and model our experimental data really kept us going. Besides that, I have also good memories on our trips abroad to many different conferences. I believe our first trip together to Manchester (already in the first month of my PhD) really set the trend for all the other travels. I would like to call it a once in a lifetime experience.

Joost, we have already a long history which started in the second year of my study when we became housemates. In the second year of my PhD, you entered our research group as a Master student and we worked closely together. After you left for a half year to the USA, you came back and we became colleagues. We worked on detecting the spin-dependent Peltier effect and together we have obtained very nice results. Although you can be a bit stubborn sometimes, I think you are an excellent experimentalist and I believe you are still record holder within our group in successfully aligning the most EBL steps on top of each other. Thanks for all the fun we had, both at work and during all the borrels and outings. I am more than happy that you are willing to be my paranymph.

Thanks to the other metallic spintronics members Fasil, Vincent, Nynke and Jean-Paul. Fasil, good luck with finishing your PhD and I know you will be a perfect father soon. Vincent and Jean-Paul, it was in many ways nice to have some French input to our team.

Thanks to all the students that worked with me. Nynke, success with your PhD and good luck with maintaining the breakjunction exhibit and the levitating train. Although it was in the beginning hard for me to accept that you are a better swimmer than I am, please make sure you remain the fastest swimmer of the group. Dirk, your work as a Bachelor student has led to a very nice publication (Chapter 7 of this thesis). Thanks for all the good work and I hope your Master research will be as successful. Tom, I really regret that your research went not as planned because of two interchanged gas flow lines, but I hope it did not scare you off that much.

My roommates Thomas and Arramel, thanks for all the fun we had in our office, there have been moments that I thought our office was a second coffee room. Thomas, I will absolutely miss the daily crappy youtube videos that we used to watch. Let me highlight the knick knack video (especially the soundtrack) and the alien abduction from Pixar. I wish you a healthy new start in Vancouver and good

luck with finding a new job! Arramel, thanks for introducing us with the chainsaw, your special way of dealing with your frustration. All the best with continuing your scientific career in Indonesia.

Dear Alina, Sergii and Maksym, thanks for introducing me into the east european culture. An important lesson I learned, was that complaining does not necessarily mean that you want to change something. Alina, thanks for all your cheerfulness and of course the birthday cards. Sergii and Maksym, thank you for the great borrels we had and I hope you both get a successful career at ASML.

I would like to express my thanks to the breakjunction team, Marius T. and Eek. Marius, you were a perfect supervisor for me during my Master research and your enthusiasm really helped me in deciding whether or not to start with a PhD. Eek, thanks for helping me out with the breakjunction exhibit whenever that was needed.

For all the technical assistance, I would like to thank our technicians Bernard, Johan, Martijn and Siemon. Bernard, I surely miss our lunchtime swimming break, but I hope that we can cycle together some time soon. Johan, thank you for all the time you spend solving issues with the Varian and TFC-2000. I still do remember our hunt for strangely behaving electrons in the evaporator. Without you we probably would still have been struggling to grow nice metallic layers. Martijn, thanks for wire bonding all those hundreds of samples. And promise me that you will buy a new (proper) bike soon. A special place I reserved for Siemon, who passed away in 2011. When Siemon (and his special kind of jokes) was present during the coffeebreak, the atmosphere was always great. Those funny moments and his famous barbeques I will never forget. Of course, thanks to our secretary Anna for all your assistance and especially for helping me out with all the incomprehensible forms for the reimbursement of travel expenses.

Thanks to all the other group members for all the good discussions and great atmosphere during the coffee breaks, borrels and group outings. Thanks to Ivan, Niko, Paul, Marcos, Jasper, Javaid (formerly known as Goraya), Subir, Gaurav, Alok, Magda, Sander K., Sander O., Saurabh, Jakko, Olger, Rob, Hilbert, Jorrit, Eline, Csaba, Anatoly, Thorsten, Erik, Ji, Pedro, Mihai, Marius C., Steve, Morten, Seva, Vishal, Jan-Kees, Zorione, Juliane, Natasja and all others whom I have forgotten.

Dear friends Jesse and Jorg, thanks for the great skiing trip we had in Flachau last year. It felt just like the old days in high school. Jesse (a.k.a. Leppy), thanks for all those nights that we played online Command & Conquer. It surely helped to get relaxed and to forget about work.

Ruben, although you have chosen a completely different career path, you are still the best old study friend I have. I have very good memories of our student time, of the saté dinners and the special MSN language we developed. Yes, I know that I have now officially won the biggest nerd contest, but I am very happy that you are

willing to share this moment with me as my paranymp.

Finally, I would like to express my thanks to my family for all their support during the last four years. Kim, thanks for all your love and support. I know it has not always been easy for you during the last years because of your health. For me it feels extra special that you, even in tough times, were always there for me. I cannot wish for a better girlfriend and from now on, I'm sure, it only gets better.

Frank Bakker  
Groningen  
August 19, 2012

---

## List of publications

1. Nanoscale temperature detection using the Seebeck effect.  
F. L. Bakker, J. Flipse & B. J. van Wees.  
*J. Appl. Phys.* **111**, 084306 (2012).
2. Thermoelectric detection of ferromagnetic resonance in a nanoscale ferromagnet.  
F. L. Bakker, J. Flipse, A. Slachter & B. J. van Wees.  
*Phys. Rev. Lett.* **108**, 167602 (2012).
3. Direct observation of the spin-dependent Peltier effect.  
J. Flipse, F. L. Bakker, A. Slachter, F. K. Dejene & B. J. van Wees.  
*Nature Nanotechnology* **7**, 166 (2012).
4. Modeling of thermal spin transport and spin-orbit effects in ferromagnetic/nonmagnetic mesoscopic devices.  
A. Slachter, F. L. Bakker & B. J. van Wees.  
*Phys. Rev. B* **84**, 174408 (2011).
5. Anomalous Nernst and anisotropic magnetoresistive heating in a lateral spin valve.  
A. Slachter, F. L. Bakker & B. J. van Wees.  
*Phys. Rev. B* **84**, 020412 (2011).
6. Temperatuurverschil genereert spinstroom.  
F. L. Bakker, A. Slachter & B. J. van Wees.  
*Nederlands Tijdschrift van Natuurkunde* **77-04**, 128 (2011).

7. Public exhibit for demonstrating the quantum of electrical conductance.  
E. H. Huisman, F. L. Bakker, J. P. van der Pal, R. M. de Jonge & C. H. van der Wal.  
*American Journal of Physics* **79**, 856 (2011).
8. The mechanical response of lithographically defined break junctions.  
E. H. Huisman, M. L. Trouwborst, F. L. Bakker, B. J. van Wees & S. J. van der Molen.  
*J. Appl. Phys.* **109**, 104305 (2011).
9. Thermally driven spin injection from a ferromagnet into a nonmagnetic metal.  
A. Slachter, F. L. Bakker, J.-P. Adam & B. J. van Wees.  
*Nature Physics* **6**, 879 (2010).
10. Interplay of Peltier and Seebeck effects in nanoscale nonlocal spin valves.  
F. L. Bakker, A. Slachter, J.-P. Adam & B. J. van Wees.  
*Phys. Rev. Lett.* **105**, 136601 (2010).
11. Single atom adhesion in optimized gold nanojunctions.  
M. L. Trouwborst, E. H. Huisman, F. L. Bakker, S. J. van der Molen & B. J. van Wees.  
*Phys. Rev. Lett.* **100**, 175502 (2008).
12. Stabilizing single atom contacts by molecular bridge formation.  
E. H. Huisman, M. L. Trouwborst, F. L. Bakker, B. de Boer, B. J. van Wees & S. J. van der Molen.  
*Nano Lett.* **8**, 3381 (2008).

---

# Curriculum Vitae

Frank Lennart Bakker

3 March 1984      Born in Leeuwarden, The Netherlands.

## Education

- 3/2008 - 3/2012      Stichting Fundamenteel Onderzoek der Materie (FOM)  
Ph.D. research in the group of Physics of Nanodevices under the supervision of prof.dr.ir. B. J. van Wees  
Performed at the Rijksuniversiteit Groningen, The Netherlands
- 9/2006 - 3/2008      Rijksuniversiteit Groningen, The Netherlands  
Master Applied Physics  
Research project: "*Mechanical properties of single gold atom contacts*".
- 9/2002 - 6/2006      Rijksuniversiteit Groningen, The Netherlands  
Bachelor Applied Physics  
Research project: "*Anisotropic magnetoresistance in cobalt strips and transport phenomena in carbon nanotubes*".
- 9/1996 - 5/2002      O.S.G. Piter Jelles Montessori, Leeuwarden, The Netherlands  
VWO, profiel Natuur en Techniek

